2016 Alaska State-wide Weather Research Forecast (WRF) Meteorological Model Performance Evaluation

EPA-454/R-20-003
May 2020

2016 Alaska State-wide Weather Research Forecast (WRF) Meteorological Model Performance Evaluation

U.S. Environmental Protection Agency
Office of Air Quality Planning and Standards
Air Quality Assessment Division
Research Triangle Park, NC

Executive Summary

In 2018, the EPA Office of Air Quality Planning and Standards proposed to develop a set of one-year WRF datasets for regions not included in the prior CONUS WRF modeling domains produced annually by the EPA. The Alaska, Hawaii, and Puerto Rico regions were selected for this modeling effort. The modeling was intended as a preliminary testbed to expand the extent of the national annual WRF runs provided by the EPA. Given the limited resources initially assigned to the testbed effort, efforts were not made to determine optimized settings and parameterization schemes for simulation of the regions modeled. For Alaska, the effort was intended to provide a state-wide dataset at relatively low resolution, analogous to the EPA CONUS WRF datasets. Like the prior annual EPA CONUS WRF runs, the modeling was not intended to simulate flows in complex terrains that may require high resolution modeling to resolve.

The 9 km 2016 Alaska WRF dataset was generated using Version 3.9.1.1 of the Advanced Research WRF (ARW) core. The 9 km domain contains the entire state of Alaska except for a few of the extreme western Aleutian Islands. This report provides a model performance evaluation (MPE) of the dataset. Tools such as bias/error soccer-plots, parameter time series, and wind roses were used to assess the performance of surface and upper-air meteorological parameters such as temperature, wind speed, wind direction, and humidity. Also, state-wide monthly precipitation maps were produced for qualitative comparison to observation-based regional precipitation maps.

The analysis plots and other products contained in this report can be used by air permitting and other authorities for project-specific model performance evaluations to determine if the dataset is appropriate for regulatory use. Notably, this report itself does not represent an EPA endorsement or validation of the dataset. Any use of the dataset for regulatory purposes (such as those specified under 40 CFR Part 51, Appendix W) will require a project-specific performance evaluation and approval of the evaluation by the regulatory authorities. However, the plots, statistics, and other evaluation products included in this report can be adopted or referenced to as part of any project-specific MPE.

Questions or requests concerning the 2016 EPA Alaska WRF dataset and the MPE can be sent to Jay McAlpine of the EPA Region 10, mcalpine.jay@epa.gov or Kirk Baker of the EPA OAQPS at baker.kirk@epa.gov.

List of Tables

List of Figures

List of Acronyms

AMET	Atmospheric Model Evaluation Tool
ARW	Advanced Research WRF
ASOS	Automated Surface Observing System
CFR	Code of Federal Regulations
COOP	Cooperative Observer Program (NWS)
EPA	Environmental Protection Agency
ESRL	Earth System Research Laboratory
GFS	Global Forecast System
MADIS	Meteorological Assimilation Data Ingest System
MM5	Fifth-generation Penn State/NCAR Mesoscale Model
MPE	Model Performance Evaluation
NCAR	National Center for Atmospheric Research
NCEP	National Centers for Environmental Prediction
NLCD	National Land Cover Database
NOAA	National Oceanic and Atmospheric Administration
NWS	National Weather Service
PBL	Planetary Boundary Layer
RAWS	Remote Automatic Weather Stations
RMSE	Root Mean Square Error
SNOTEL	Snow Telemetry Station
SST	Sea Surface Temperature
WRAP	Western Regional Air Partnership
WRF	Weather Research and Forecasting (Model)

Table of Contents

1. Introduction

The United States Environmental Protection Agency (EPA) developed a one-year (2016) meteorological dataset for the state of Alaska, using the Weather Research and Forecasting model (WRF). This report provides a summary of the modeling methodology used to develop the dataset and provides a model performance evaluation (MPE) of the dataset. Like EPA's annual 12-km United States CONUS WRF models, the purpose of this dataset is to provide a resource to support air pollution and atmospheric photochemical modeling applications for regulatory and planning purposes.

The WRF model represents the state-of-the-art tool for modern mesoscale numerical meteorological simulation, designed for research and operational forecasting purposes (NCAR, 2019). WRF has largely displaced its predecessor, the MM5 model, which was widely used to provide meteorological datasets for regulatory air quality analyses in the past. WRF is now used widely by universities and government agencies, including the National Weather Service (NWS), to provide simulations and downscaling of past weather fields and forecasts of future conditions. The 2016 Alaska WRF dataset contains gridded hourly meteorological fields across two domains, at 27-km and 9-km horizontal resolutions. The modeling was conducted using meteorological inputs from a global reanalysis dataset, applying parameterization and physics schemes selected based on a survey of other recent WRF modeling efforts focused on Alaska and other arctic domains.

The MPE contained in this report evaluates the performance of the 9-km domain modeling results compared to surface and upper-air measurements of wind, humidity, and temperature. Regional precipitation estimates are also evaluated qualitatively by comparison to measurement-based regional precipitation maps.

2. WRF modeling configuration

WRF Version 3.9.1.1 of the Advanced Research WRF (ARW) core (Skamarock, 2008) was used for this work. The WRF-ARW is developed and maintained by the National Center for Atmospheric Research's (NCAR) Mesoscale and Microscale Meteorology Lab (NCAR, 2019). The modeling was conducted on the EPA High Performance Computing Center's scientific cluster located at Research Triangle Park in North Carolina. The 2016 Alaska dataset is maintained and archived by the EPA and may be obtained upon request (contact information provided in Executive Summary).

2.1 Domain configuration

Modeling was conducted using a set of nested grids. The inner grid, at a horizontal resolution of 9 km, is nested within an outer domain at 27 km horizontal grid spacing. The grids are shown in **Figure 1**. The modeling domains were defined with a goal of capturing all parts of the state of

Alaska within the inner 9-km domain. The sizing and location of the domains also were configured to fit well within the global GEOS-CHEM grid domain, to account for derivative photochemical modeling purposes. The grids were defined using a Lambert Conformal Conic (LCC) projection centered at 155° W, 63° N and true latitudes at 60° and 70°. **Table 1** provides a summary of the configuration of the two domains.

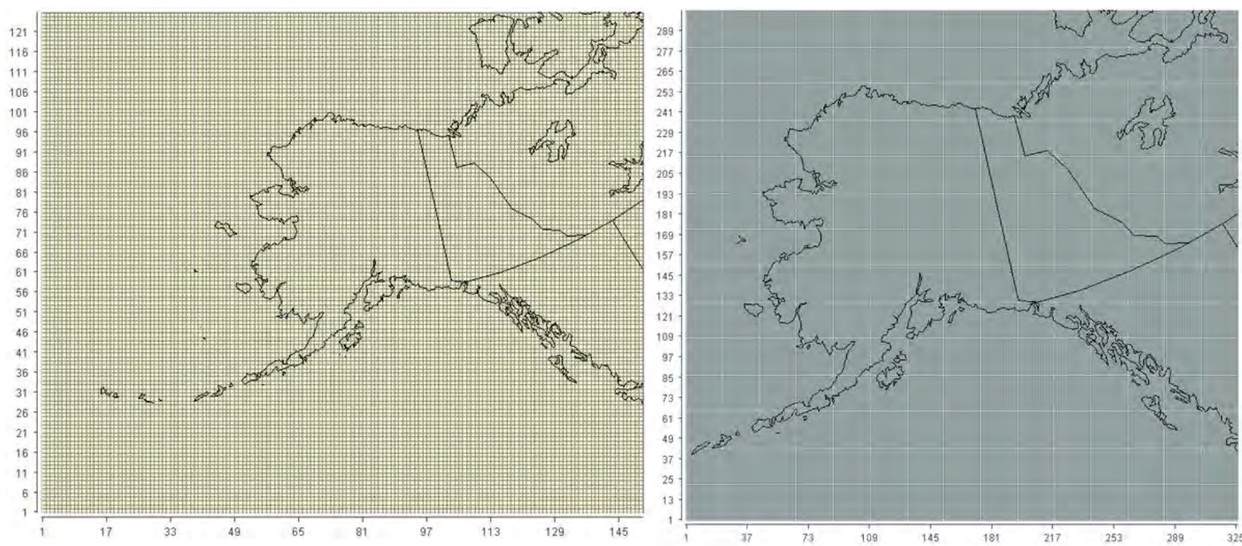

Figure 1. Alaska 27-km (left) and 9-km (right) horizontal resolution WRF modeling domains.

Table 1. WRF domain configurations.

Grid	Resolution	Nx	Ny
Outer	27 km	156	139
Inner	9 km	325	265

The domain was configured using 36 vertical layers with a first (surface) layer approximately 20 meters deep. Vertical resolution was greatest near the surface to resolve boundary layer processes. The vertical domain configuration is outlined in **Table 2** by sigma level and approximate height and pressure coordinates.

Table 2. WRF vertical domain configuration.

Layer	Sigma Level	Approximate Pressure (mb)	Approximate Height (mb)	Approximate Layer Thickness (m)
36	0.0000	50.00	19313	3423
35	0.0500	98.15	15890	2243
34	0.1000	146.30	13648	1706

Layer	Sigma Level	Approximate Pressure (mb)	Approximate Height (mb)	Approximate Layer Thickness (m)
33	0.1500	194.45	11942	1392
32	0.2000	242.60	10551	1183
31	0.2500	290.75	9367	1034
30	0.3000	338.90	8333	921
29	0.3500	387.05	7412	832
28	0.4000	435.20	6580	761
27	0.4500	483.35	5820	702
26	0.5000	531.50	5117	652
25	0.5500	579.65	4465	610
24	0.6000	627.80	3856	573
23	0.6500	675.95	3283	541
22	0.7000	724.10	2742	412
21	0.7400	762.62	2330	298
20	0.7700	791.51	2032	289
19	0.8000	820.40	1742	188
18	0.8200	839.66	1554	185
17	0.8400	858.92	1369	182
16	0.8600	878.18	1188	178
15	0.8800	897.44	1010	175
14	0.9000	916.70	834	87
13	0.9100	926.33	748	86
12	0.9200	935.96	662	85
11	0.9300	945.59	577	84
10	0.9400	955.22	492	84
9	0.9500	964.85	409	83
8	0.9600	974.48	325	83
7	0.9700	984.11	243	82
6	0.9800	993.74	162	41
5	0.9850	998.56	121	40
4	0.9900	1003.37	80	40
3	0.9950	1008.19	40	20
2	0.9975	1010.59	20	20
1	1.0000	1013.00	0.0	--

2.2 Inputs

WRF modeling requires inputs from databases to define the static and dynamic features of the land and water interfaces. Also, WRF requires inputs from a global-scale meteorological model or reanalysis dataset to provide the initial and boundary conditions of the atmosphere.
Land use and vegetation information were obtained from the recent National Land Cover Database (NLCD) provided with WRF. Topographic information for WRF was developed using the standard 30 arc-second (~900 m) resolution WRF terrain database.

The WRF model was initialized using the 0.25-degree National Centers for Environmental Prediction (NCEP) Global Forecast System (GFS) analysis and 3-hour forecast from the 00Z, 06Z, 12Z, and 18Z simulations. This dataset was also used to provide boundary conditions and analysis nudging throughout the model runs. Analysis nudging was applied aloft only; Planetary Boundary Layer (PBL) nudging of winds, temperature, and humidity was turned off. No observational nudging was used in the modeling. Sea surface temperatures (SST) and snow cover were obtained from the GFS analysis also.

2.3 WRF options and parameterization schemes

WRF contains a suite of state-of-the-art atmospheric physics parameterization schemes. The options and models used in the Alaska WRF modeling are listed in **Table 3**. A local-closure PBL scheme was selected to more accurately simulate the PBL in highly stable conditions, based on the understanding non-local schemes may result in excessive mixing in highly stable conditions near the surface.

Table 3. Physics parameterization schemes used in the 2016 Alaska WRF model.

Physics Scheme	WRF scheme variable name	Model Selected	Description
Land Surface Model	sf_surface_physics	NOAH	Surface flux parameterization scheme based on a four-layer soil temperature and moisture model. Accounts for fractional snow cover and frozen soil physics.
PBL parameterization	bl_pbl_physics	MYNN PBL model	Local 2.5-order closure K-theory based model. Model set to compute each time step.
Atmospheric surface layer parameterization	sf_sfclay_physics	MYNN surface layer model	Local 2.5-order closure surface layer model.
Cumulus/convective physics	cu_physics	Kain-Fritsch	Deep and shallow convection sub-grid scheme that applies a mass-flux approach for downdrafts. Moisture-advection modulation function used for this modeling.
Cloud/precipitation microphysics	mp_physics	Morrison double-moment scheme	Double-moment ice, snow, rain, and graupel model.
Longwave/shortwave radiation	ra_lw_physics, ra_sw_physics	RRTMG scheme	Rapid Radiative Transfer Model, including the MCICA method for random cloud overlap. Radiation physics calculation frequency set to 20 minutes.

3. Model performance evaluation methodology

The purpose of this evaluation is to determine whether the simulated meteorological outputs sufficiently represent a reasonable approximation of actual meteorological conditions that occurred over Alaska in 2016. The evaluation is conducted using both quantitative and qualitative analyses using archived surface and upper-air meteorological measurements. Since the intended purpose of this WRF dataset is for use in air quality models, performance in the PBL and at the surface is of particular concern. The quantitative assessment focuses on WRF performance at specific locations where wind, temperature, and humidity were measured at surface and upper-air radiosonde stations. A qualitative evaluation of precipitation across Alaska is also provided in this report.

Quantitative analysis is conducted using common statistical measures such as mean prediction error, root mean square error (RMSE), and mean prediction bias. The equations for these measures are given below where P is the predicted variable at a site and O is the observed variable at the site, determined over an incremental timeframe:

$$Mean\ Bias = \frac{1}{N}\sum_{i=1}^{N}(P_i - O_i)$$

$$RMSE = \sqrt{\frac{1}{N}\sum_{i=1}^{N}(P_i - O_i)^2}$$

$$Mean\ Error = \frac{1}{N}\sum_{i=1}^{N}|P_i - O_i|$$

The predicted values obtained from the WRF dataset are extracted from the grid points located nearest to the locations of the meteorological stations. However, the WRF grid point selected for any given station may not be representative of the meteorological conditions at that station, especially in complex terrain. For example, the meteorological station could be located in a valley, whereas the grid point could be located on an adjacent mountain peak. Given the 9 km horizontal resolution of the WRF dataset, the nearest grid point to any given station may be some distance from that station. Also, the WRF grid point is meant to represent the average conditions within the 9-km wide grid cell, rather than the conditions at a single point within that cell. These factors may contribute to an inherent degree of bias and error that is not necessarily an indication of poor model performance.

3.1 Surface meteorological parameters and performance criteria

WRF model performance was assessed by comparing modeled surface-layer meteorological parameters to measured values obtained from the Earth System Research Laboratory (ESRL) Meteorological Assimilation Data Ingest System (MADIS). The MADIS surface hourly dataset consists of hourly-averaged meteorological values collected mainly at airport ASOS and other official meteorological stations operated by government agencies. The assessment compared modeled hourly-averaged values of 10-m wind speed and wind direction and 2-m temperature and absolute humidity (in units of grams of water vapor per kilogram of dry air) to measured values. In total, 216 surface meteorological stations from the MADIS database were located within the 9 km domain and selected for the analysis. The selection included three stations in Russia and about 40 stations in Canada. Not every meteorological dataset contained enough data for analysis over all the periods examined.

3.1.1 Performance benchmarks

Several sets of benchmarks reported in the scientific literature have been developed to evaluate the performance of meteorological model datasets used for air quality modeling applications. EPA's Atmospheric Model Evaluation Tool (AMET) (EPA, 2019) uses a set of statistical performance goals in its "soccer plot" tool, based on common benchmarks for normalized bias and error (Appel, et al., 2011). Several sets of benchmarks, namely Emery et al. (2001) and Kemball-Cook et al. (2005), have been widely used in recent meteorological performance evaluations (Bowden, et al., 2015) (Bowden, et al., 2016) (Brashers, et al., 2015) (Brown, 2014) (Ramboll-Environ, 2015) and were adopted for use in this evaluation.

Emery et al. (2001) developed performance benchmarks for meteorological inputs to photochemical models drawing on the (Tesche, et al., 2001) evaluation of statistics from over 30 regional modeling datasets within the continental United States. Emery et al. selected a set of error and bias thresholds based on the 80th percentile performance values for 29 of the datasets. The majority of the datasets were developed at a horizontal resolution of 12 km using the MM5 or RAMS meteorological models.

Kemball-Cook et al. developed a model performance analysis of the Western Regional Air Partnership (WRAP) 2002 Alaska MM5 model dataset. It was noted, in their report, that the Emery et al. performance benchmarks were excessively stringent for model performance in regions of complex terrain or regions comprised of highly heterogeneous microclimates, such as most of Alaska. Kemball-Cook et al. adopted a less stringent set of benchmarks based on the previous performance of the 2002 WRAP Rocky Mountains and Sierra Nevada MM5 datasets. These benchmarks have been adopted for "complex conditions," as opposed to the "simple conditions" benchmarks of Emery et al.

The benchmarks used in this study are listed in **Table 4**. For complex conditions, Kemball-Cook et al. did not provide a benchmark for wind direction bias. Given the benchmark for wind direction error is roughly twice the value for complex conditions as the value for simple conditions, the EPA adopted a wind direction complex-conditions bias benchmark double the value for simple conditions.

Note, the EPA does not recommend using these benchmarks as a "pass/fail" indicator of dataset performance (EPA, 2018). The benchmarks are intended to be used to assess the general confidence in the representativeness of the model outputs. The benchmarks have been developed considering average bias and error over wide regions that include a number of surface stations. Therefore, the benchmarks are most useful for assessing performance on a regional basis. They can be used to evaluate performance on a single-station basis, but the modeler must use more caution in assuming the criteria are applicable to single-station performance.

Table 4. Surface meteorology performance benchmarks.

	Simple Conditions benchmarks based on Emery et al. (2001)		**Complex Conditions benchmarks** based on Kemball-Cook et al. (2005)	
	Bias	**Error[a]**	**Bias**	**Error[a]**
Wind speed	0.5 ms^{-1}	2.0 ms^{-1}	1.5 ms^{-1}	2.5 ms^{-1}
Wind direction	10°	30°	20° [b]	55°
Temperature	0.5° K	2.0° K	2.0° K	3.5° K
Absolute Humidity	1 g kg^{-1}	2 g kg^{-1}	1 g kg^{-1}	2 g kg^{-1}

[a] Wind speed benchmarks are based on RMSE, while others are mean absolute error.
[b] Kemball-Cook et al. does not provide a recommendation for wind direction bias. A value of 20° was assumed for this study, which is twice the simple conditions benchmark.

3.1.2 Qualitative analysis

In addition to quantitative evaluation of WRF performance using measures of error and bias, qualitative evaluation tools such as wind roses and time series of meteorological variables were developed for this assessment. Hour-of-day time series of temperature, wind speed, and humidity were developed on a seasonal basis for both the measured and modeled parameters at each meteorological station location.

3.2 Selected sub-regions for analysis

The State of Alaska is a large landmass roughly 20% the size of the contiguous United States, that encompasses a significant range of climates. Five subdomains were selected to facilitate the performance evaluation based on the division of climates and regions of strategic importance with regards to air quality regulation. Subregion performance is judged by comparison of a subdomain-wide average error and bias on a monthly basis against the benchmarks identified in Section 3.1.

The first domain, referred to as the "North Slope" domain, encompasses surface weather stations located at 12 sites along the Arctic coast of Alaska, spanning from Point Hope (PAPO) to Barter Island (PABA). Included in the domain are Alaskan village sites such as Nuiqsut (PATQ) and Utqiagvik (PABR). The North Slope domain is of particular importance from an air quality perspective due to the large number of existing and planned oil and gas facilities at Prudhoe Bay and locations within the National Petroleum Preserve.

A plot of the domain, including positions of the meteorological stations, is shown in **Figure 2**.

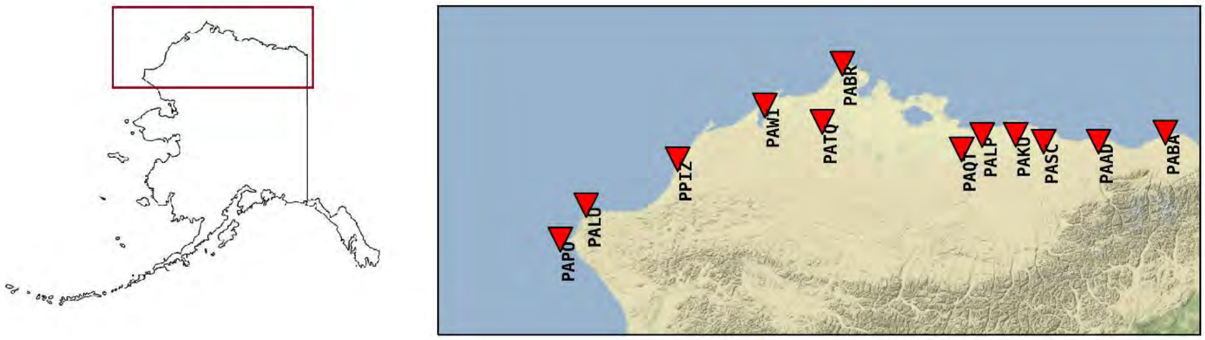

Figure 2. North Slope domain.

The second domain selected for regional analysis is the "Fairbanks" domain, which encompasses five surface meteorological stations in the vicinity of the city of Fairbanks. This area is of particular interest from an air quality perspective due to persistently high $PM_{2.5}$ concentrations in the Fairbanks area. In 2009, the EPA designated parts of the Fairbanks North Star Borough as nonattainment for the 2006 24-hour $PM_{2.5}$ National Ambient Air Quality Standards, and in 2017, the EPA reclassified the area from a "moderate to a "serious" nonattainment area. The domain contains the Fairbanks International airport (PAFA) and Nenana airport (PANN) airport meteorological stations, as well as Eielson Airforce Base (PAEI), Allen Army Airfield (PABI), and Wainwright AAF airport (PAFB) stations.

A plot of the Fairbanks domain and selected meteorological stations is shown in **Figure 3**.

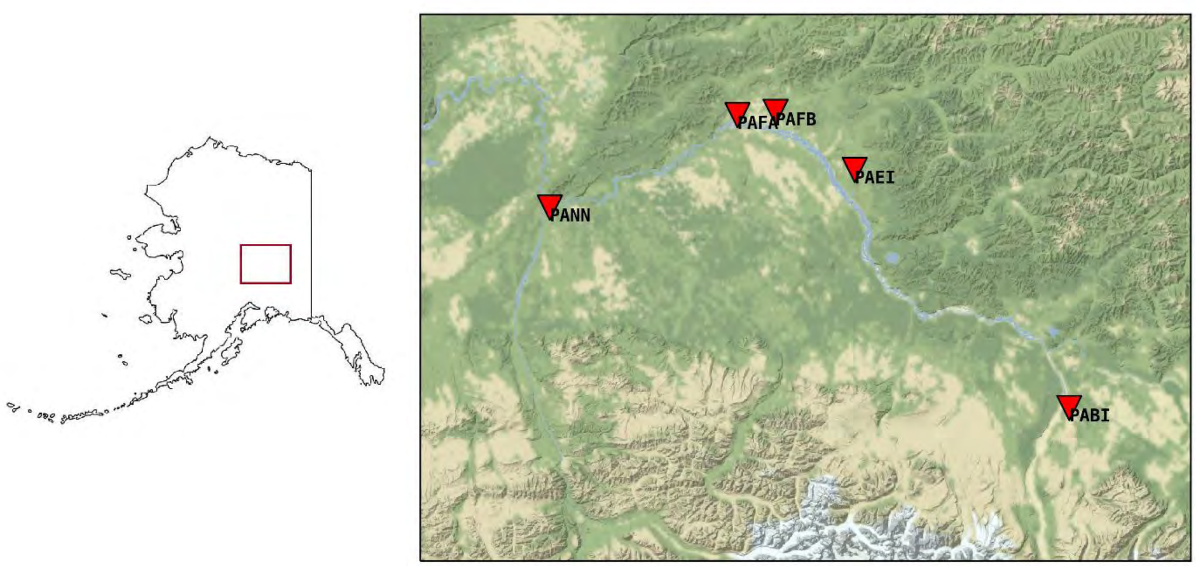

Figure 3. Fairbanks domain.

The third sub-region selected for analysis is the “Cook Inlet” domain. This domain consists of 12 meteorological stations located within the Anchorage metropolitan area and along the coast of the Cook Inlet. This area of Alaska is of particular concern because most of the state’s population resides in the Anchorage metropolitan area and because there is a significant concentration of industry across the Cook Inlet area. Also, offshore oil and gas facilities are located in the Cook Inlet. Development of additional offshore facilities within the Cook Inlet are possible in the future. The domain is shown in **Figure 4**.

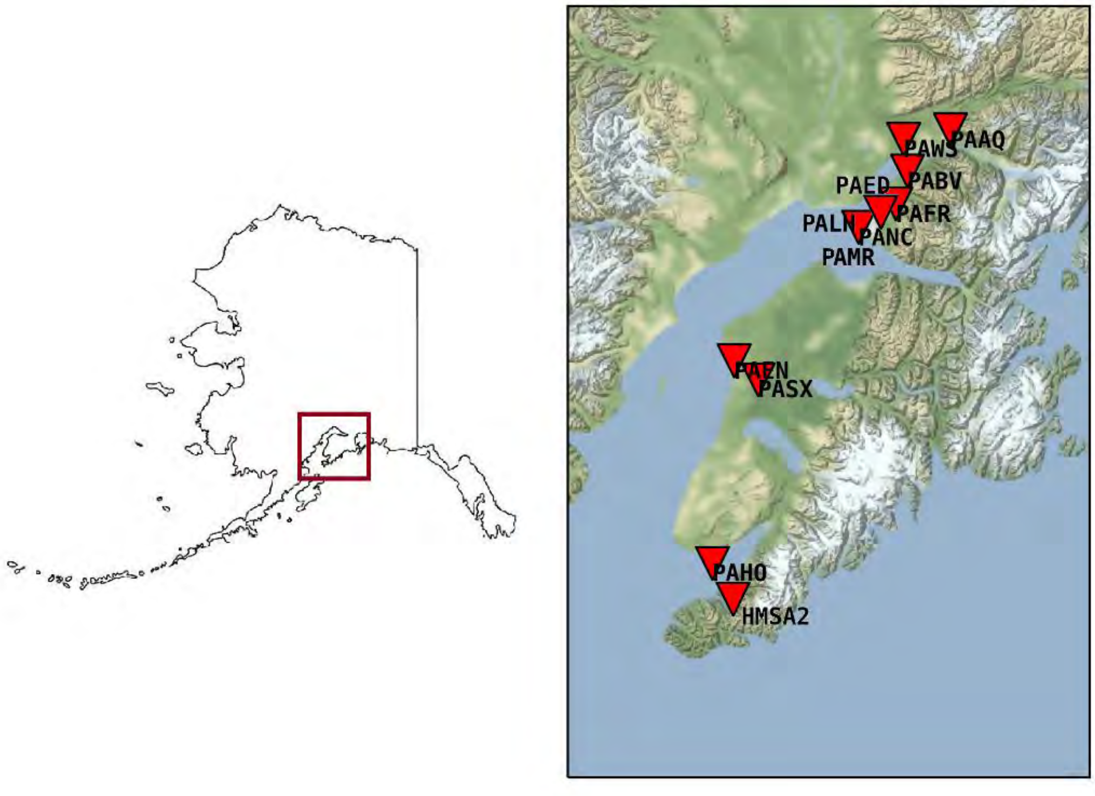

Figure 4. Cook Inlet domain.

The fourth subregion selected for the analysis is the “Juneau” domain. Although this area is currently not a significant concern from an air quality perspective, the area encompasses the state capitol and a significant portion of the state population. The region is also subject to the shipping emission impacts from heavy industrial and cruise ship traffic. The region contains highly complex terrain and a variety of microclimates. The domain is centered on the Juneau International airport station (PAJN) and contains stations as far south as Wrangell airport (PAQG) and far north as Haines (PAHN). The domain is shown in **Figure 5**.

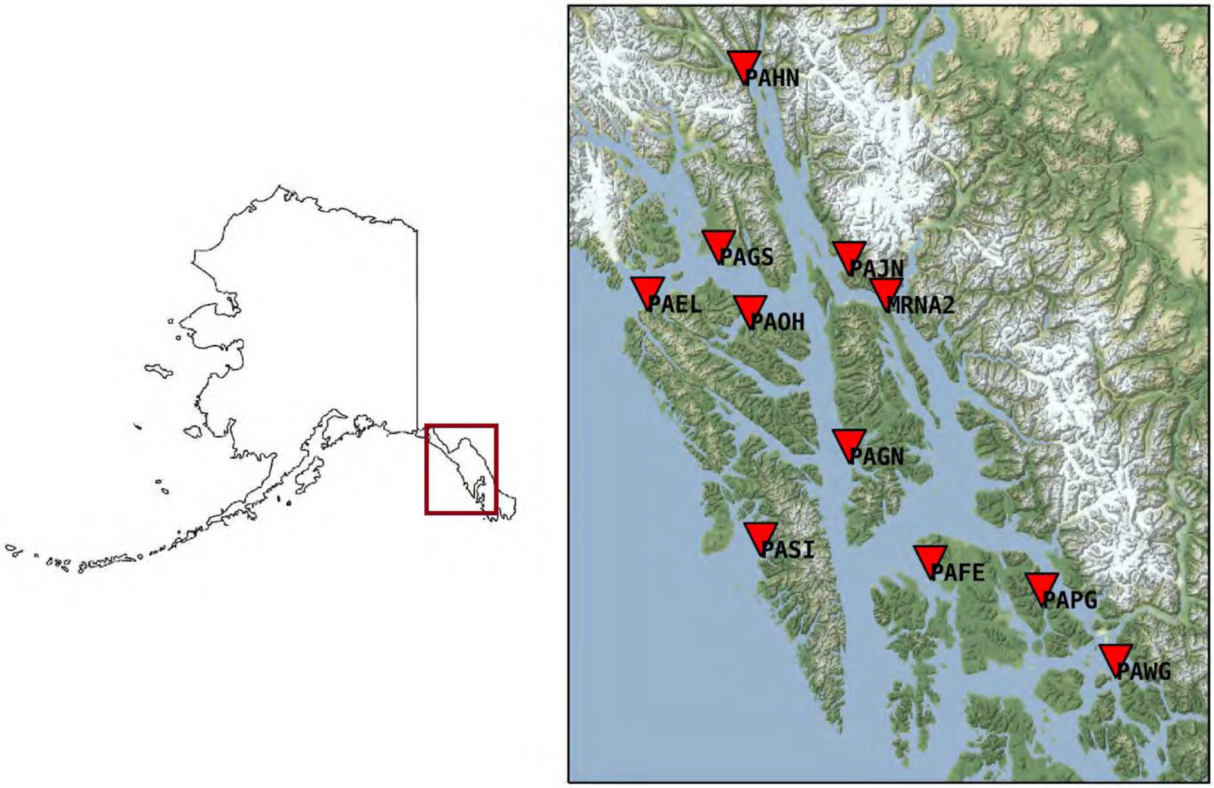

Figure 5. Juneau domain.

The fifth subregion selected for the analysis is the “Alaska Peninsula” domain. This domain encompasses meteorological stations located on Kodiak Island, along the Alaska Peninsula, and on several of the Aleutian Islands. This domain also contains several areas of concentrated industrial activity including Dutch Harbor and Kodiak. The domain and selected meteorological stations are plotted in **Figure 6.**

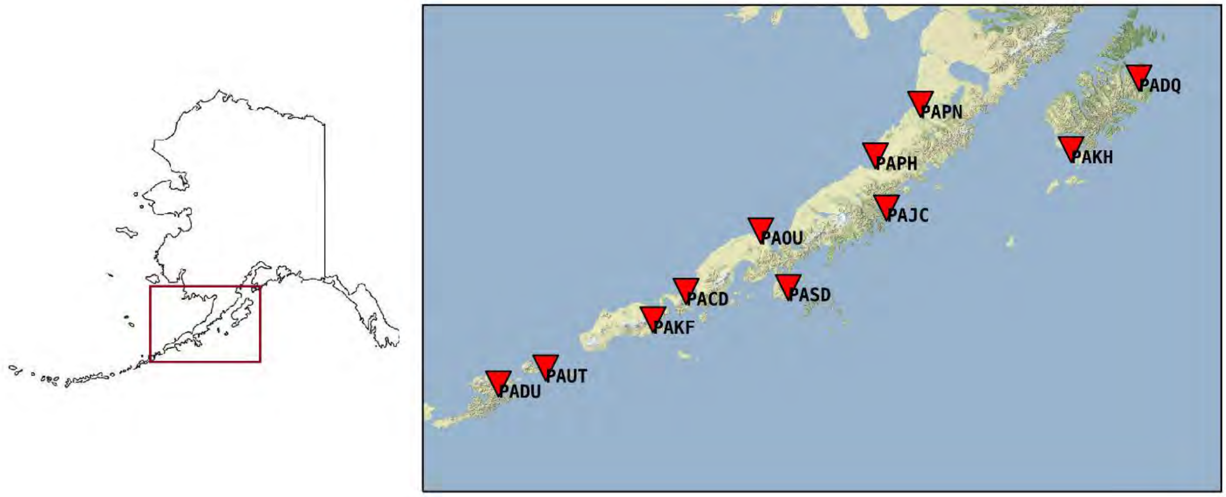

Figure 6. “Alaska Peninsula” domain.

3.3 Upper-air evaluation

A set of 16 upper-air meteorological station datasets were obtained for the model performance evaluation. The set consists of the 13 stations operated by the National Weather Service in Alaska as well as three stations located in Canada. Upper-air stations deploy radiosonde instruments on weather balloons, released twice daily just prior to hours 0 and 12 UTC, each day. The radiosondes measure wind, temperature, and humidity through the atmospheric column. Profiles of hourly-averaged wind, temperature, and humidity were obtained from the WRF grid cell nearest to the location of each upper-air station at times corresponding with the radiosonde measurements. The station identifiers and locations are plotted in **Figure 7**.

Performance was assessed using a set of boxplots to describe the distribution of residuals of wind speed, wind direction, temperature, and humidity for each of the four seasons. Seasons were defined as winter (December, January, February), spring (March, April, May), summer (June, July, August), and autumn (September, October, November). The residuals (the difference between the modeled and measured values) were calculated for pressure levels 1000, 925, 850, 700, 500, 400, and 300 mb.

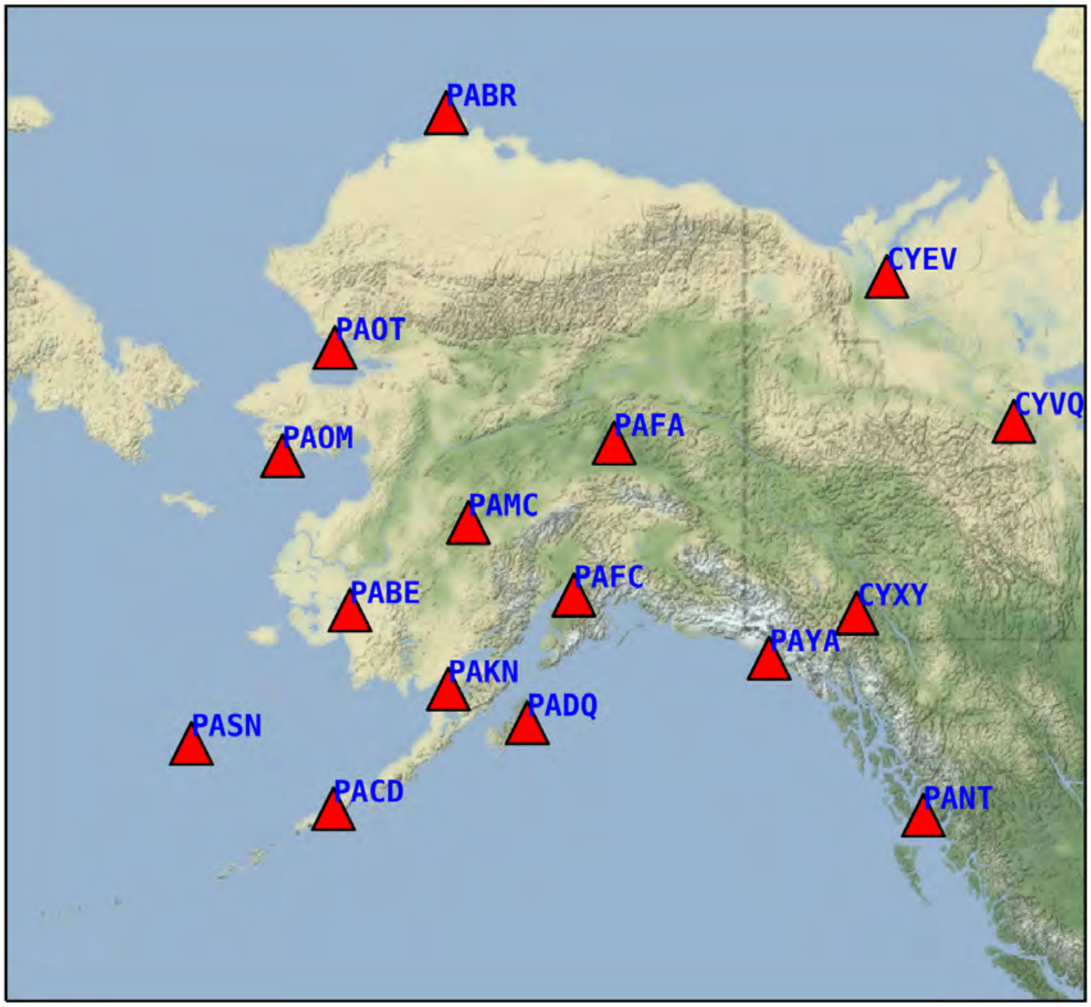

Figure 7. Upper-air stations selected for the model performance study.

3.4 Precipitation

A qualitative evaluation of precipitation was conducted using monthly-averaged precipitation maps for the state of Alaska. Monthly total precipitation maps for the state of Alaska were obtained from the National Centers for Environmental Prediction (NCEP) Alaska climate monitoring database (NOAA-NCEP, 2019). These maps were developed using the gridded 5-km NOAA "nClimGrid" dataset, developed from the Global Historical Climatology Network (GHCN). The GHCN dataset is a daily 5-km resolution grid of meteorological variables, including precipitation, determined using measured surface data. Climatologically aided spatial interpolation is used to assign daily average values to each grid point from the available measurements (Vose, et al., 2014). Precipitation datasets used to develop the grids are obtained from the COOP, ASOS, RAWS, and SNOTEL networks.

Monthly-averaged precipitation maps provided by the NOAA-NCEP tool are compared to plots of state-wide monthly average precipitation values determined from the 2016 Alaska WRF model (in inches of liquid-equivalent precipitation).

4. Model performance evaluation results

Bias and error were determined for each hourly-average wind speed, wind direction, temperature, and humidity record available by comparison of WRF outputs to measurements. The average bias and error results were evaluated on a domain-wide scale (bias and error averaged from all stations in the 9-km domain) and also on a regional scale in this section (bias and error averaged from meteorological stations located in each subdomain). The plots for a selection of individual stations of interest are also analyzed in this section. The plots of all other individual surface and upper-air stations that are not reviewed in the body of this report are available in electronic format from the EPA upon request (Appendix A).

4.1 Domain-wide surface parameters

Domain-wide performance is evaluated using error/bias “soccer plots” that compare monthly averaged error and bias against the adopted benchmarks presented in Section 3.1.1. This evaluation is used to assess the likelihood of systematic error driven by selection of parameterization schemes or other factors that could impact domain-wide performance.

4.1.1 Temperature

The domain-wide soccer plot for surface temperature is shown in **Figure 8**. The plot demonstrates the domain-wide surface temperature tends to be biased cold, particularly in winter and spring. However, the bias is within the criteria for complex conditions, except in March, which is slightly outside of the bounds. Temperature error is also within the complex criteria, except for December, which slightly exceeds the benchmark.

Domain-wide temperature bias per month is illustrated in **Figure 9** through **Figure 14** through a plot of all stations in the domain shaded by the magnitude of bias. The regional bias maps in these figures demonstrate the domain-wide average cold bias, evident in the soccer plot, is mainly driven by bias along the North Slope and coastal areas of the Seward Peninsula during winter and spring months.

Surface temperatures are biased warm in the early winter months in the eastern Alaska interior and Yukon interior. These stations are generally located within steep valleys in mountainous areas. Further examination of precipitation and snow cover would be needed to investigate the bias, but it is assumed the bias is due to incorrect parameterization of the surface energy bias possibly due to error in snow cover.

The temperature bias over summer months is very low, and within the bounds of simple condition benchmarks.

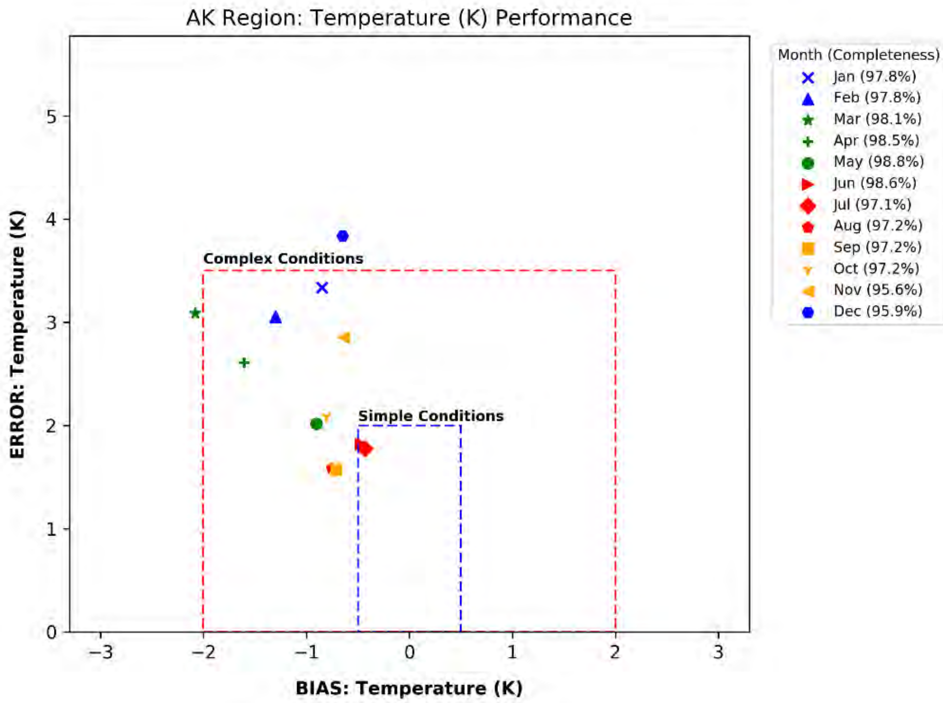

Figure 8. Soccer plot of monthly 2-m temperature error and bias averaged over the 9 km Alaska domain for 2016.

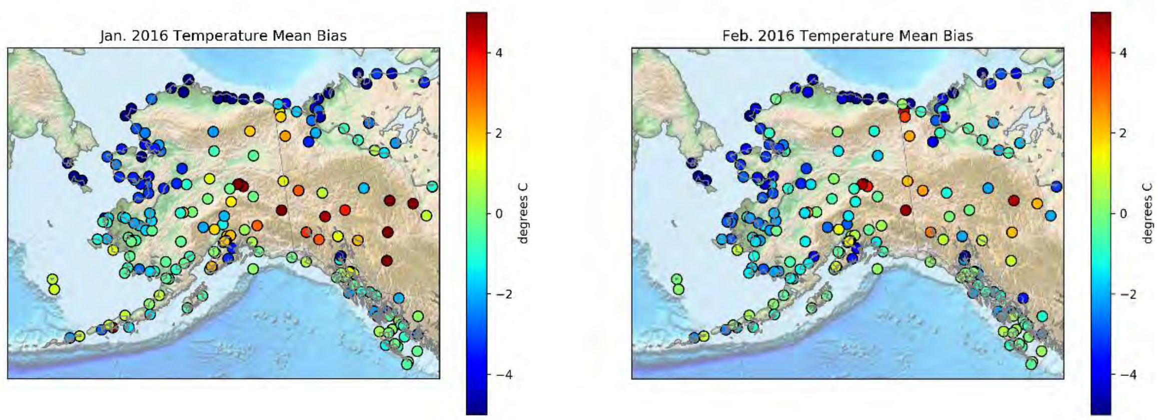

Figure 9. Monthly mean temperature bias, January (left) and February (right) 2016.

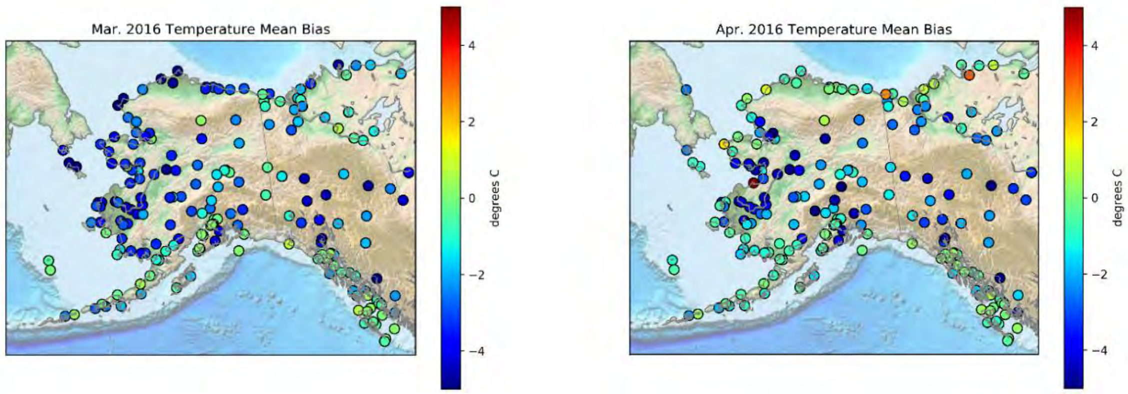

Figure 10. Monthly mean temperature bias, March (left) and April (right) 2016.

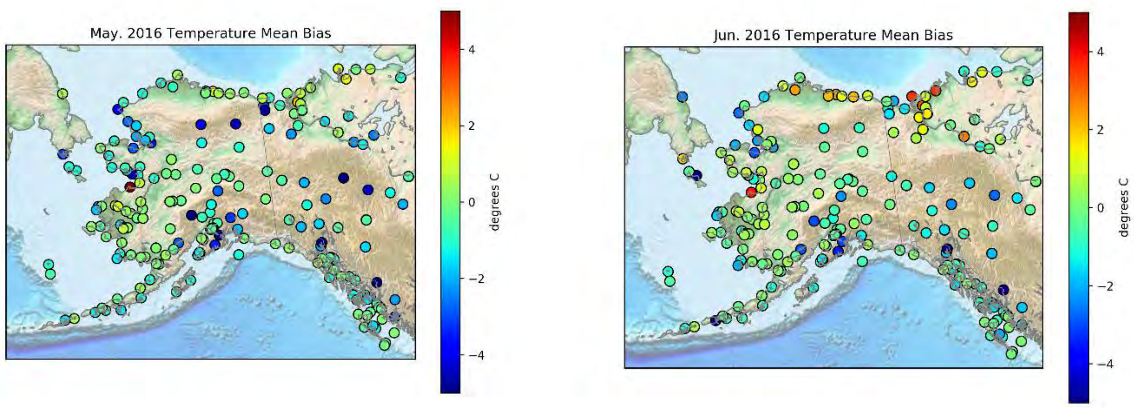

Figure 11. Monthly mean temperature bias, May (left) and June (right) 2016.

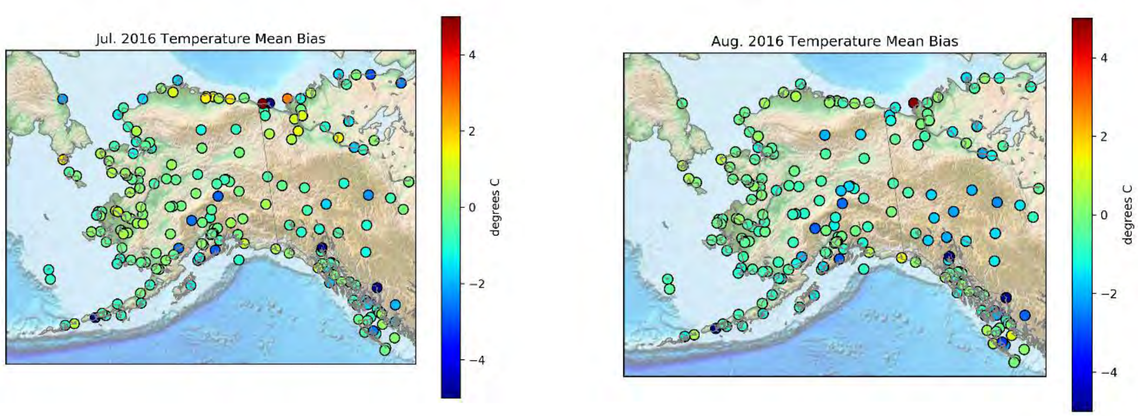

Figure 12. Monthly mean temperature bias, July (left) and August (right) 2016.

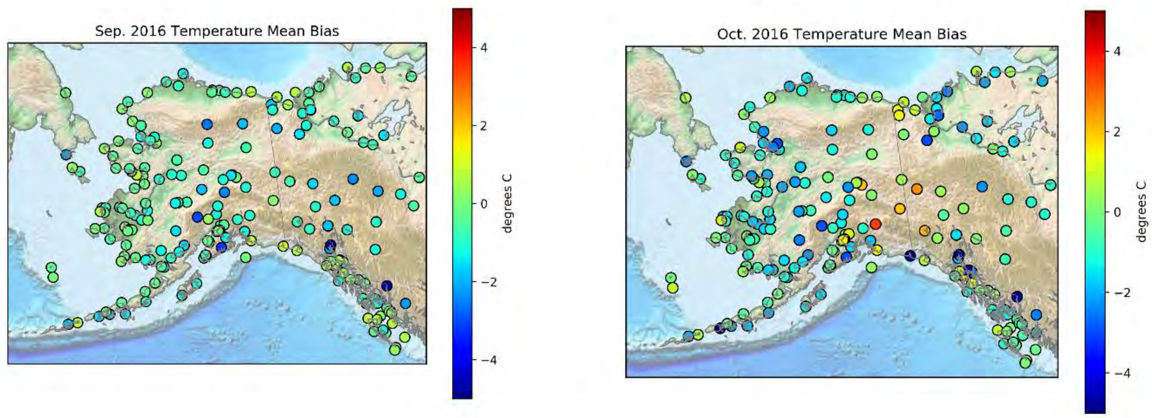

Figure 13. Monthly mean temperature bias, September (left) and October (right) 2016.

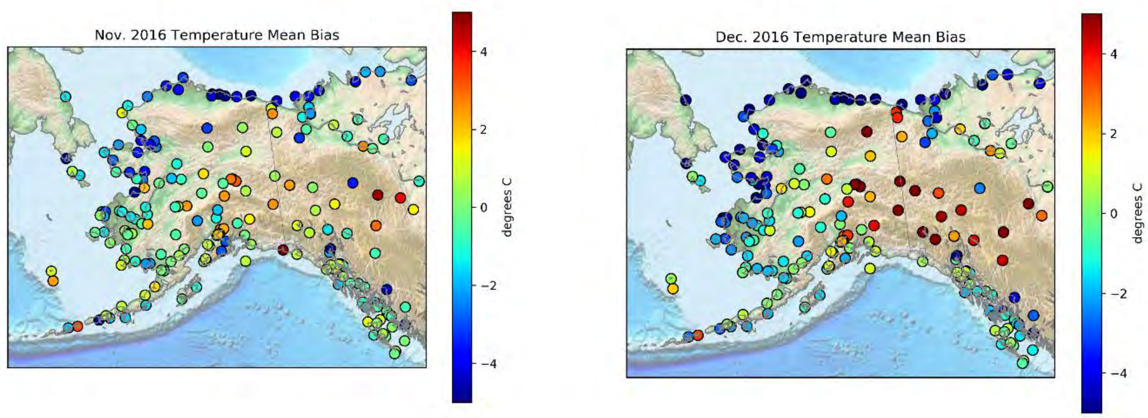

Figure 14. Monthly mean temperature bias, November (left) and December (right) 2016.

4.1.2 Wind speed

The domain-wide soccer plot for surface wind speed is shown in **Figure 15**. The plot demonstrates the domain-wide surface wind speed tends to be just slightly biased low, but all within the criteria for simple conditions. However, wind speed error tends to slightly exceed complex criteria for the winter months. The error and bias appear to be driven mainly by a low wind speed bias along the coastal regions of the North Slope and Seward peninsula during winter months, as shown in **Figure 16** through **Figure 21**.

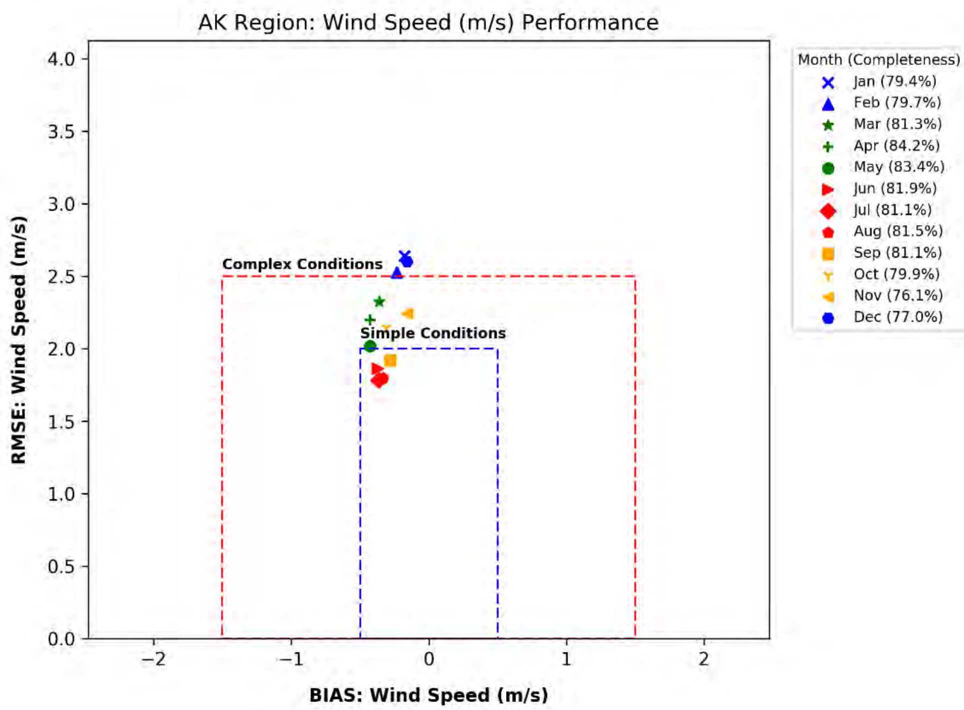

Figure 15. Soccer plot of monthly 10-m wind speed error and bias averaged over the 9 km Alaska domain for 2016.

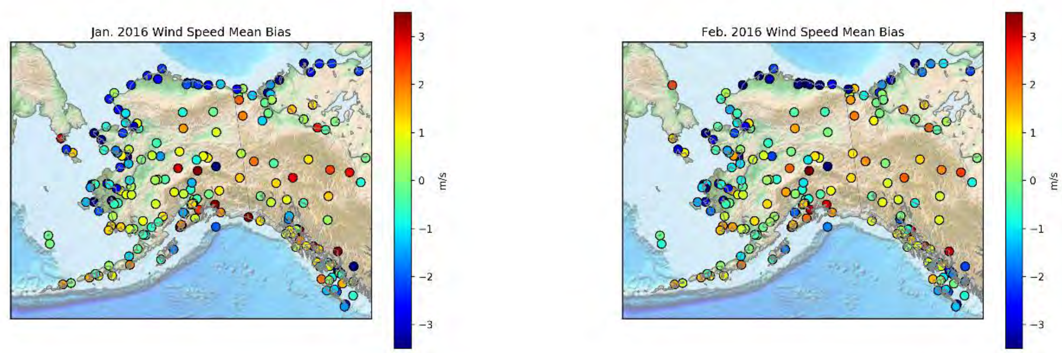

Figure 16. Monthly mean wind speed bias, January (left) and February (right) 2016.

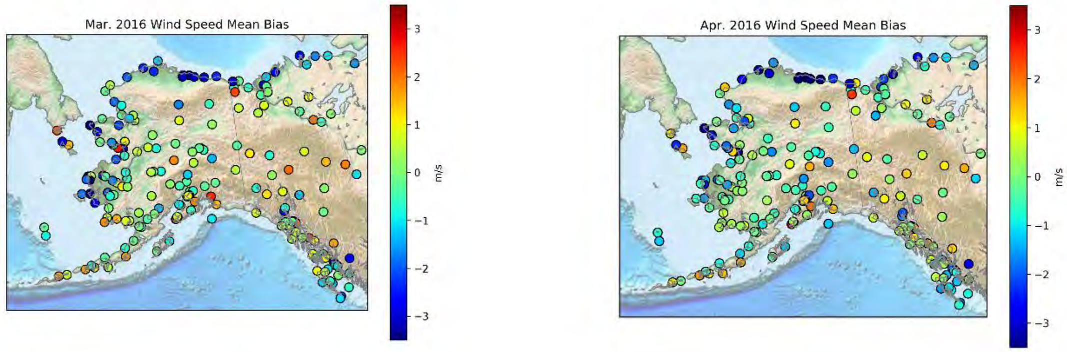

Figure 17. Monthly mean wind speed bias, March (left) and April (right) 2016.

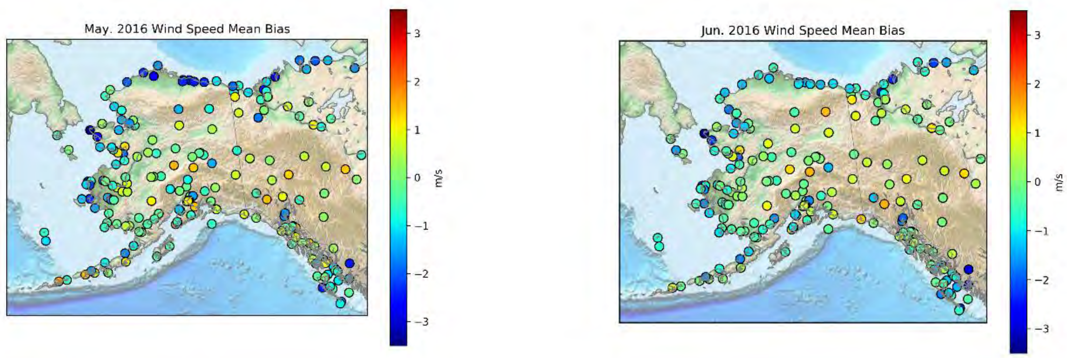

Figure 18. Monthly mean wind speed bias, May (left) and June (right) 2016.

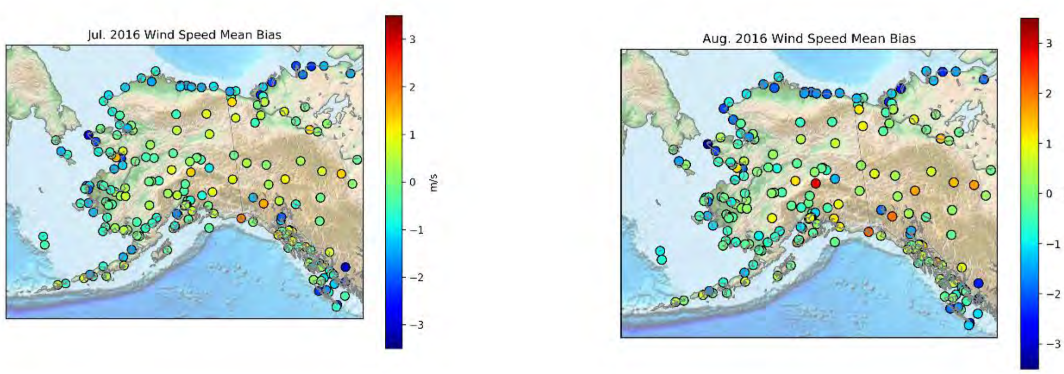

Figure 19. Monthly mean wind speed bias, July (left) and August (right) 2016.

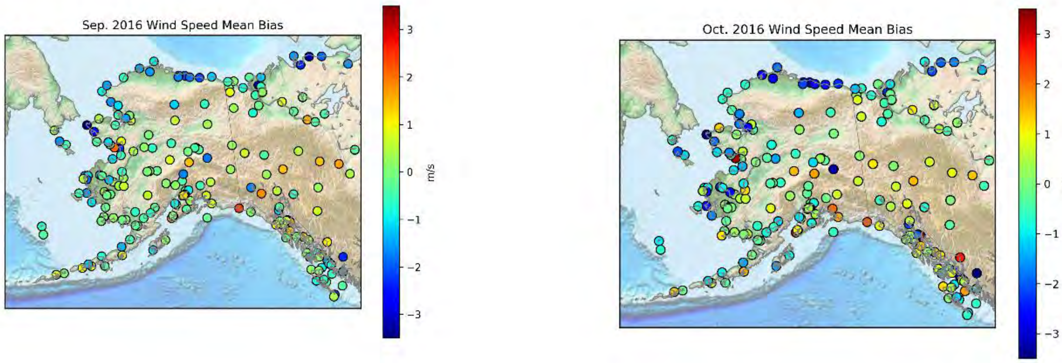

Figure 20. Monthly mean wind speed bias, September (left) and October (right) 2016.

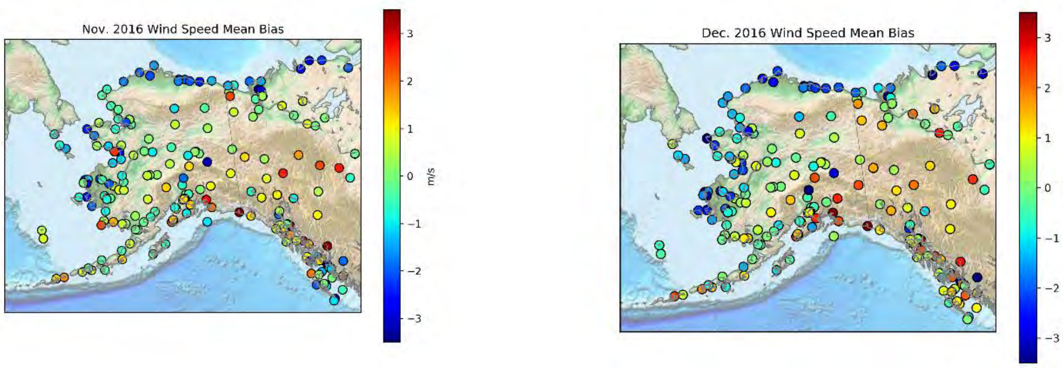

Figure 21. Monthly mean wind speed bias, November (left) and December (right) 2016.

4.1.3 Wind direction

The domain-wide soccer plot for surface wind direction is shown in **Figure 22**. Wind direction bias is very low on average. Wind direction error exceeds simple criteria but falls within the complex benchmark criteria. The distribution of wind direction error per month is shown in **Figure 23** through **Figure 28**. Wind direction error is greatest in the inland mountainous regions of eastern Alaska and the Yukon. High wind direction error in mountainous areas is not necessarily an indication of poor WRF performance. Observations are typically representative of mountain valleys where airports are located and where the wind climate is generally aligned with the terrain. At 9 km resolution, WRF provides an average wind vector across an area that can easily contain several mountain peaks and valleys in a single grid cell.

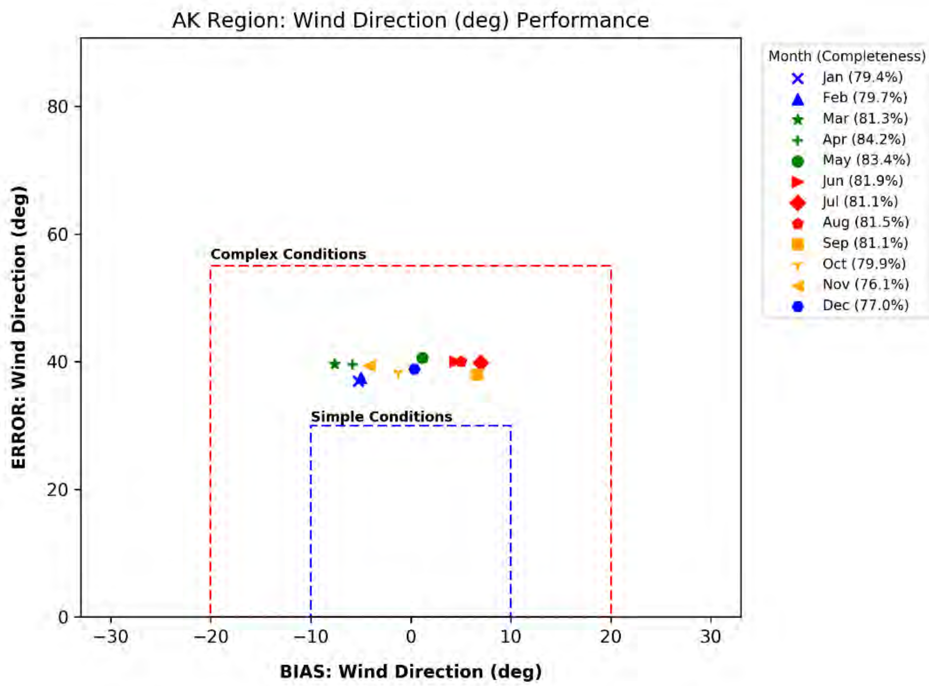

Figure 22. Soccer plot of monthly 10-m wind direction error and bias averaged over the 9 km Alaska domain for 2016.

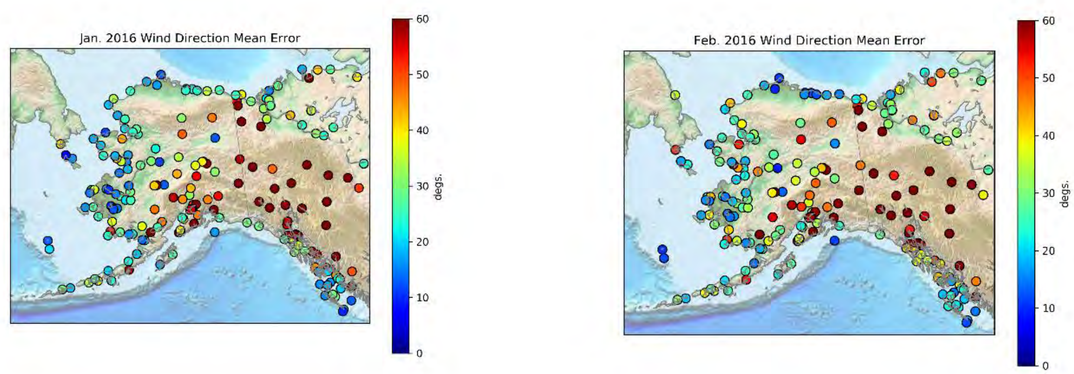

Figure 23. Monthly mean wind direction error, January (left) and February (right) 2016.

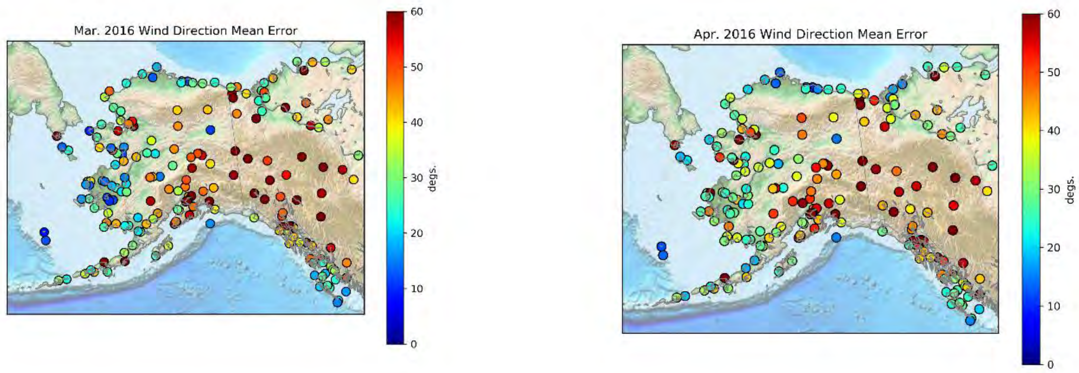

Figure 24. Monthly mean wind direction error, March (left) and April (right) 2016.

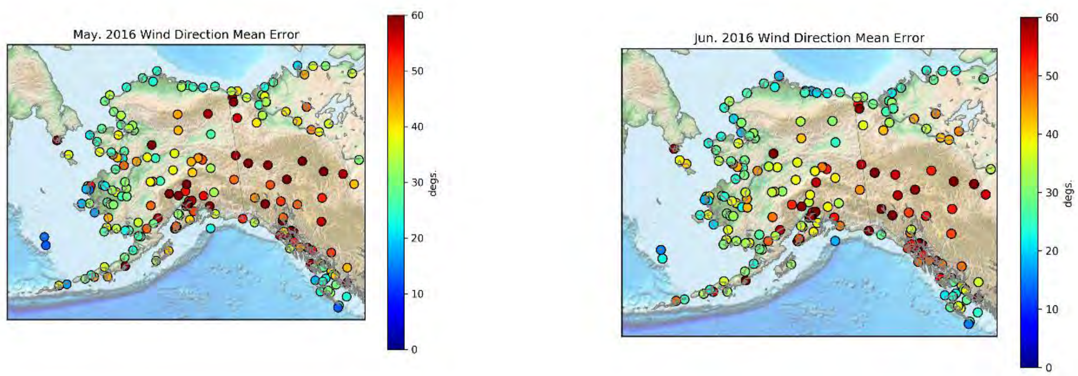

Figure 25. Monthly mean wind direction error, May (left) and June (right) 2016.

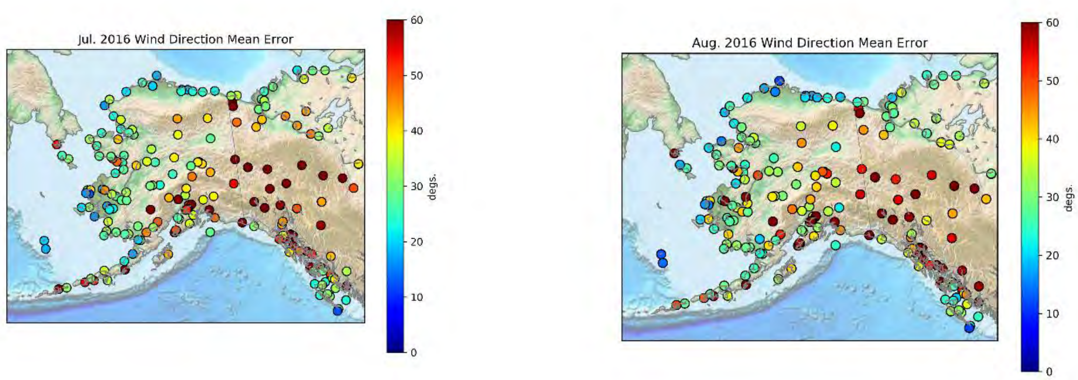

Figure 26. Monthly mean wind direction error, July (left) and August (right) 2016.

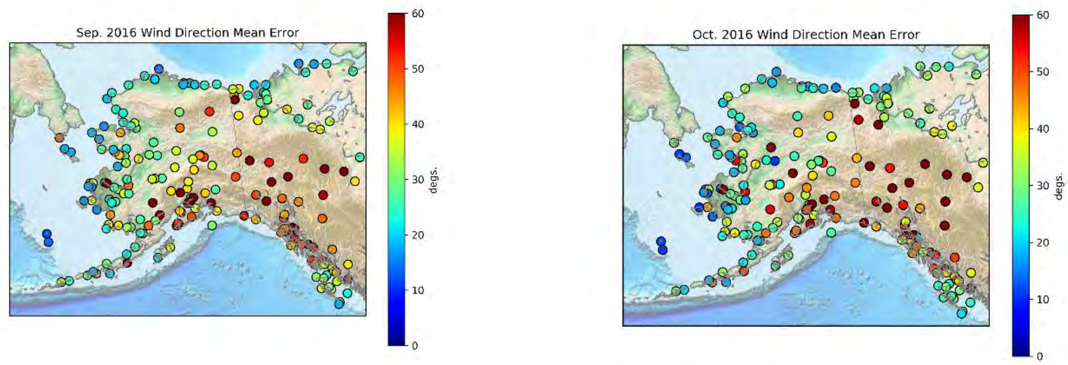

Figure 27. Monthly mean wind direction error, September (left) and October (right) 2016.

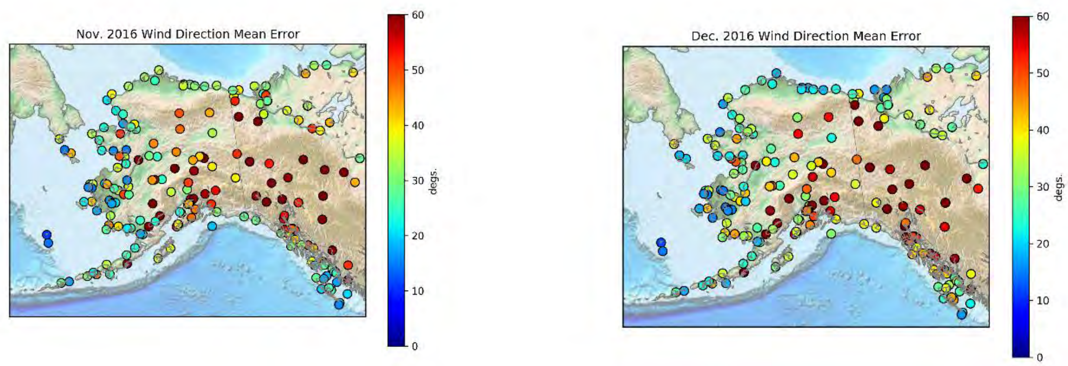

Figure 28. Monthly mean wind direction error, November (left) and December (right) 2016.

4.1.4 Humidity

The domain-wide soccer plot for surface absolute humidity is shown in **Figure 29**. WRF performance is within the benchmark criteria all months. There are no regions with significant absolute humidity bias through any season, as seen in **Figure 30** through **Figure 35**.

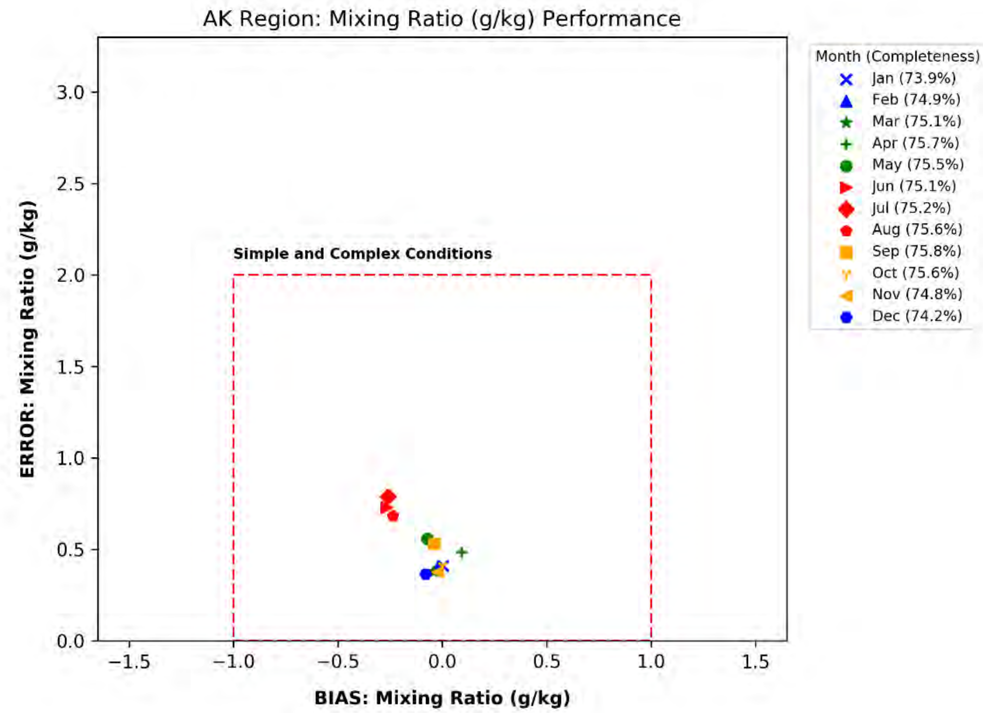

Figure 29. Soccer plot of monthly absolute humidity error and bias averaged over the 9 km Alaska domain for 2016.

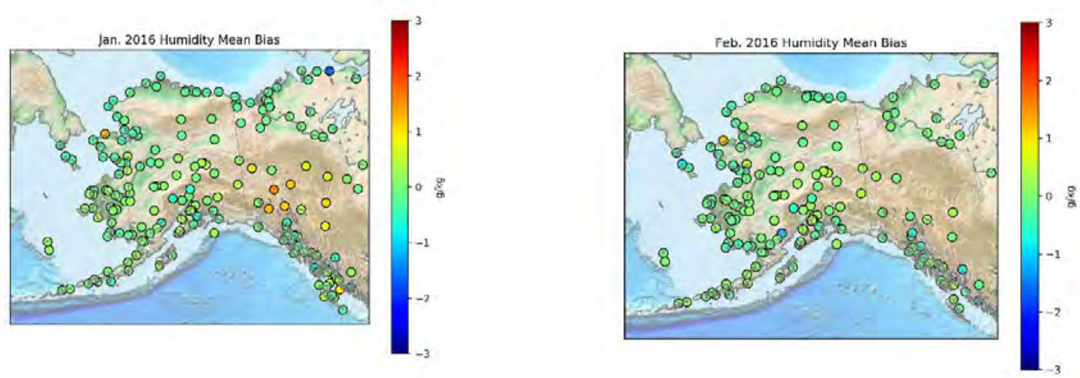

Figure 30. Monthly mean humidity bias, January (left) and February (right) 2016.

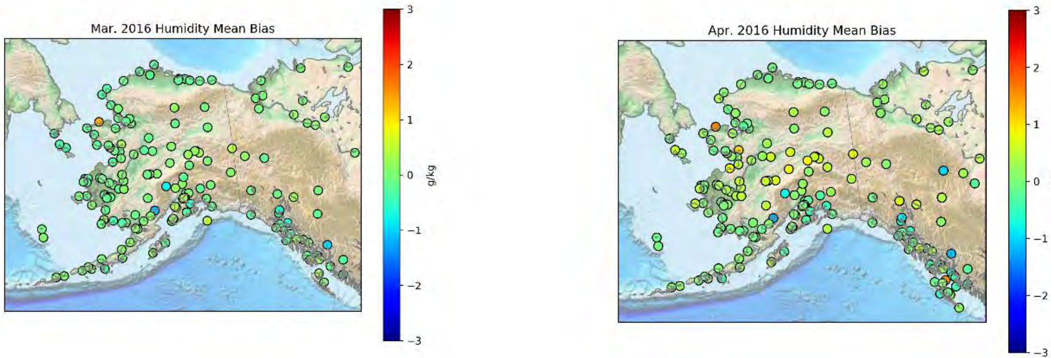

Figure 31. Monthly mean humidity bias, March (left) and April (right) 2016.

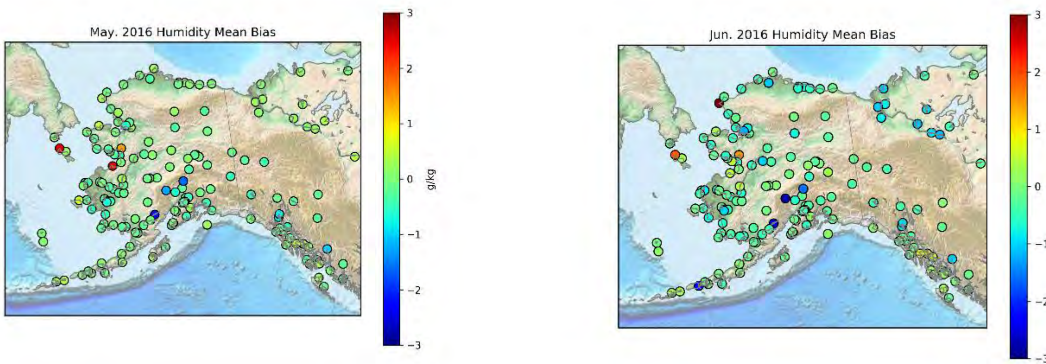

Figure 32. Monthly mean humidity bias, May (left) and June (right) 2016.

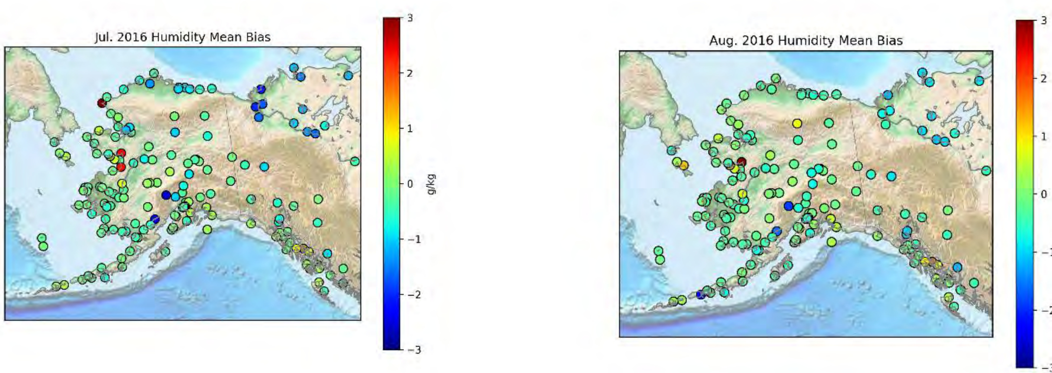

Figure 33. Monthly mean humidity bias, July (left) and August (right) 2016.

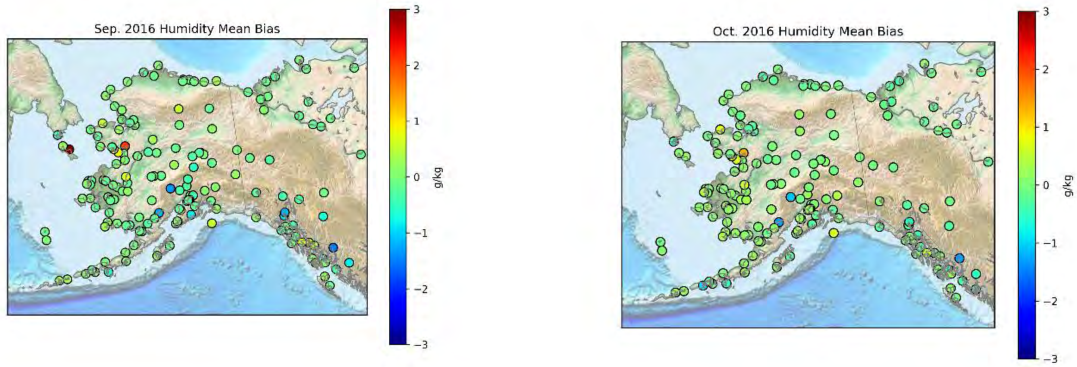

Figure 34. Monthly mean humidity bias, September (left) and October (right) 2016.

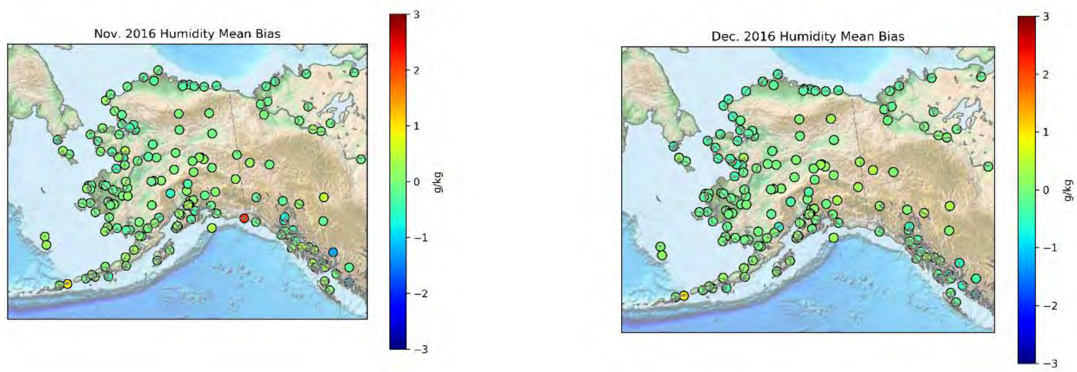

Figure 35. Monthly mean humidity bias, November (left) and December (right) 2016.

4.2 Cook Inlet region performance

Cook Inlet regional performance was assessed using soccer plots to analyze average error and bias across all stations in the subdomain. Also, Anchorage International airport (PANC) was selected as the individual station of interest for the analysis because it is located in the largest metropolitan area in the region. Temperature, wind, and humidity performance is examined over the subregion and at the individual station of interest.

4.2.1 Temperature

A plot of temperature distribution at PANC, examined by hour per season is shown in **Figure 36**. The distributions match well except WRF is biased low during summer nighttime and early morning hours. This could be partially explained by the local urban heat island effect at the monitor, which would be muted across a 9 km grid cell.

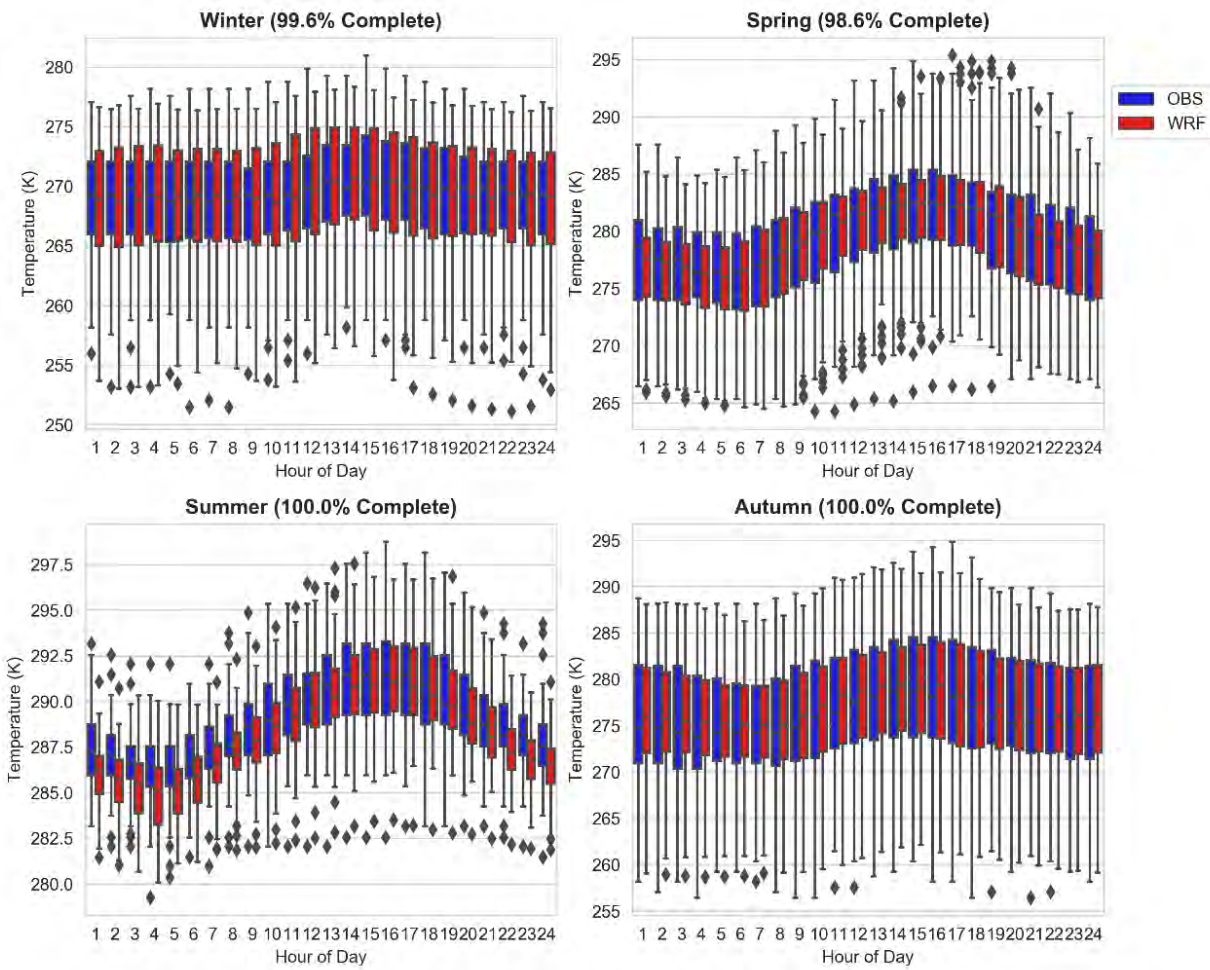

Figure 36. PANC (Anchorage) seasonal, hour-of-day temperature distributions, ASOS (blue) vs. Alaska 9-km WRF (red).

The regional average temperature error and bias soccer plot is shown in **Figure 37**. All results are within the complex conditions benchmark criteria. Winter-time temperatures are biased high, but still within the criteria.

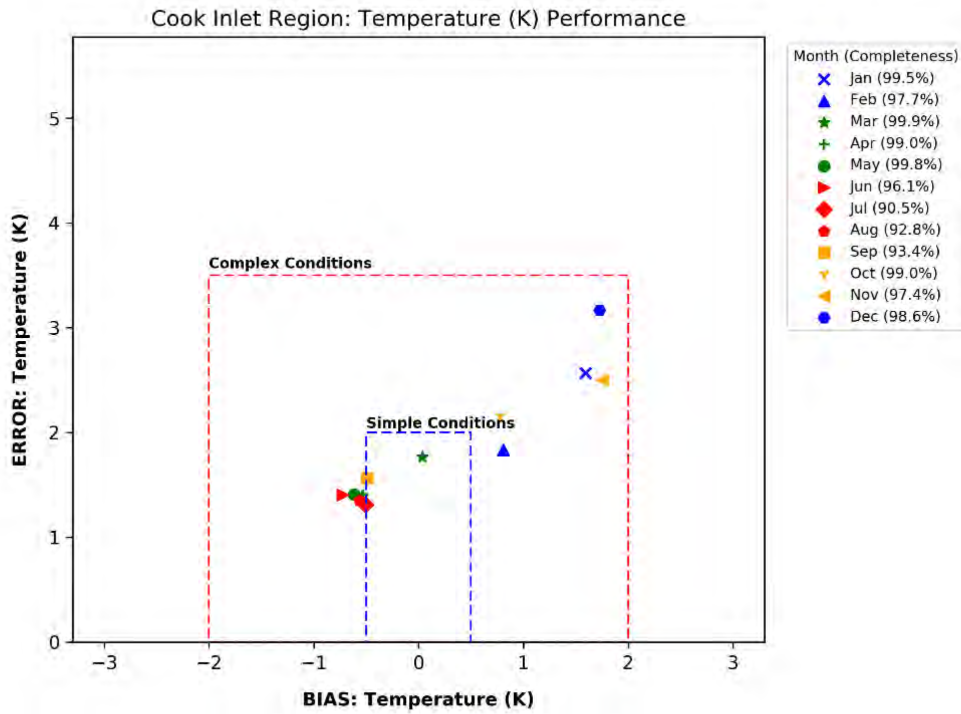

Figure 37. Soccer plot of monthly 2-m temperature error and bias averaged over the Cook Inlet subdomain for 2016.

4.2.2 Wind speed

Wind rose plots developed from both the observed (PANC) and modeled datasets are included in **Figure 38**. WRF simulates the modes of predominant wind well at PANC but appears to overpredict wind speed on average.

A plot of wind speed distribution at PANC, examined by hour per season is shown in **Figure 39**. WRF consistently overpredicts wind speed all hours of the day every season. The overprediction could be a result of the local surface roughness in the area of the PANC ASOS station. The ASOS station is likely subject to higher roughness than what is "seen" by the 9-km wide WRF grid cell. The grid cell encompasses areas over the water west and south of Anchorage and therefore represents a region of lower surface roughness than what is representative in the immediate vicinity of PANC.

The regional average wind speed error and bias soccer plot is plotted in **Figure 40**. All results are within the complex conditions criteria. Wind speed on average is unbiased and winter-time error is higher than error during the other seasons.

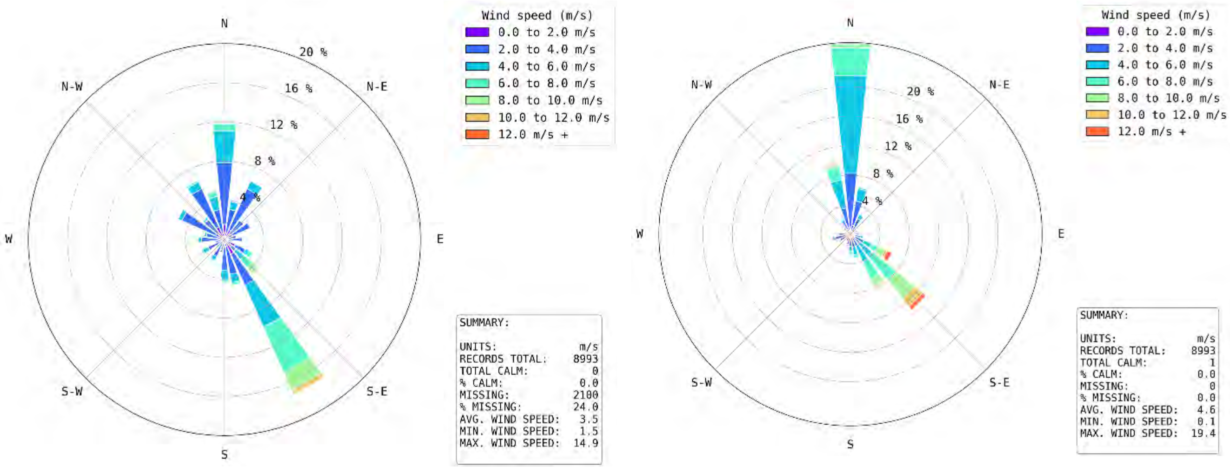

Figure 38. Wind rose comparison, PANC (Anchorage), ASOS observed (left), Alaska 2016 WRF (right).

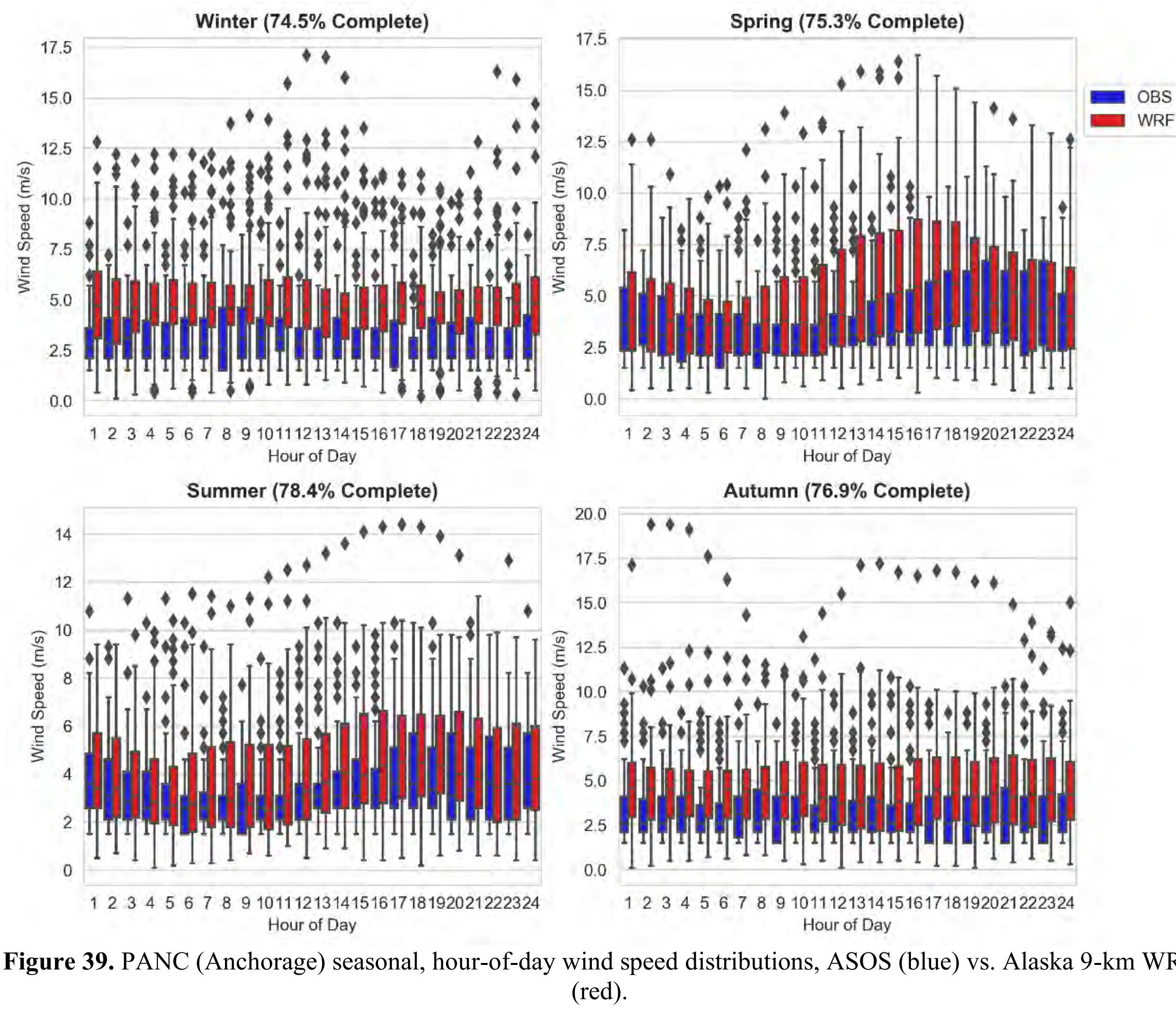

Figure 39. PANC (Anchorage) seasonal, hour-of-day wind speed distributions, ASOS (blue) vs. Alaska 9-km WRF (red).

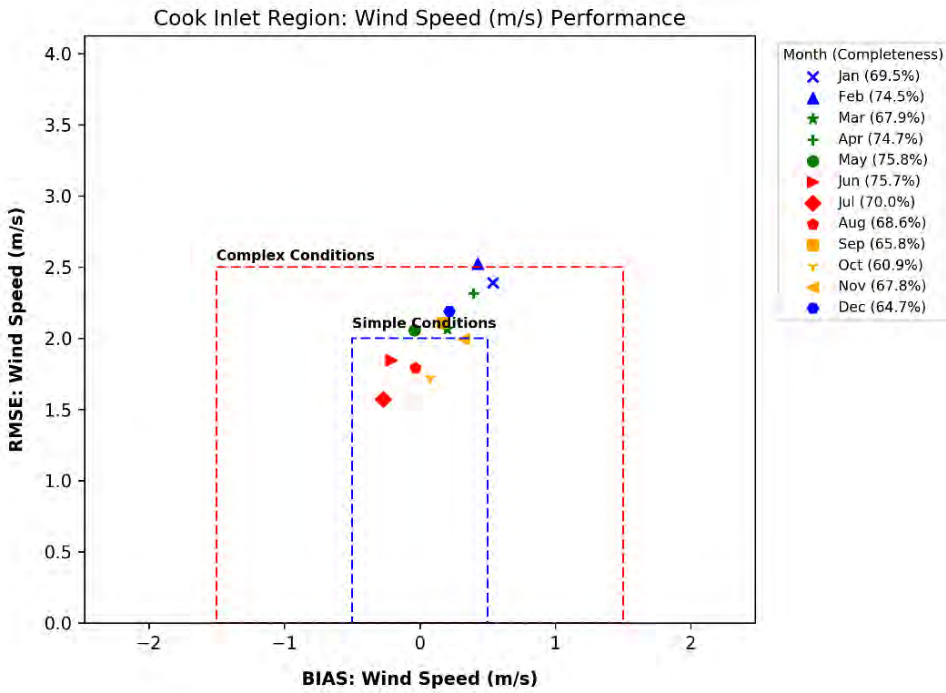

Figure 40. Soccer plot of monthly wind speed error and bias averaged over the 9 km Cook Inlet domain for 2016.

4.2.3 Wind direction

The wind direction monthly bias and error plot of the Cook Inlet subdomain is shown in **Figure 41**. The subdomain monthly average error exceeds the simple conditions criteria but generally falls within the complex condition benchmarks. The subregion bias is higher during the winter and spring months, with only April slightly exceeding the criteria.

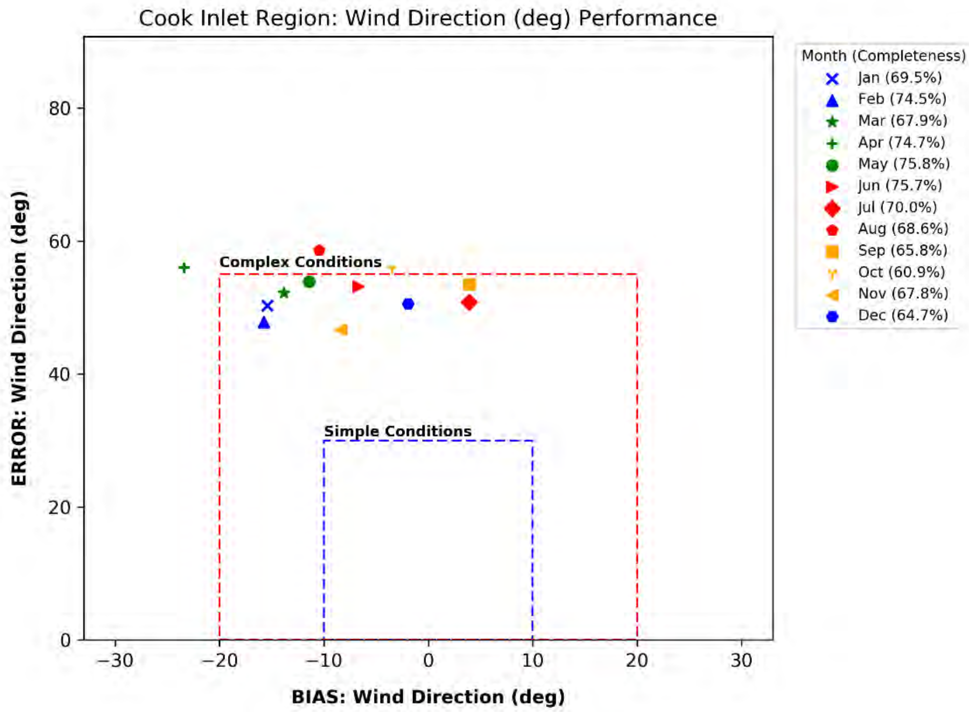

Figure 41. Soccer plot of monthly wind direction error and bias averaged over the Cook Inlet domain for 2016.

4.2.4 Humidity

A plot of the PANC station distributions of absolute humidity by hour of day per season is shown in **Figure 42**. The results demonstrate the WRF model tended to slightly overpredict daytime humidity during winter months on average and underpredict morning humidity during summer months.

The Cook Inlet subdomain humidity soccer plot is shown in **Figure 43**. The plot demonstrates WRF humidity performance has low bias and error and within the criteria.

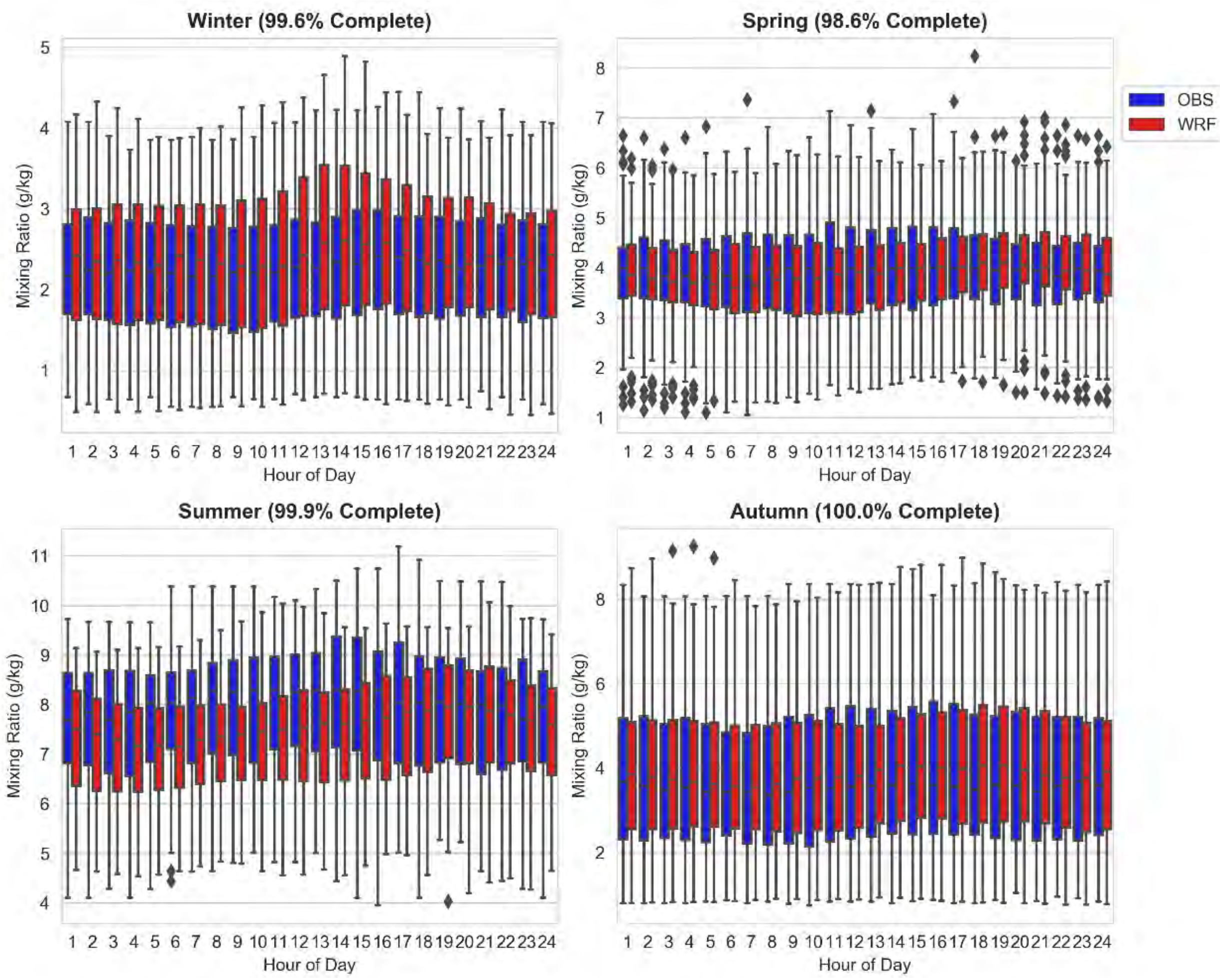

Figure 42. PANC (Anchorage) seasonal, hour-of-day absolute humidity distributions, ASOS (blue) vs. Alaska 9-km WRF (red).

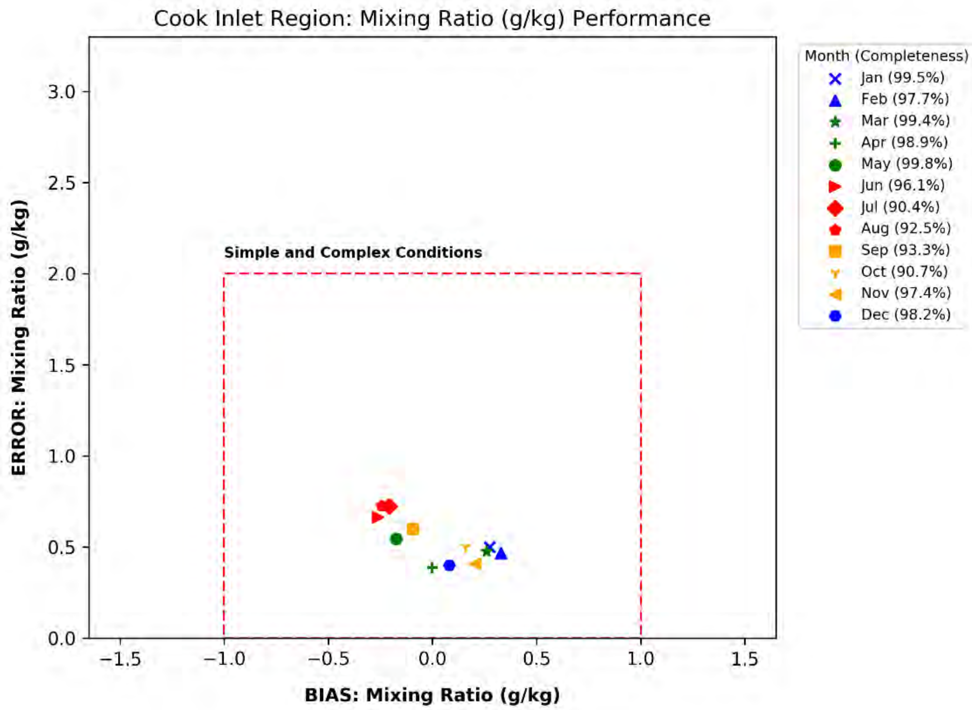

Figure 43. Soccer plot of monthly absolute humidity error and bias averaged over the Cook Inlet subdomain for 2016.

4.3 Fairbanks region performance

The Fairbanks subregion performance was assessed using soccer plots to analyze average error and bias across all stations in the subdomain. Also, Fairbanks International airport (PAFA) was selected as the individual station of interest for the analysis. Temperature, wind, and humidity performance is examined in this section for the subregion and at the individual station of interest.

4.3.1 Temperature

A plot of temperature distribution at PAFA, examined by hour per season is shown in **Figure 44**. The distributions match well in spring and autumn. The WRF model is biased warm all hours of the day in winter on average. Also, WRF is biased slightly cold all hours of the day over the summer.

The soccer plot of bias and error across the Fairbanks subregion is shown in **Figure 45**. The regional bias matches that of PAFA, with WRF highly overpredicting temperature in winter months and slightly underpredicting temperature in the spring and summer. WRF winter temperature bias and error falls outside the complex conditions criteria.

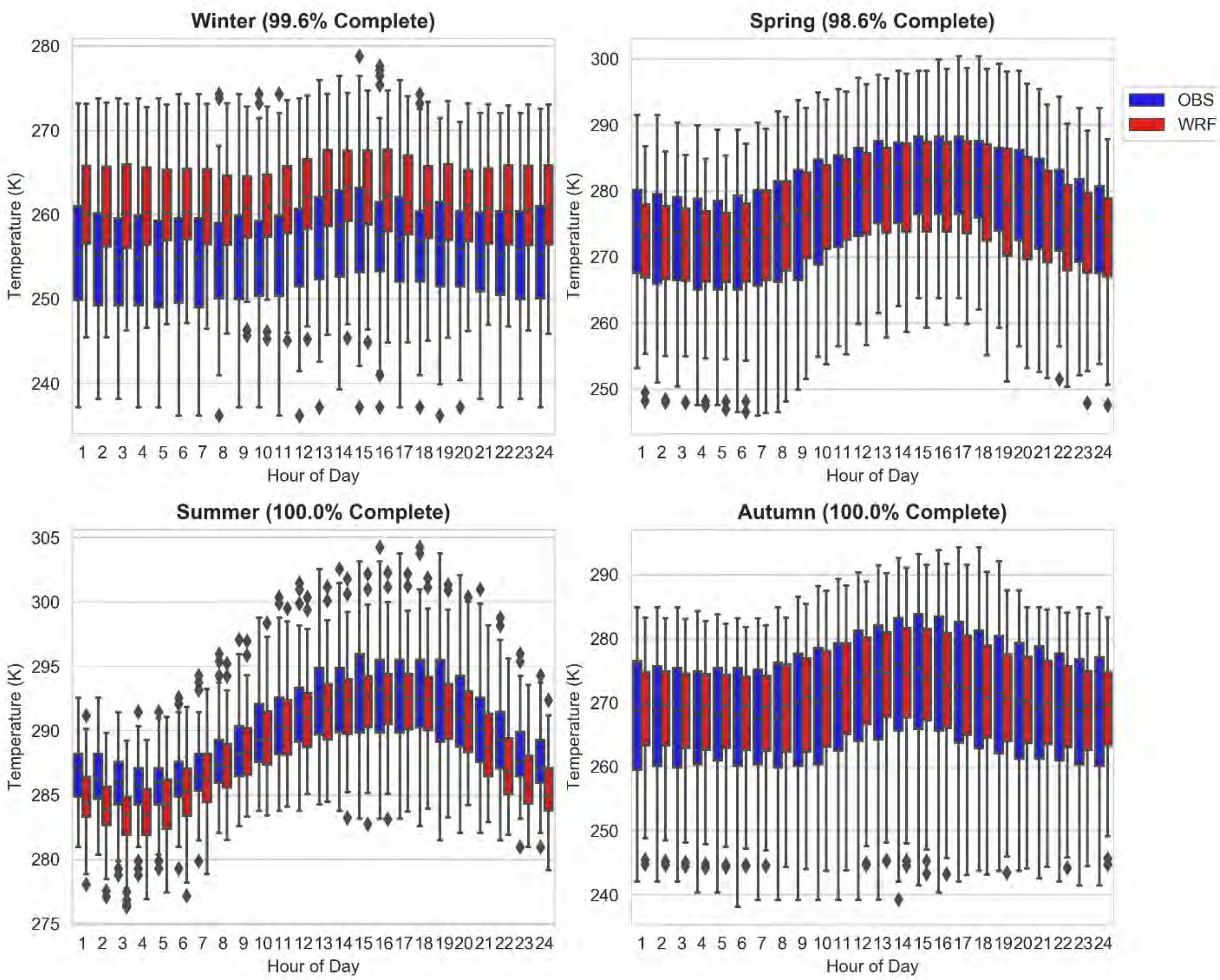

Figure 44. PAFA (Fairbanks) seasonal, hour-of-day temperature distributions, ASOS (blue) vs. Alaska 9-km WRF (red).

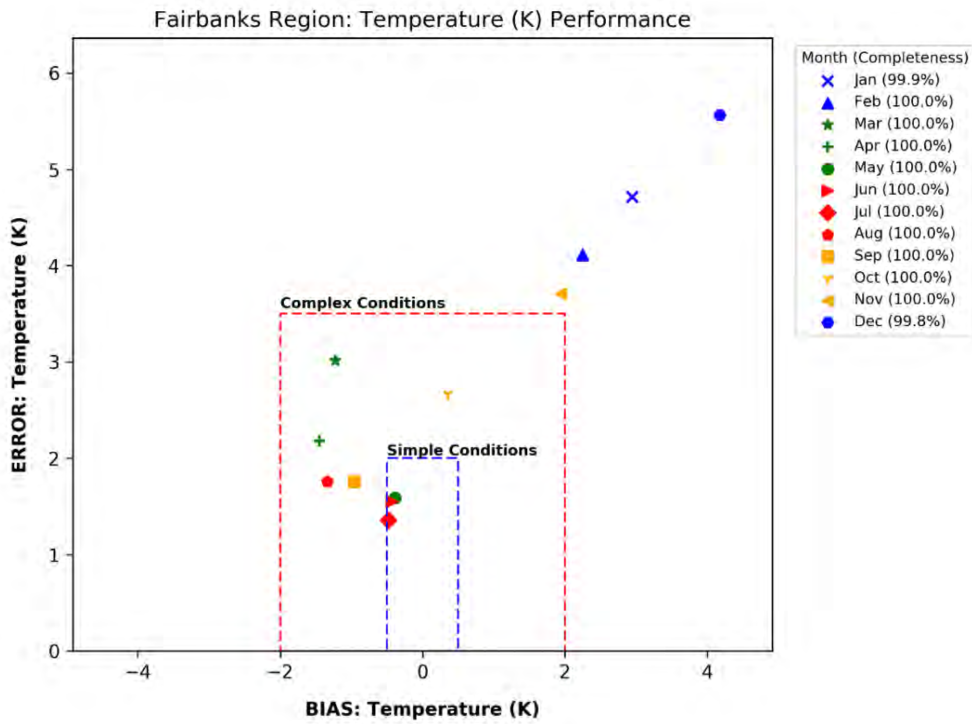

Figure 45. Soccer plot of monthly 2-m temperature error and bias averaged over the Fairbanks subdomain for 2016.

4.3.2 Wind speed

Wind roses developed from both the observed (PAFA) and modeled datasets are shown in **Figure 46**. WRF simulates the modes of predominant northeast and southwest winds well but appears to underpredict frequency and strength of high wind speed events. A plot of wind speed distribution at PAFA, examined by hour per season is shown in **Figure 47**. WRF tends to overpredict wind speed on average in the winter, but underpredict in the spring at PAFA.

The regional average wind speed error and bias soccer plot for the Fairbanks subregion is plotted in **Figure 48**. Wind speed appears to be biased low all months of the year, but well within the complex criteria. Wind speed error is within the complex criteria for all months except January, which slightly exceeds the criteria.

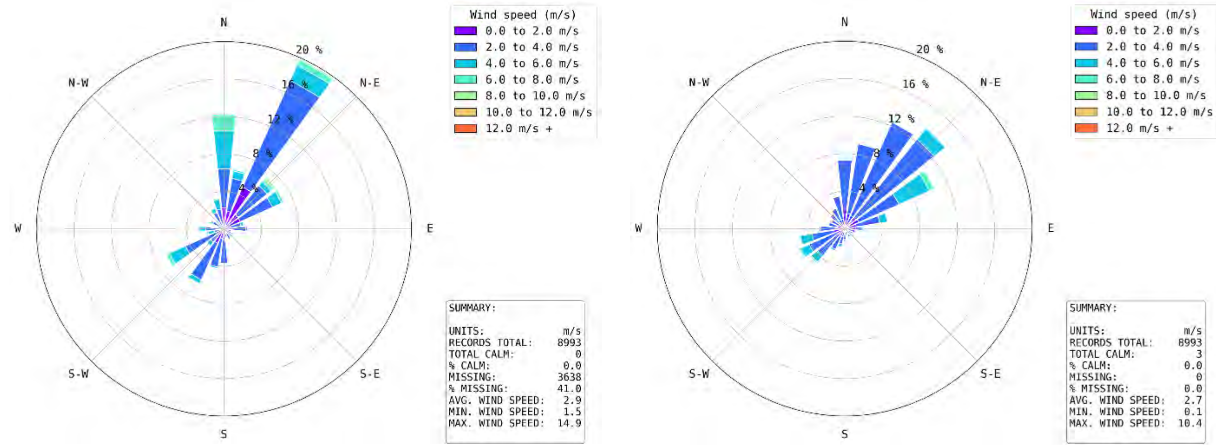

Figure 46. Wind rose comparison, PAFA (Fairbanks), ASOS observed (left), Alaska 2016 WRF (right).

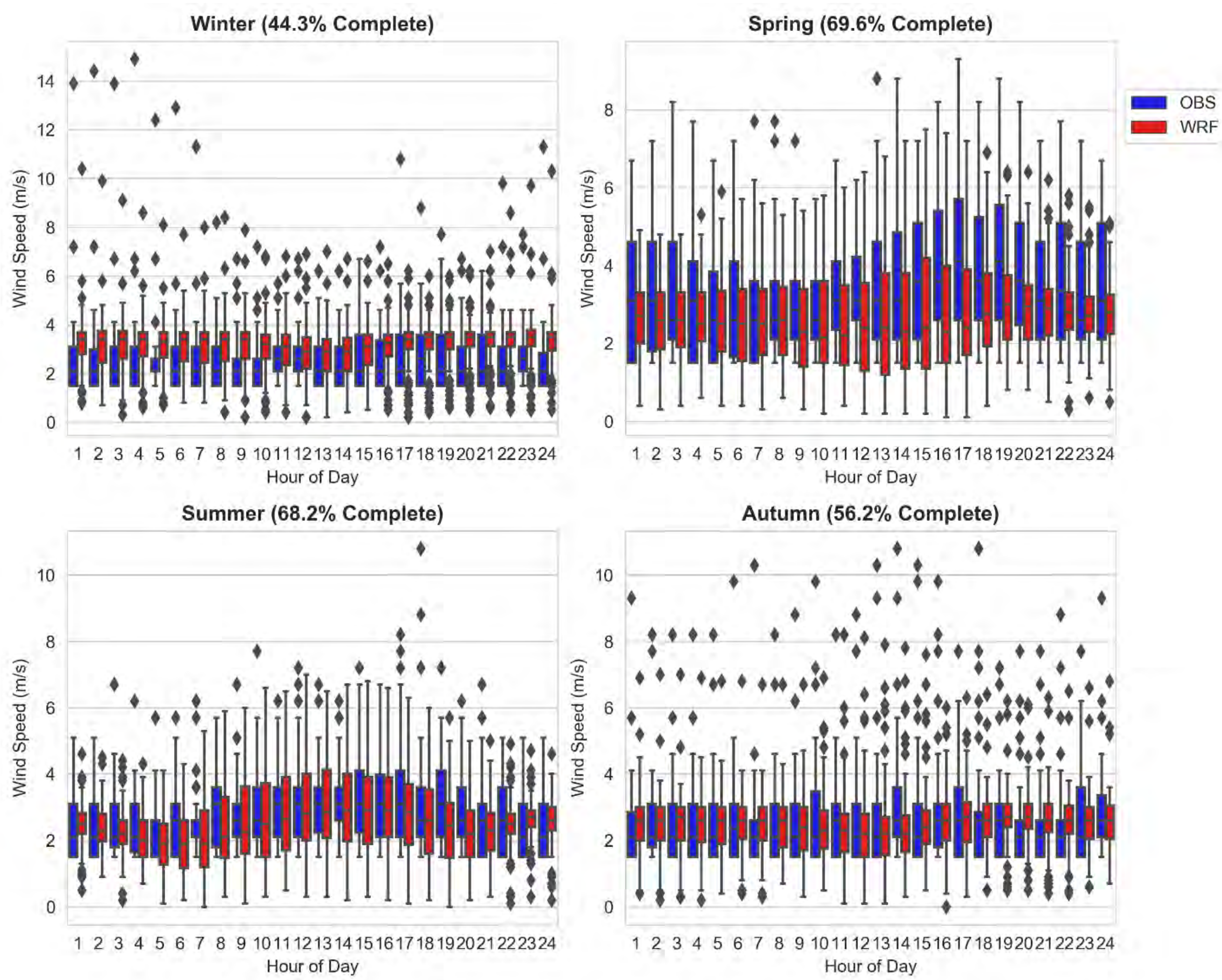

Figure 47. PAFA (Fairbanks) seasonal, hour-of-day wind speed distributions, ASOS (blue) vs. Alaska 9-km WRF (red).

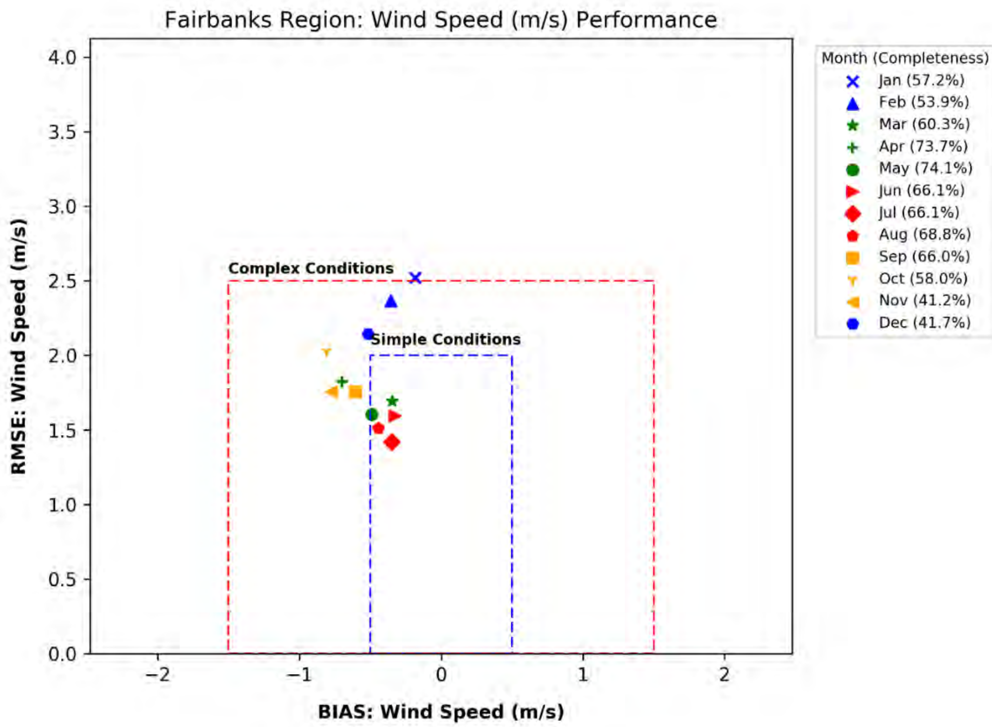

Figure 48. Soccer plot of monthly wind speed error and bias averaged over the Fairbanks subdomain for 2016.

4.3.3 Wind direction

The Fairbanks subdomain wind direction monthly bias and error is plotted in **Figure 49**. Average wind direction error falls within the complex conditions criteria and average bias generally falls within the simple conditions criteria.

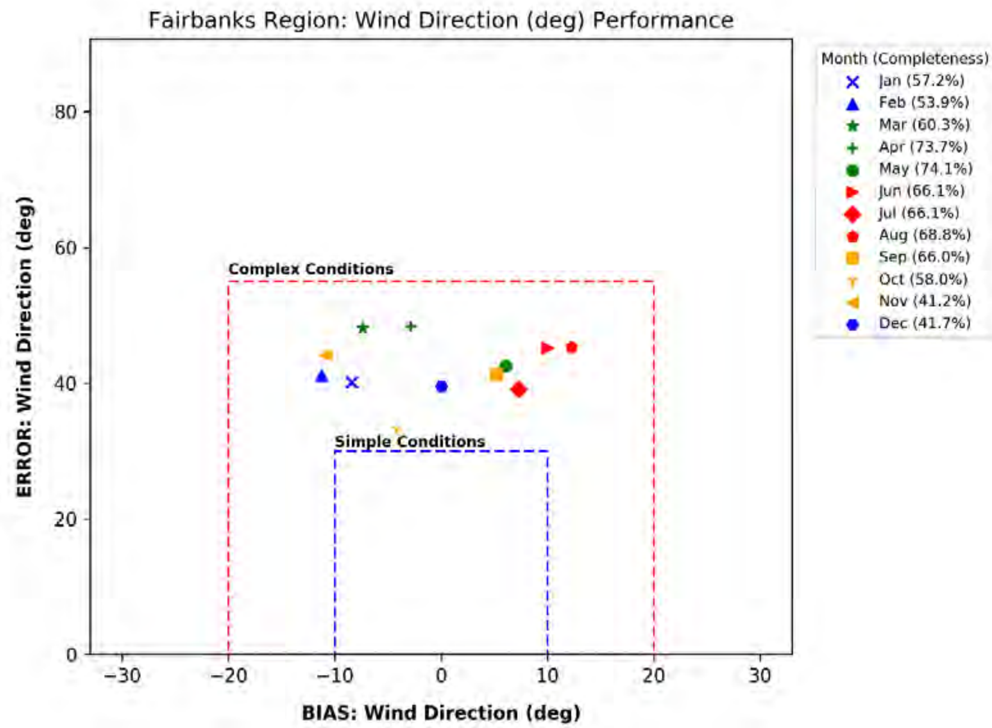

Figure 49. Soccer plot of monthly wind direction error and bias averaged over the Fairbanks subdomain for 2016.

4.3.4 Humidity

A plot of the PAFA station distributions of absolute humidity by hour of day per season is shown in **Figure 50**. WRF tended to overpredict humidity at PAFA in the winter and midday in spring and underpredict humidity in the early morning summer hours.

The Fairbanks subdomain humidity soccer plot is shown in **Figure 51.** Despite the bias shown at PAFA in the winter, the average bias and error across the subregion falls within the simple and complex criteria.

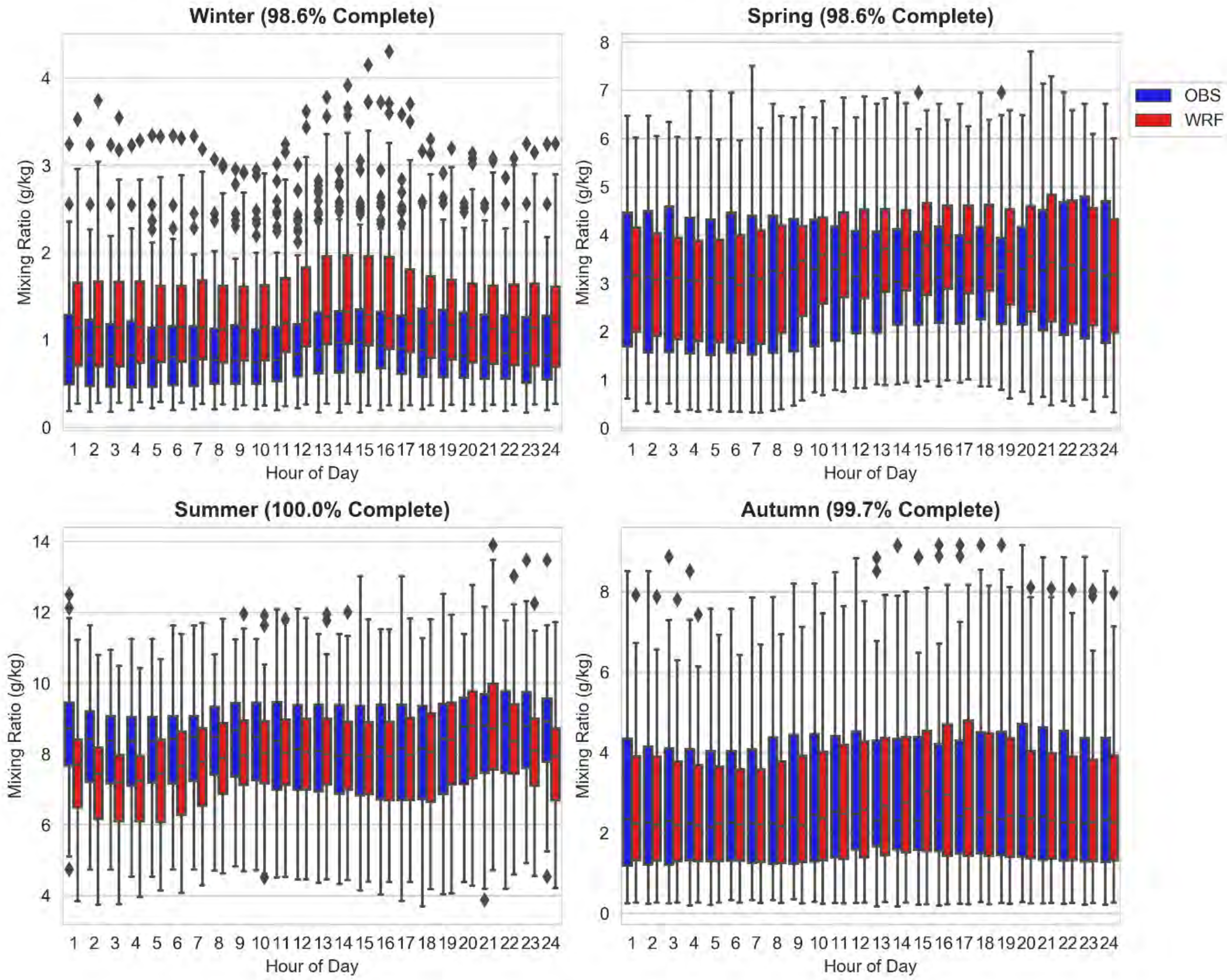

Figure 50. PAFA (Fairbanks) seasonal, hour-of-day absolute humidity distributions, ASOS (blue) vs. Alaska 9-km WRF (red).

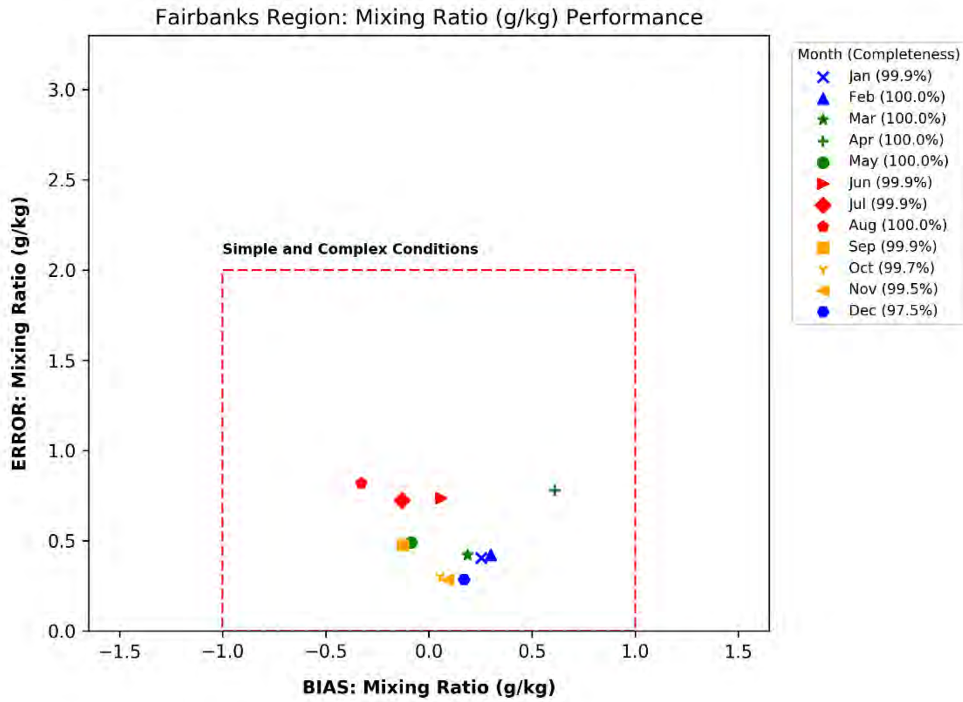

Figure 51. Soccer plot of monthly absolute humidity error and bias averaged over the Fairbanks subdomain for 2016.

4.4 North Slope region performance

The North Slope subregion performance was assessed using soccer plots to analyze average error and bias across all stations in the subdomain. Also, Deadhorse airport (PASC) was selected as the individual station of interest for the analysis. PASC was selected based on the proximity of the station to the Prudhoe Bay oil developments. Temperature, wind, and humidity performance for the subregion and at the individual station of interest is reviewed in this section.

4.4.1 Temperature

A plot of temperature distribution at PASC, examined by hour per season is shown in **Figure 52*Figure 36***. WRF tends to underpredict temperature all hours of the day in the winter at PASC. WRF temperature distributions compare well to PASC observations over the other seasons.

The soccer plot of bias and error across the North Slope subregion is shown in **Figure 53**. The results demonstrate poor WRF performance across the subregion in winter months. WRF predicts much cooler temperatures than observed, on average.

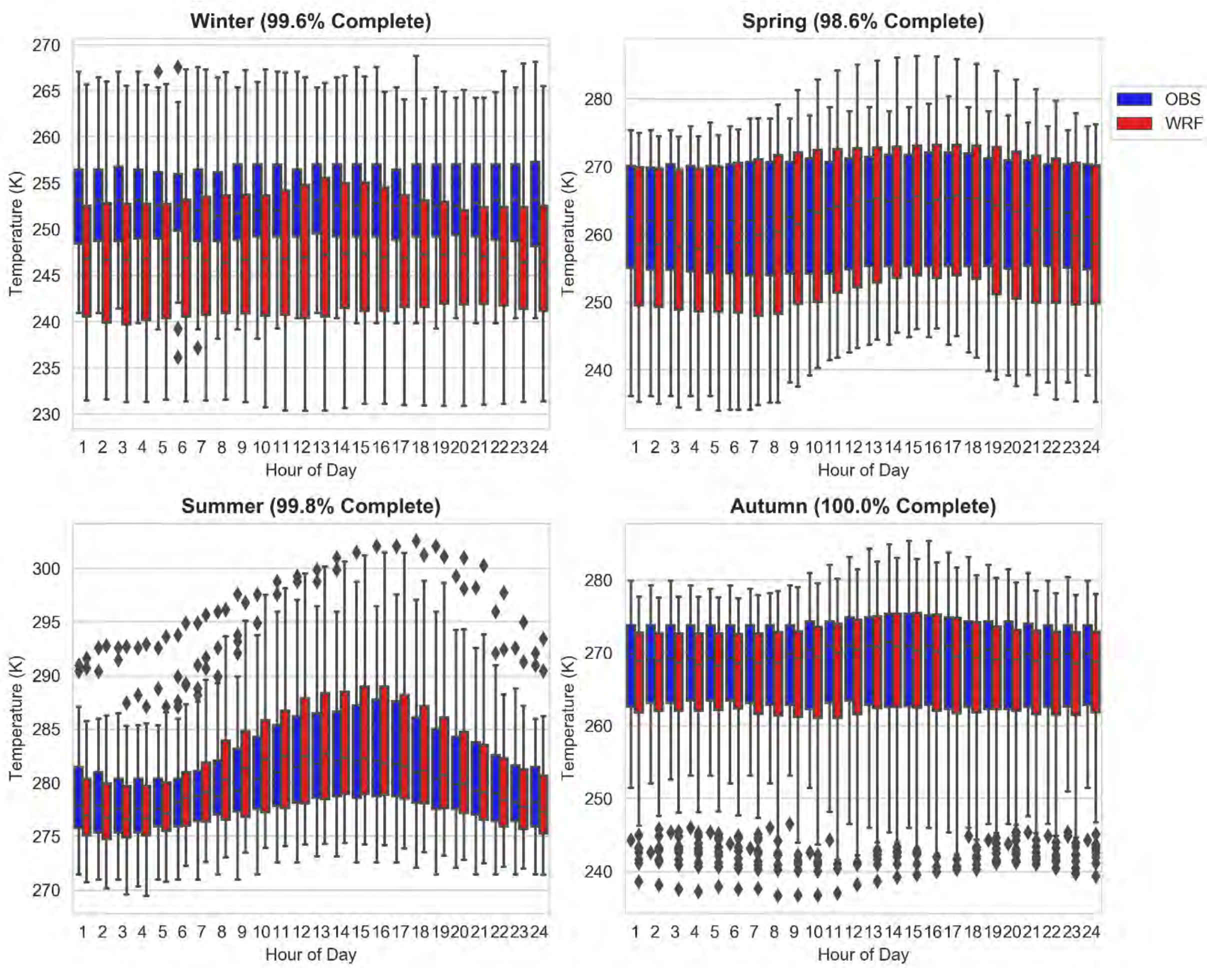

Figure 52. PASC (Deadhorse) seasonal, hour-of-day temperature distributions, ASOS (blue) vs. Alaska 9-km WRF (red).

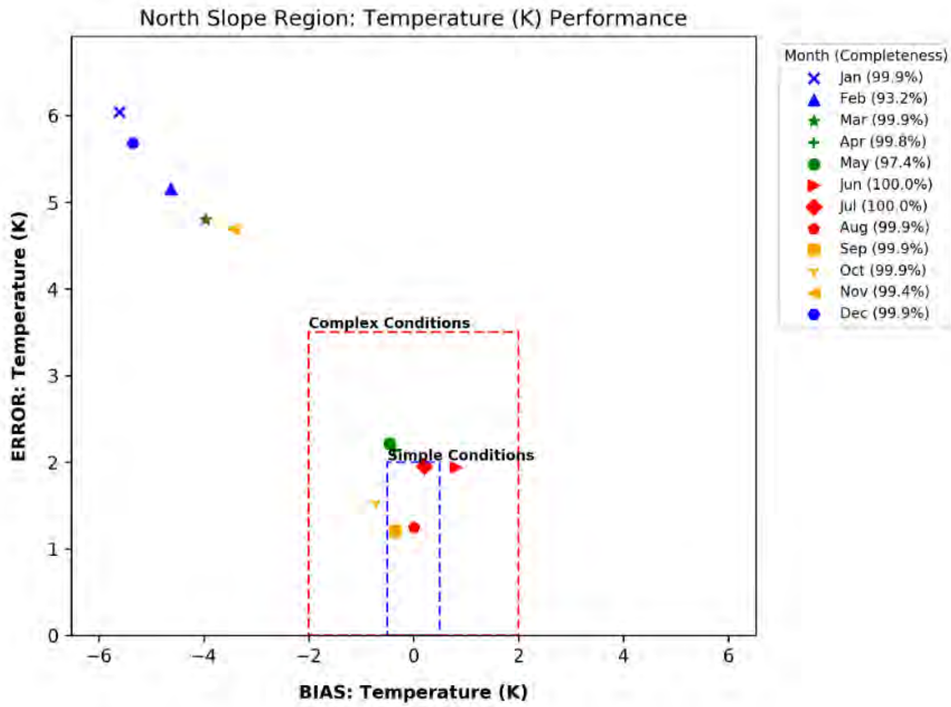

Figure 53. Soccer plot of monthly 2-m temperature error and bias averaged over the North Slope subdomain for 2016.

4.4.2 Wind speed

Wind roses developed from both the observed (PASC) and modeled datasets are plotted in **Figure 54**. Although the modes of predominant northeast and southwest winds appear to be well predicted by WRF, it is evident from the plot that WRF underpredicts wind speed. This is clear also in the plot of wind speed distribution at PASC, shown in **Figure 55**. Wind speed predictions are biased low all hours and seasons of the year at PASC.

The regional average wind speed error and bias soccer plot for the North Slope subregion is plotted in **Figure 56**. It is clear WRF is not optimized in this case to adequately predict surface winds along the North Slope, given the significant low wind speed bias. Bias and error exceed complex conditions criteria all seasons except summer.

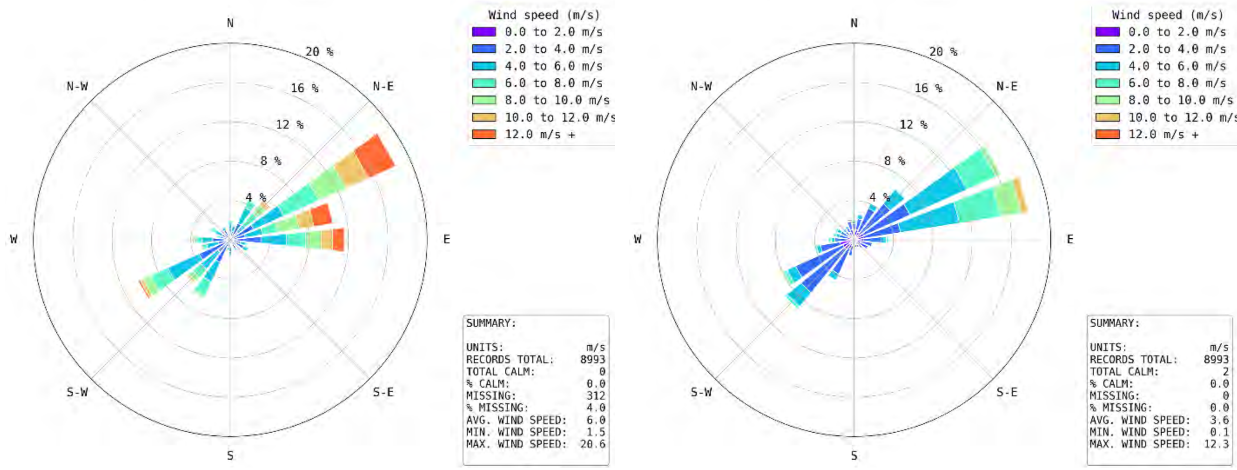

Figure 54. Wind rose comparison, PASC (Deadhorse), ASOS observed (left), Alaska 2016 WRF (right).

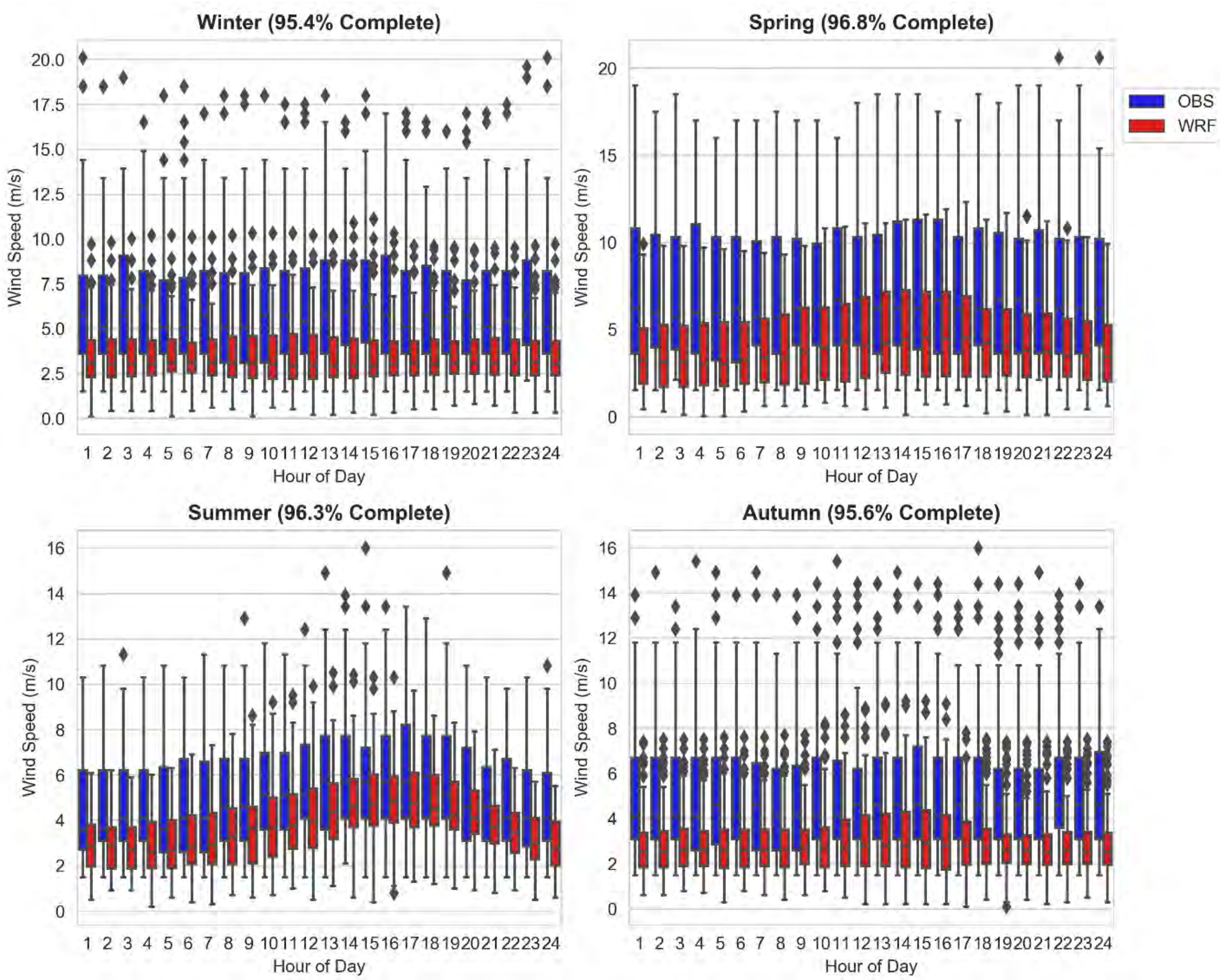

Figure 55. PASC (Deadhorse) seasonal, hour-of-day wind speed distributions, ASOS (blue) vs. Alaska 9-km WRF (red).

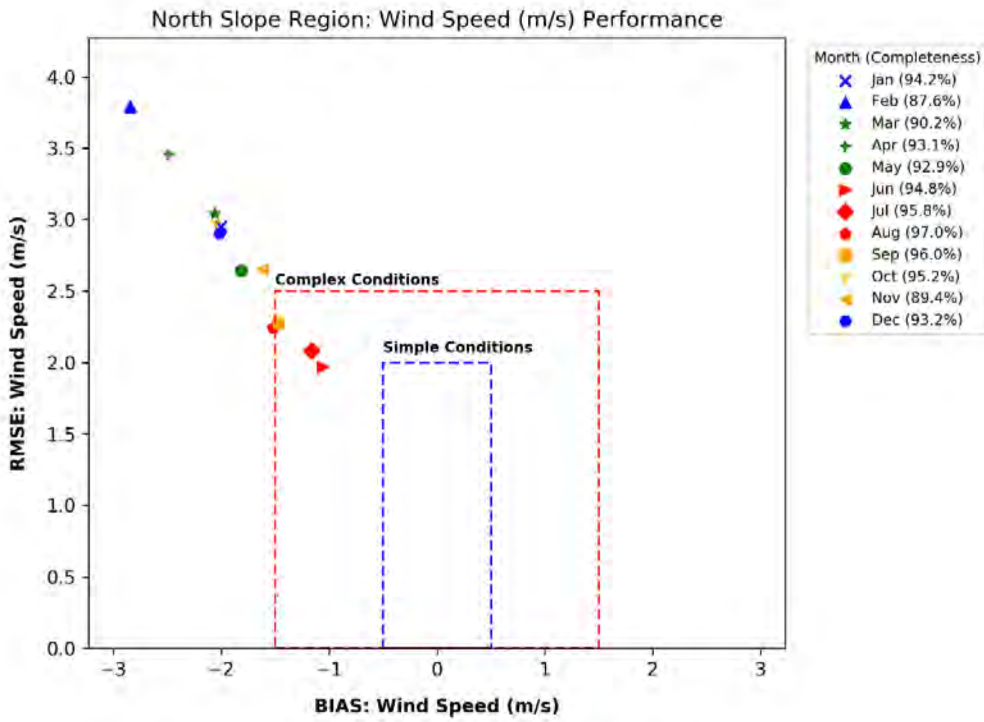

Figure 56. Soccer plot of monthly wind speed error and bias averaged over the North Slope subdomain for 2016.

4.4.3 Wind direction

The wind direction soccer-plot for the North Slope subdomain is shown in **Figure 57**. The plot demonstrates WRF predicts wind direction well across the subregion. Wind direction bias and error is within the simple conditions criteria all months of the year except November, which is within the complex conditions criteria.

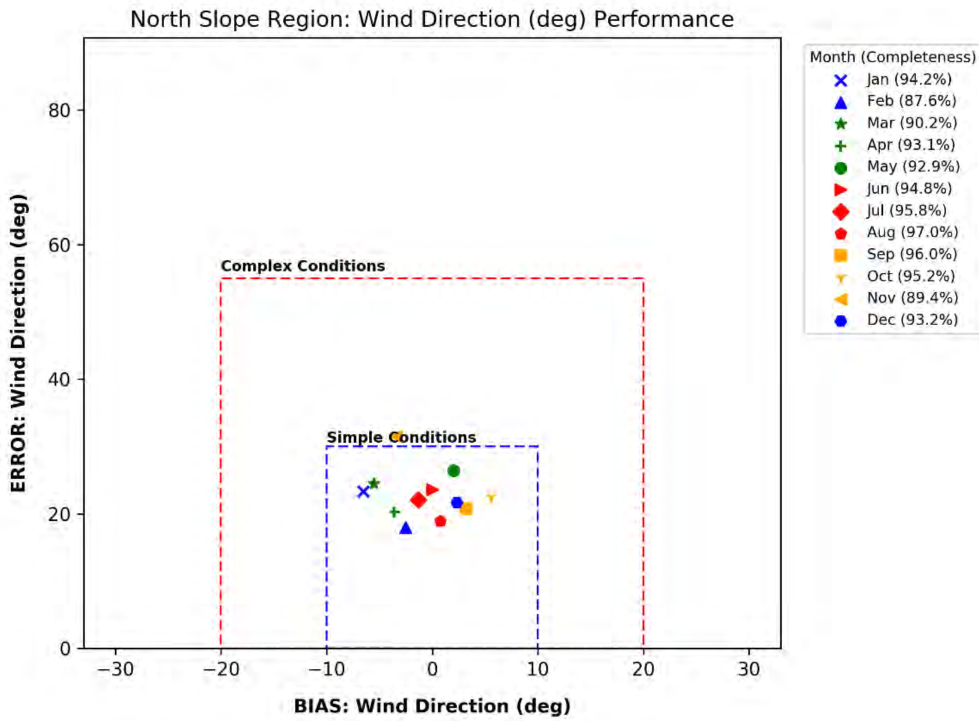

Figure 57. Soccer plot of monthly wind direction error and bias averaged over the North Slope subdomain for 2016.

4.4.4 Humidity

A plot of the PASC distributions of absolute humidity by hour of day per season is shown in **Figure 58*Figure 42***. WRF tends to underpredict humidity during the winter and summer seasons. The North Slope subdomain humidity soccer plot is shown in **Figure 59.** The average subdomain bias and error are within the criteria for all months.

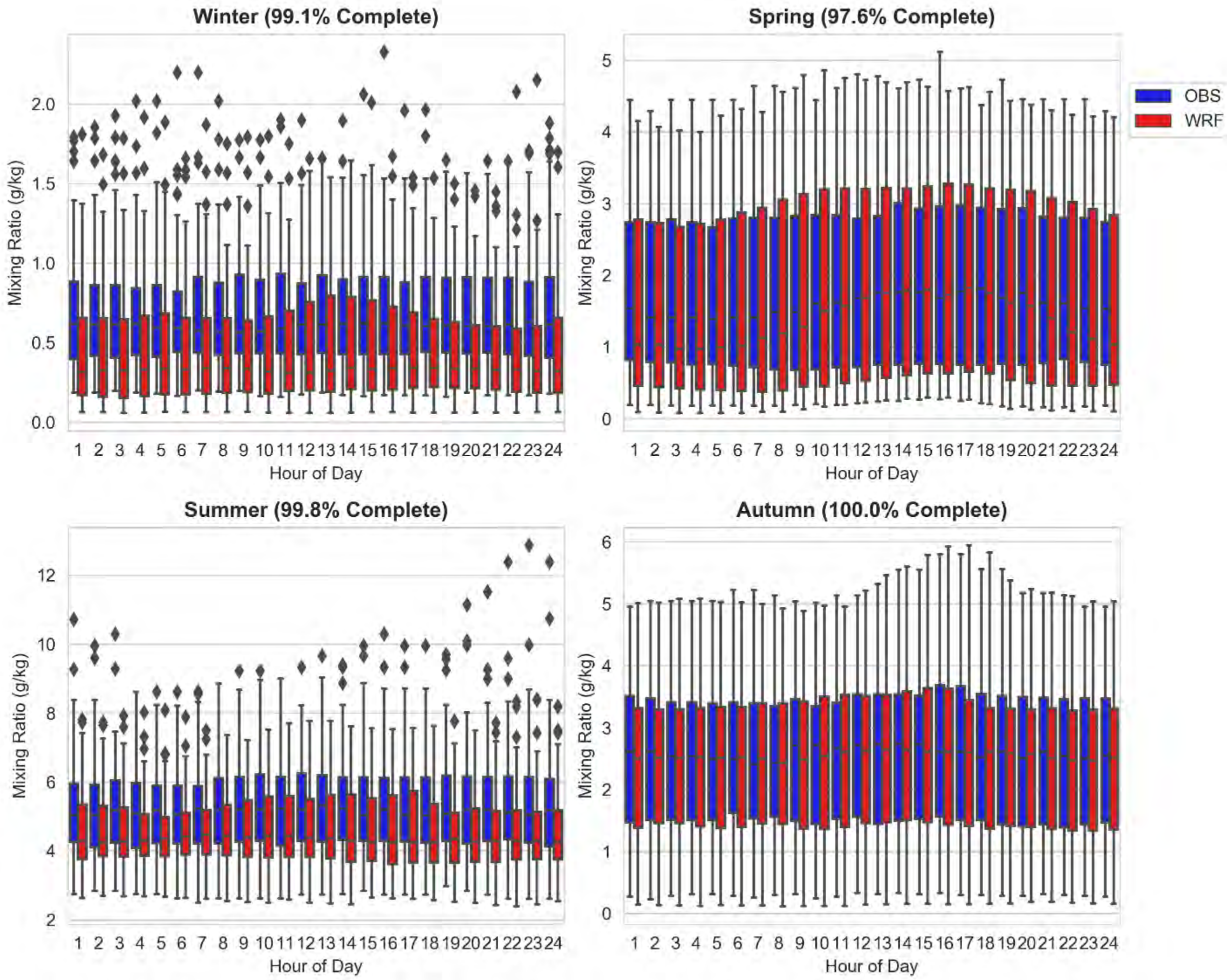

Figure 58. PASC (Deadhorse) seasonal, hour-of-day absolute humidity distributions, ASOS (blue) vs. Alaska 9-km WRF (red).

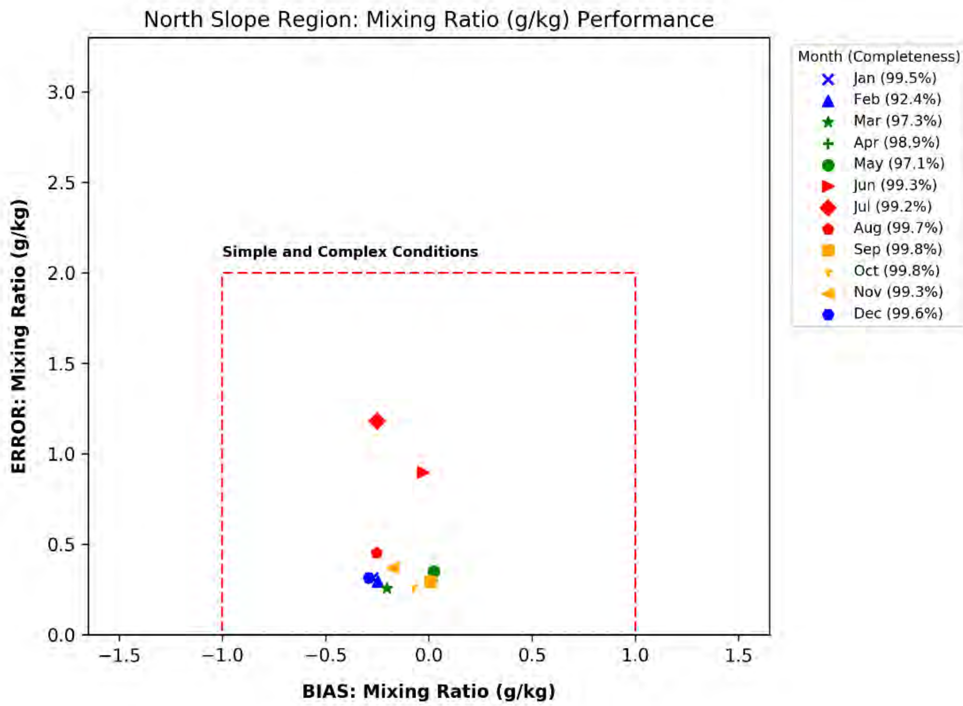

Figure 59. Soccer plot of monthly absolute humidity error and bias averaged over the North Slope subdomain for 2016.

4.5 Juneau region performance

The Juneau subregion performance was assessed using soccer plots to analyze average error and bias across all stations in the subdomain. Also, the Juneau airport (PAJN) was selected as the individual station of interest for the analysis, due to its location near the center of the subdomain and its relative distance from significant high terrain features compared to other stations in the domain. Temperature, wind, and humidity performance is examined for the subregion and at the individual station of interest in this section.

4.5.1 Temperature

A plot of temperature distribution at PAJN, examined by hour per season, is shown in **Figure 60**. Generally, the temperature daily trends predicted by WRF match the observed value trends, except WRF is consistently cooler than the observations on average.

The soccer plot of bias and error across the Juneau subregion is shown in **Figure 61**. The results fall within the complex criteria all months of the year. Temperature bias and error fall within the simple criteria during the autumn months. The year-round cold biases evident in the PAJN comparisons are evident in the performance statistics for the entire subregion.

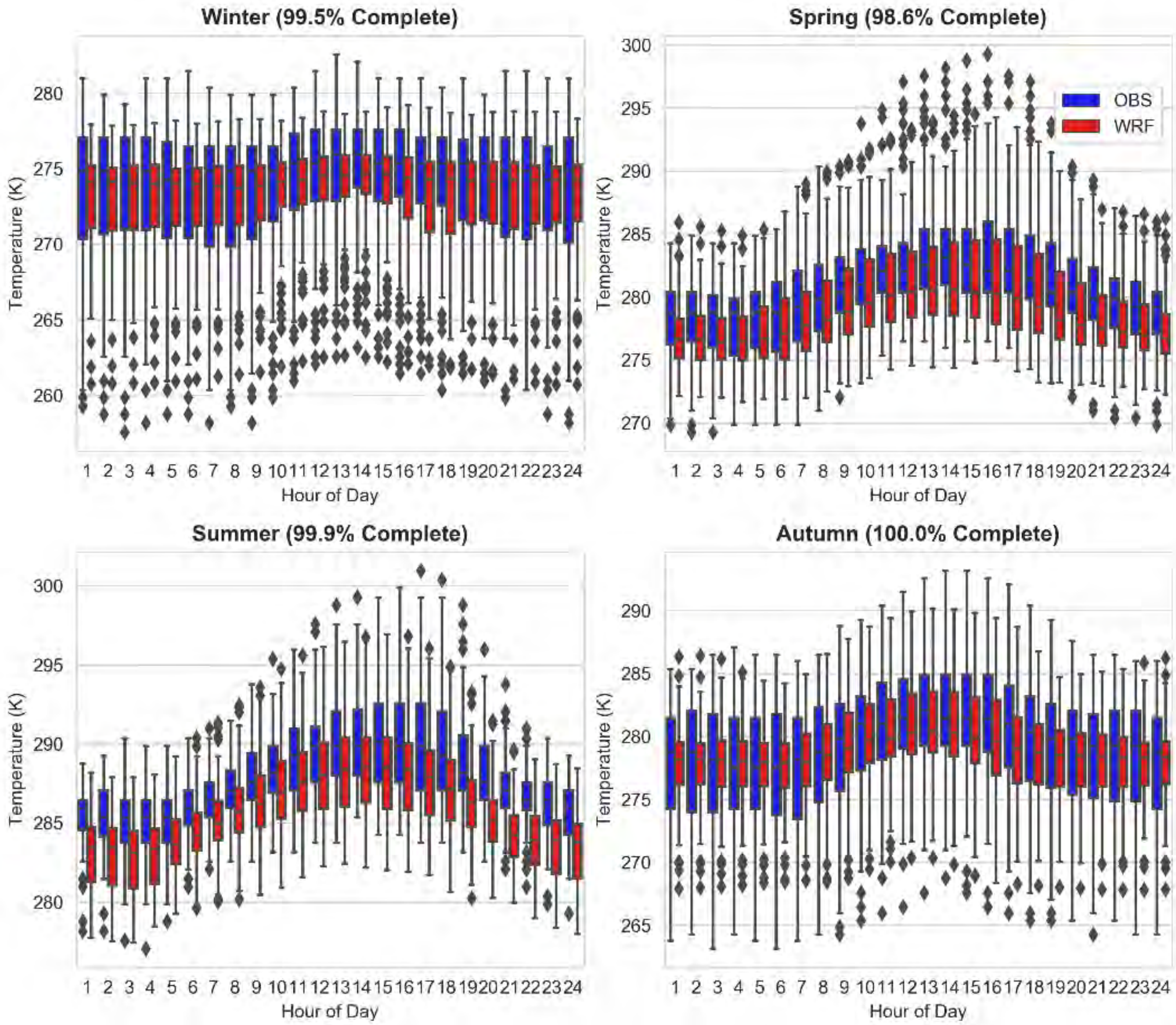

Figure 60. PAJN (Juneau airport) seasonal, hour-of-day temperature distributions, ASOS (blue) vs. Alaska 9-km WRF (red).

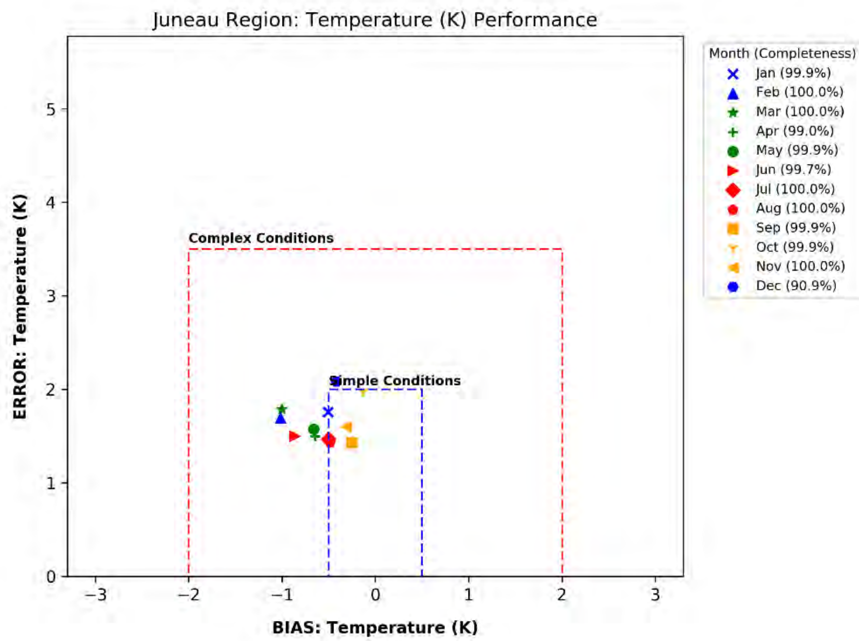

Figure 61. Soccer plot of monthly 2-m temperature error and bias averaged over the Juneau subdomain for 2016.

4.5.2 Wind speed

A plot of wind roses developed from both the observed (PAJN) and modeled datasets is included in **Figure 62**. WRF appears to predict the magnitude and easterly modes of wind well, given some error in wind direction is expected at 9 km resolution in a region of complex terrain. The distribution of wind speed per season by hour of day is plotted in **Figure 63**. Wind speed distributions are predicted well in spring and autumn months. WRF tends to overpredict wind speed in winter and autumn early morning periods and highly underpredicts windspeed continuously through the summer months.

The regional average wind speed error and bias soccer plot for the Juneau subregion is plotted in **Figure 64**. Regional wind speed error exceeds complex criteria over the winter months.

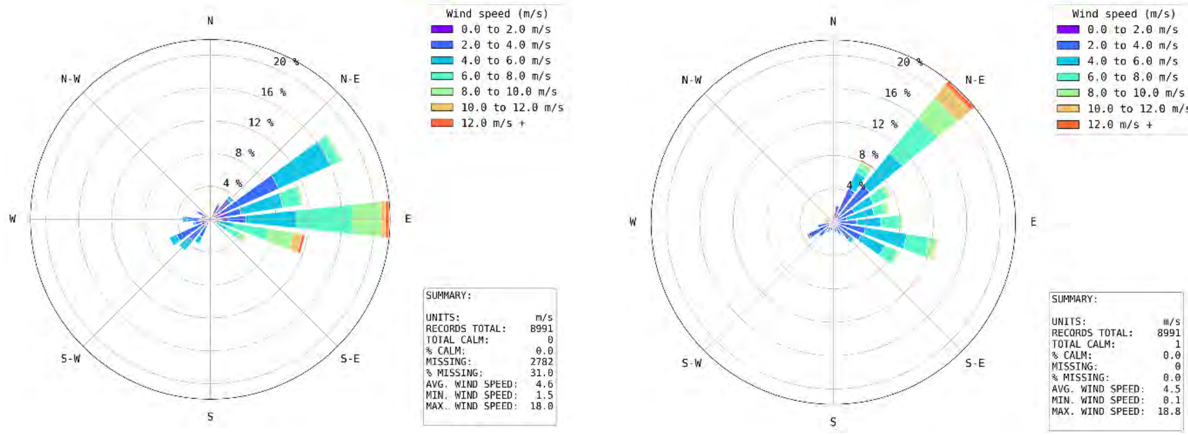

Figure 62. Wind rose comparison, PAJN (Juneau), ASOS observed (left), Alaska 2016 WRF (right).

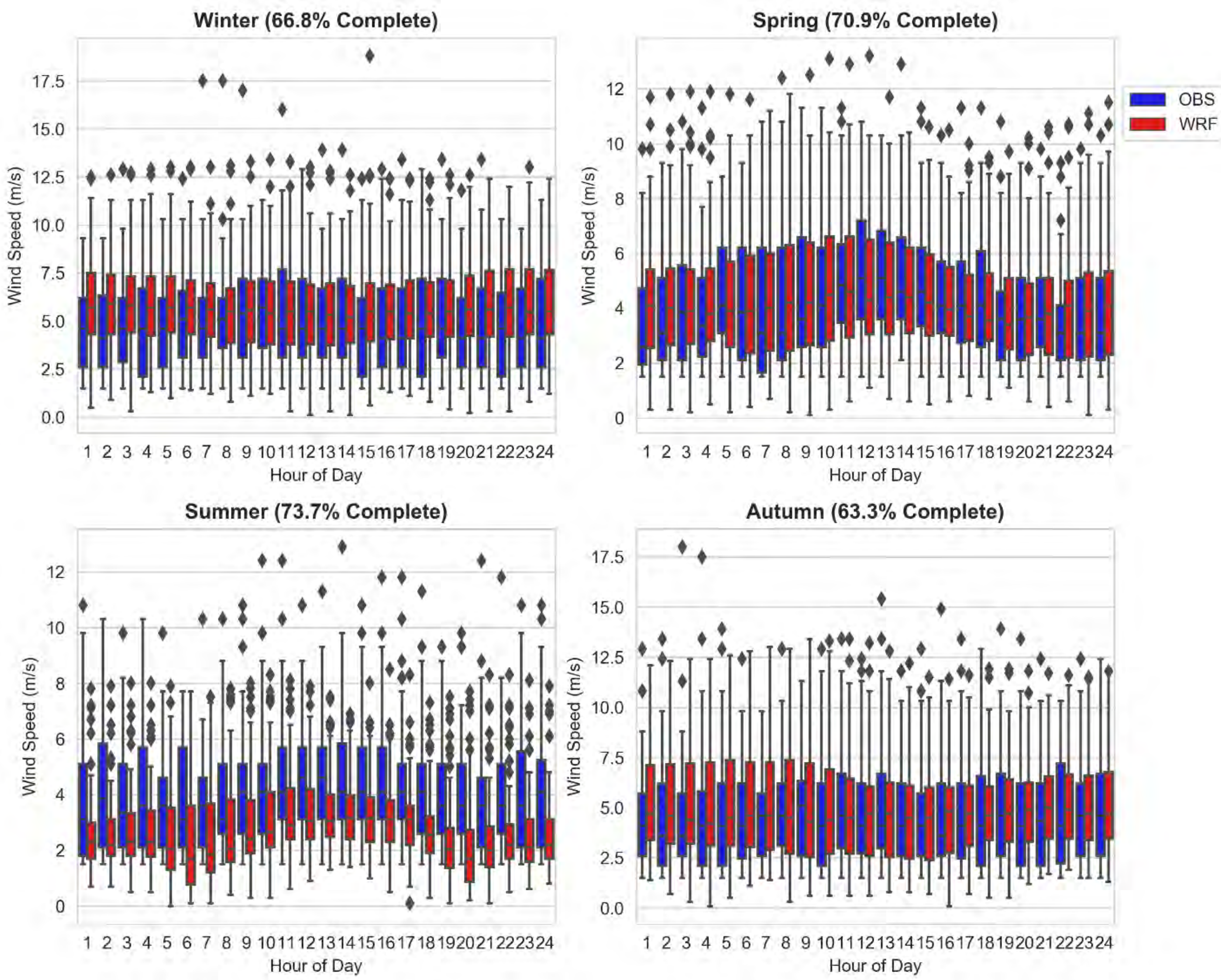

Figure 63. PAJN (Juneau) seasonal, hour-of-day wind speed distributions, ASOS (blue) vs. Alaska 9-km WRF (red).

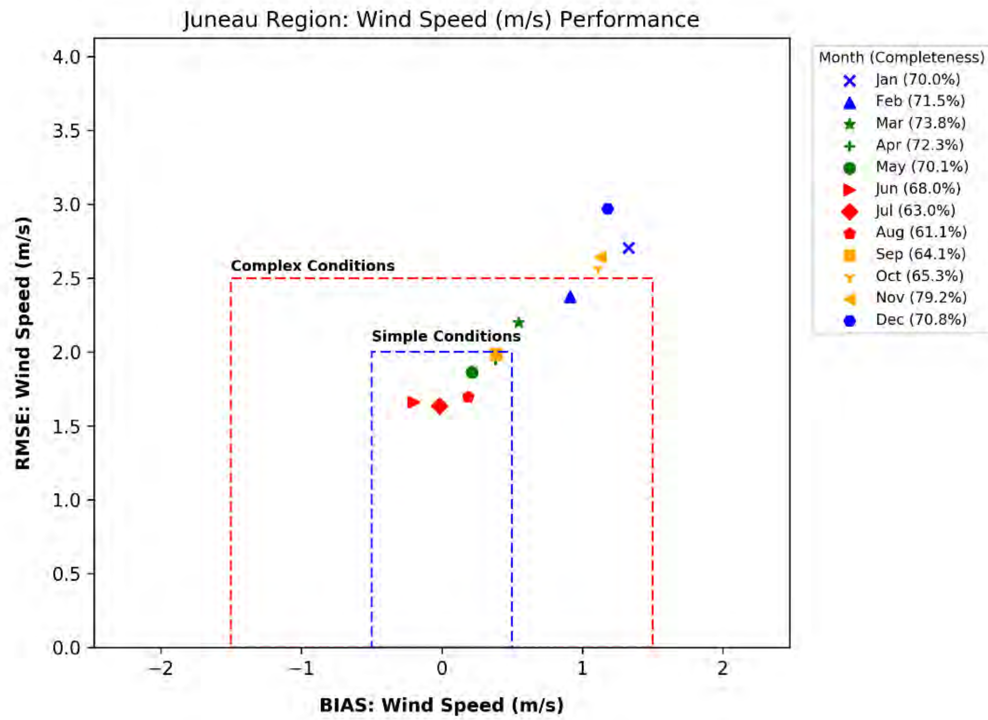

Figure 64. Soccer plot of monthly wind speed error and bias averaged over the Juneau subdomain for 2016.

4.5.3 Wind direction

The Juneau subdomain wind direction monthly bias and error is plotted in **Figure 65**. Performance is within the bias complex criteria but exceeds the error benchmark in summer months.

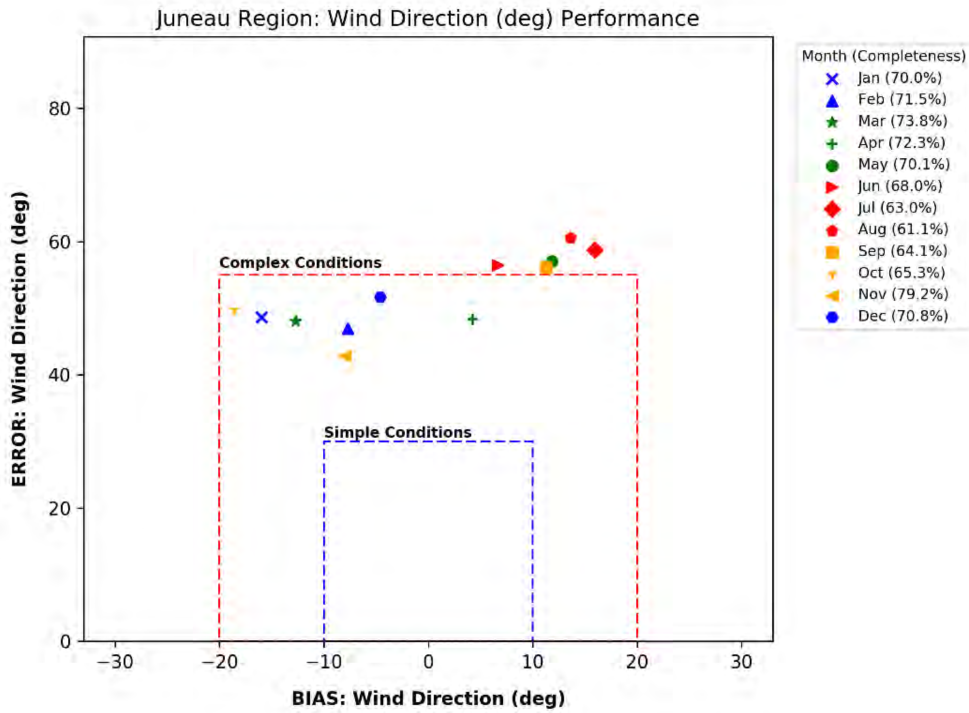

Figure 65. Soccer plot of monthly wind direction error and bias averaged over the Juneau subdomain for 2016.

4.5.4 Humidity

A plot of the PAJN station distributions of absolute humidity by hour of day per season is shown in **Figure 66**. Overall, WRF tends to be biased low, most evidently in summer and spring morning hours.

The Juneau subdomain humidity soccer plot is shown in **Figure 67.** The average subdomain bias and error are within the benchmark criteria for all months.

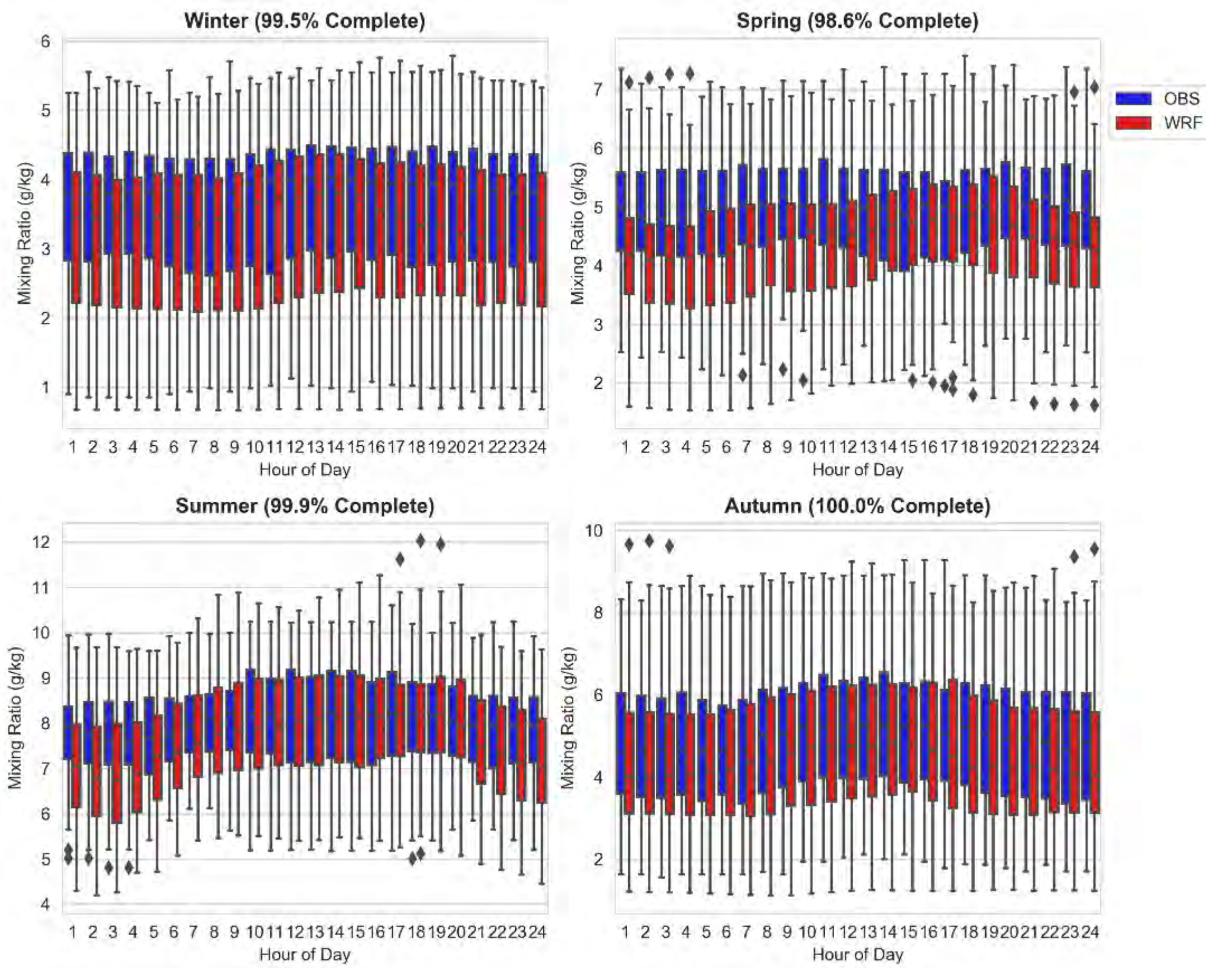

Figure 66. PAJN (Juneau) seasonal, hour-of-day absolute humidity distributions, ASOS (blue) vs. Alaska 9-km WRF (red).

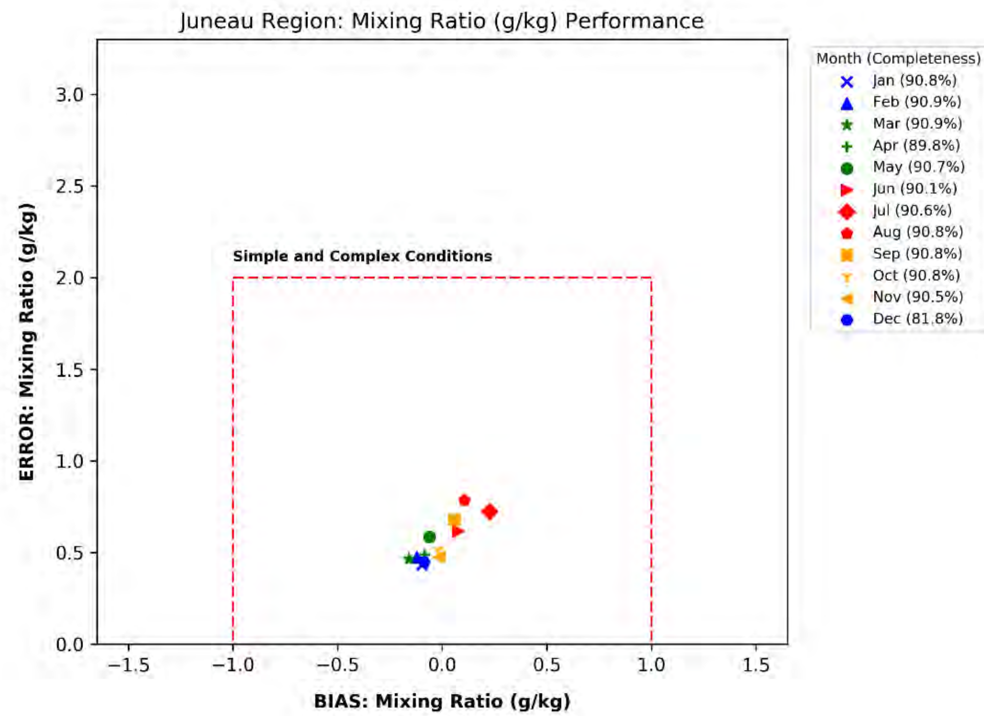

Figure 67. Soccer plot of monthly absolute humidity error and bias averaged over the Juneau subdomain for 2016.

4.6 Alaska Peninsula region performance

The Alaska Peninsula subregion performance was assessed using soccer plots to analyze average error and bias across all stations in the subdomain. Also, the Unalaska airport dataset (PADU) was selected as the individual station of interest for the analysis, due to its location near industrial developments at Unalaska and Dutch Harbor.

4.6.1 Temperature

A plot of temperature distribution at PADU, examined by hour per season is shown in **Figure 68**. WRF results are consistently cooler than the observations all of the year. The cool bias is evident regionally in the soccer plot of bias and error across the Alaska Peninsula subregion, shown in **Figure 69**. However, the bias and error are within the complex conditions criteria.

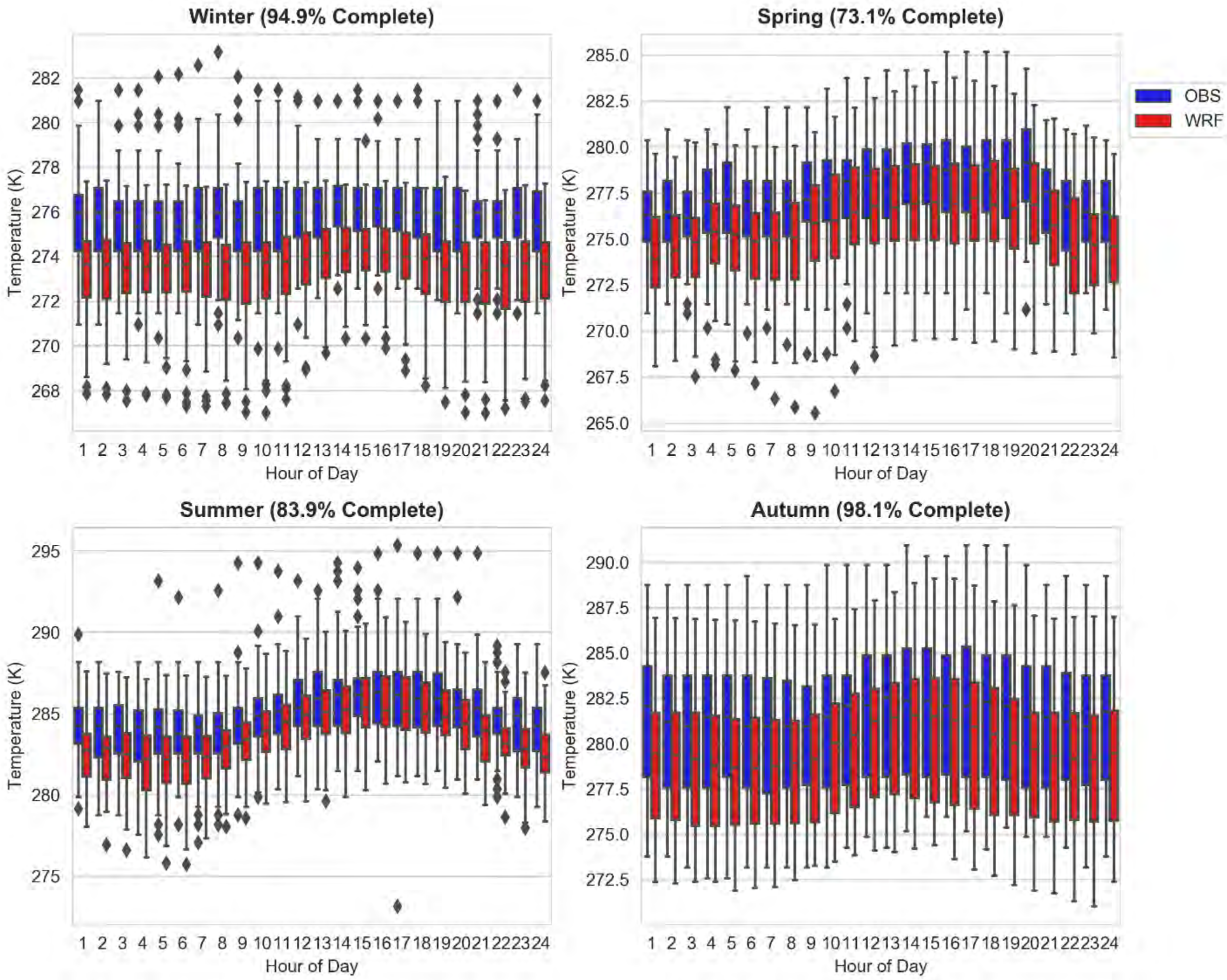

Figure 68. PADU (Unalaska) seasonal, hour-of-day temperature distributions, ASOS (blue) vs. Alaska 9-km WRF (red).

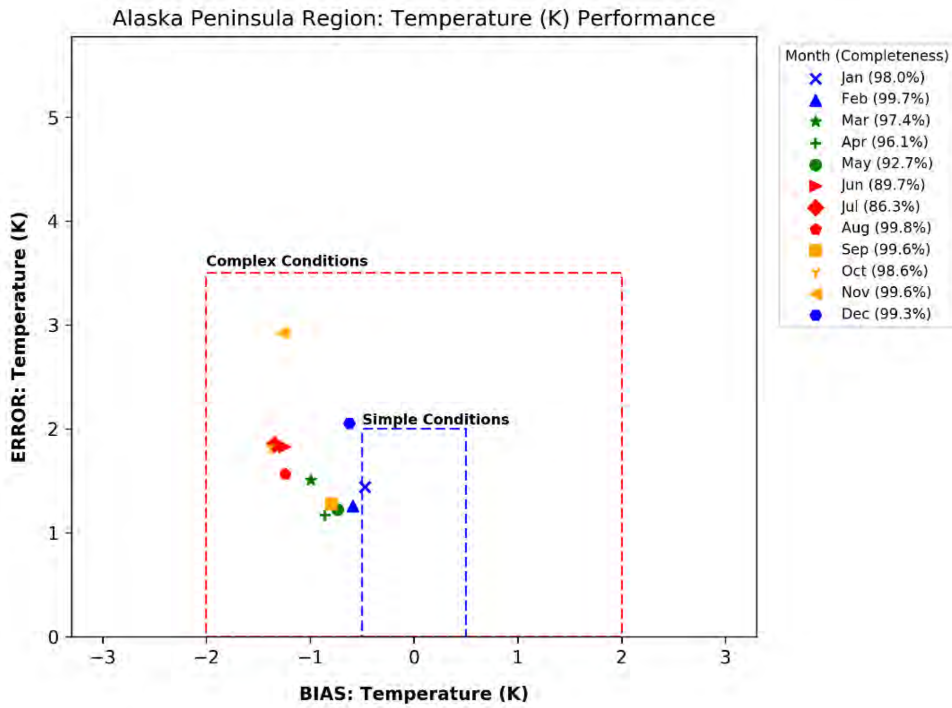

Figure 69. Soccer plot of monthly 2-m temperature error and bias averaged over the Alaska Peninsula subdomain for 2016.

4.6.2 Wind speed

Wind roses developed from both the observed (PADU) and modeled datasets are shown in **Figure 70**. WRF appears to produce the general wider distribution of wind speed and direction well, except WRF does not produce the mode of southeast wind that is evident in the observation dataset. The mode could be a result of local wind channeling by terrain features that are not resolved in the 9 km WRF domain.

The distribution of wind speeds per season by hour of day at PADU is plotted in **Figure 71**. The plot demonstrates predicted wind speed distributions are biased slightly high most of the year. The regional average wind speed error and bias soccer plot for the Alaska Peninsula subregion is plotted in **Figure 72**. The magnitude of regional wind speed bias is low, falling within the simple conditions criteria all months. However, winter wind speed error exceeds complex criteria a few months of the year.

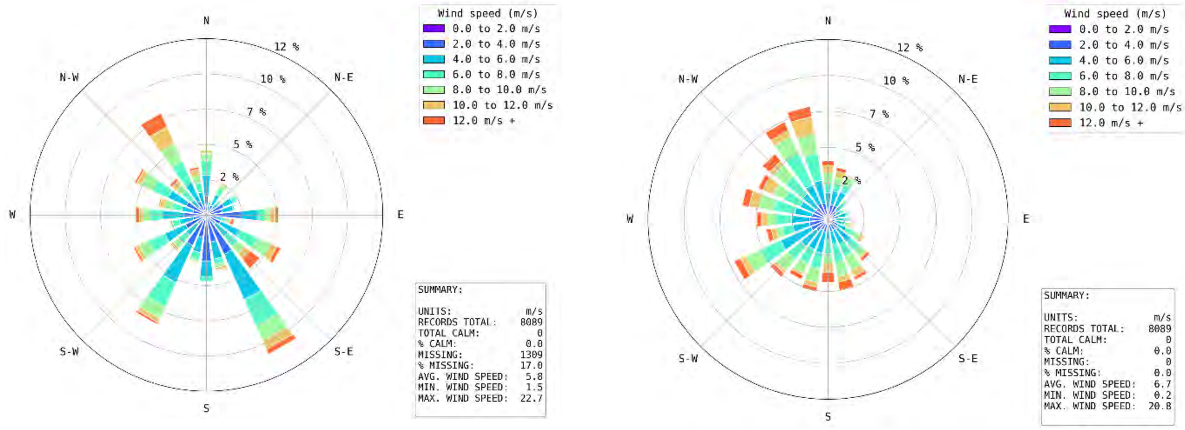

Figure 70. Wind rose comparison, PADU (Unalaska), ASOS observed (left), Alaska 2016 WRF (right).

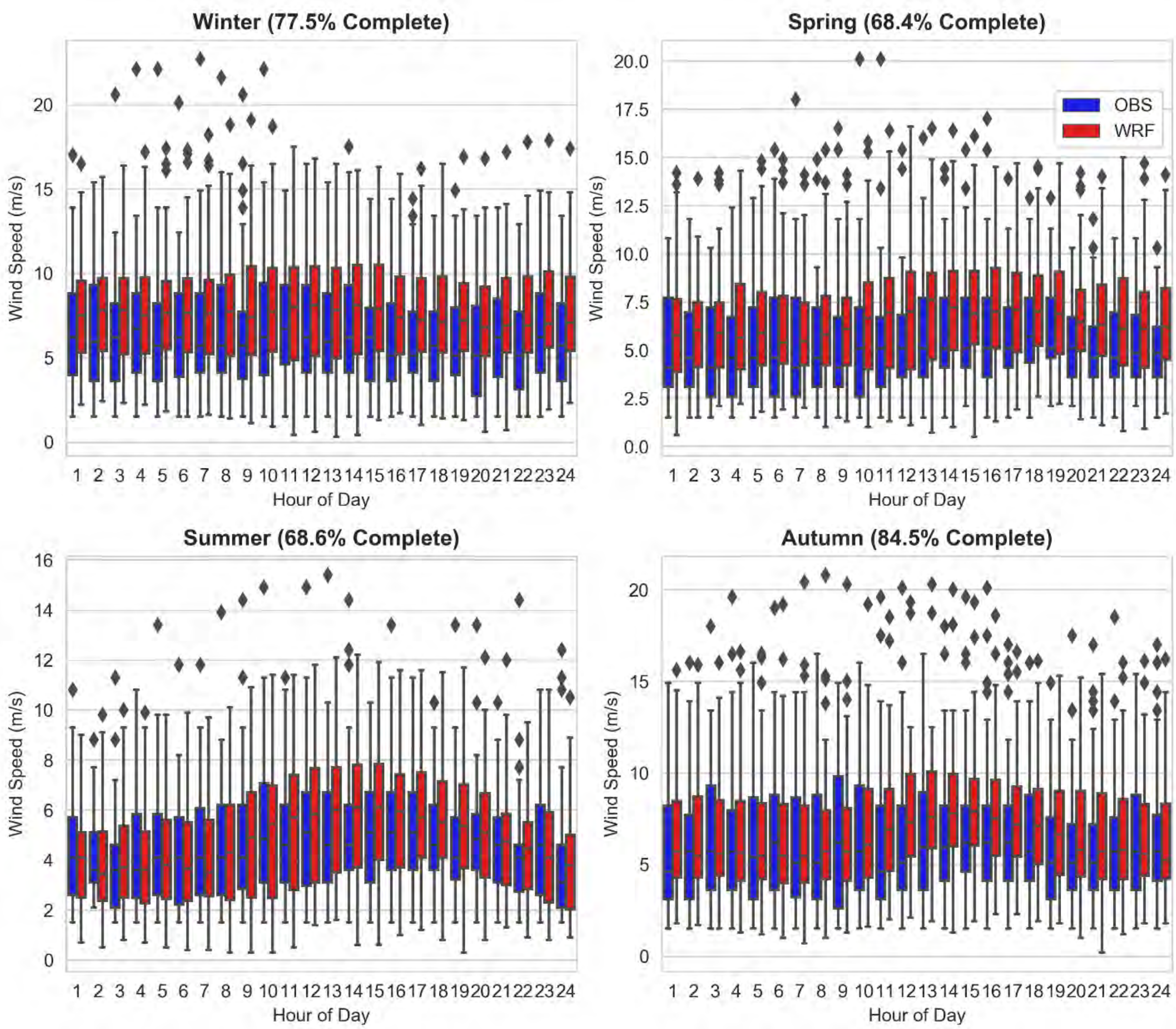

Figure 71. PADU (Unalaska) seasonal, hour-of-day wind speed distributions, ASOS (blue) vs. Alaska 9-km WRF (red).

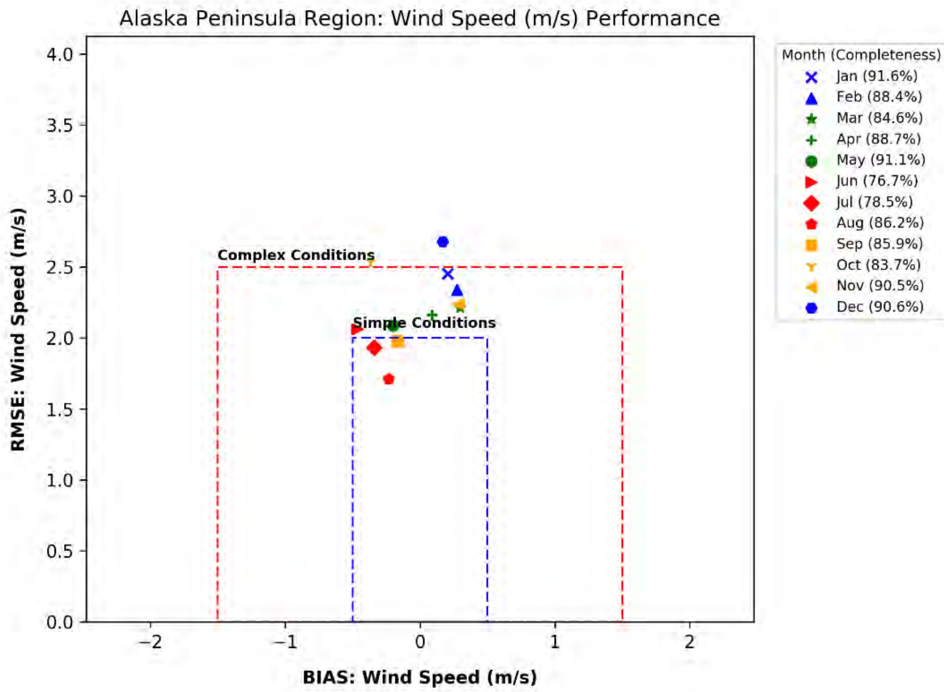

Figure 72. Soccer plot of monthly wind speed error and bias averaged over the Alaska Peninsula subdomain for 2016.

4.6.3 Wind direction

The Alaska Peninsula subdomain wind direction monthly bias and error is plotted in **Figure 73**. Wind direction bias and error fall within the complex criteria all months of the year.

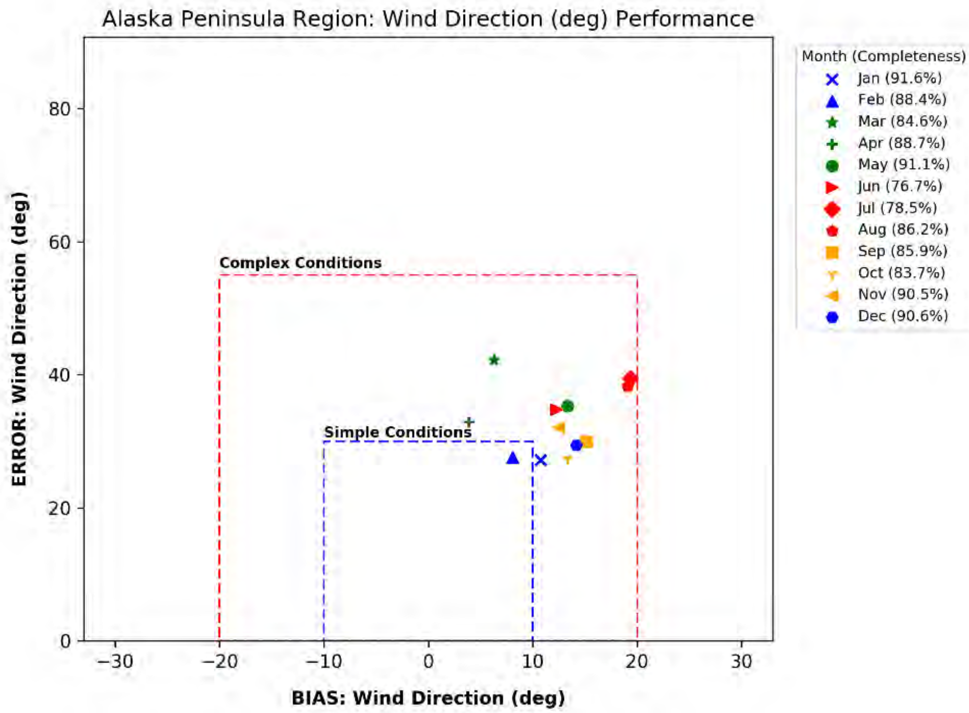

Figure 73. Soccer plot of monthly wind direction error and bias averaged over the Alaska Peninsula subdomain for 2016.

4.6.4 Humidity

A plot of the PADU distributions of absolute humidity by hour of day per season is shown in **Figure 74**. The Alaska Peninsula subdomain humidity soccer plot is shown in **Figure 75.** The magnitude of bias and error are low, falling within the benchmark criteria.

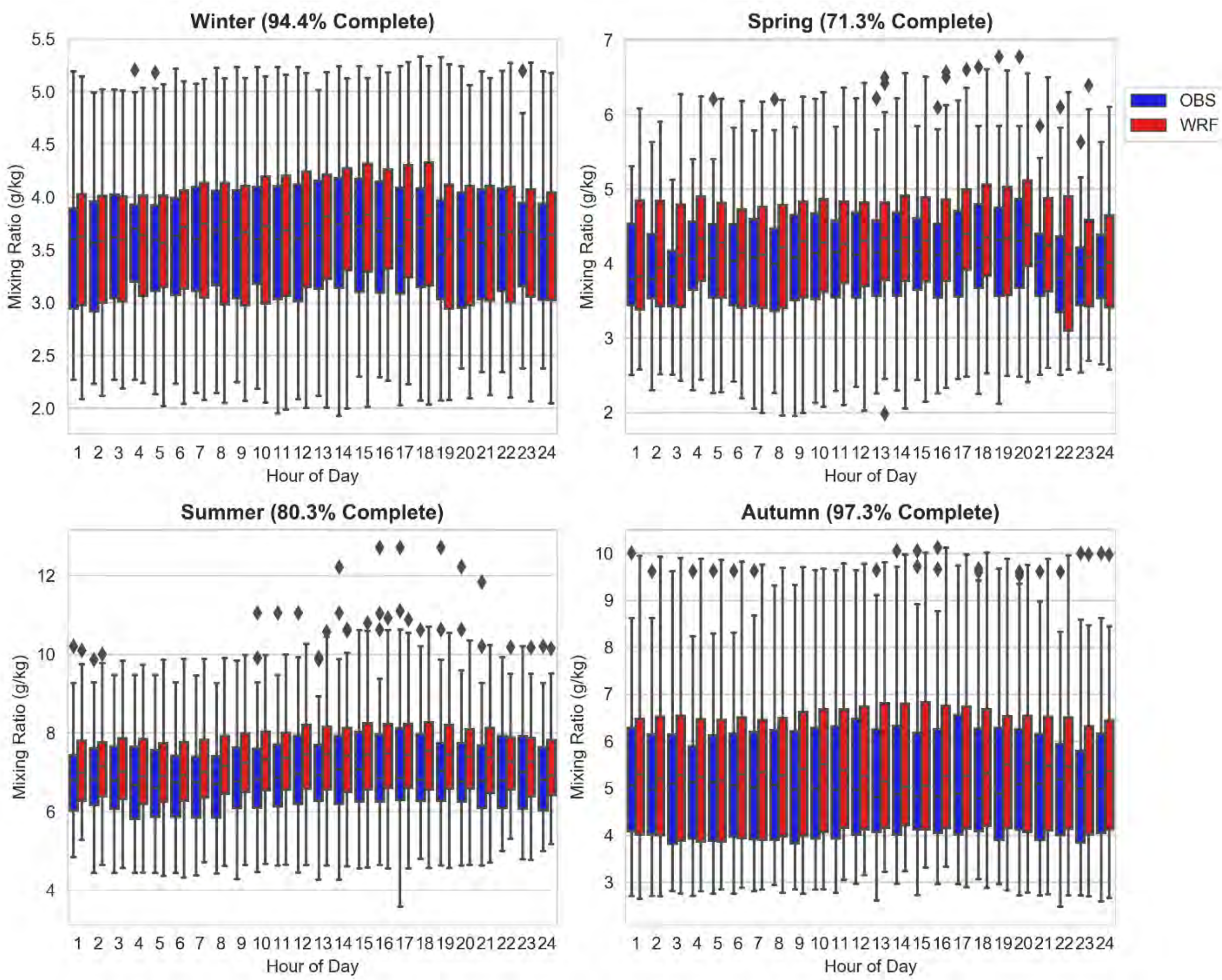

Figure 74. PADU (Unalaska) seasonal, hour-of-day absolute humidity distributions, ASOS (blue) vs. Alaska 9-km WRF (red).

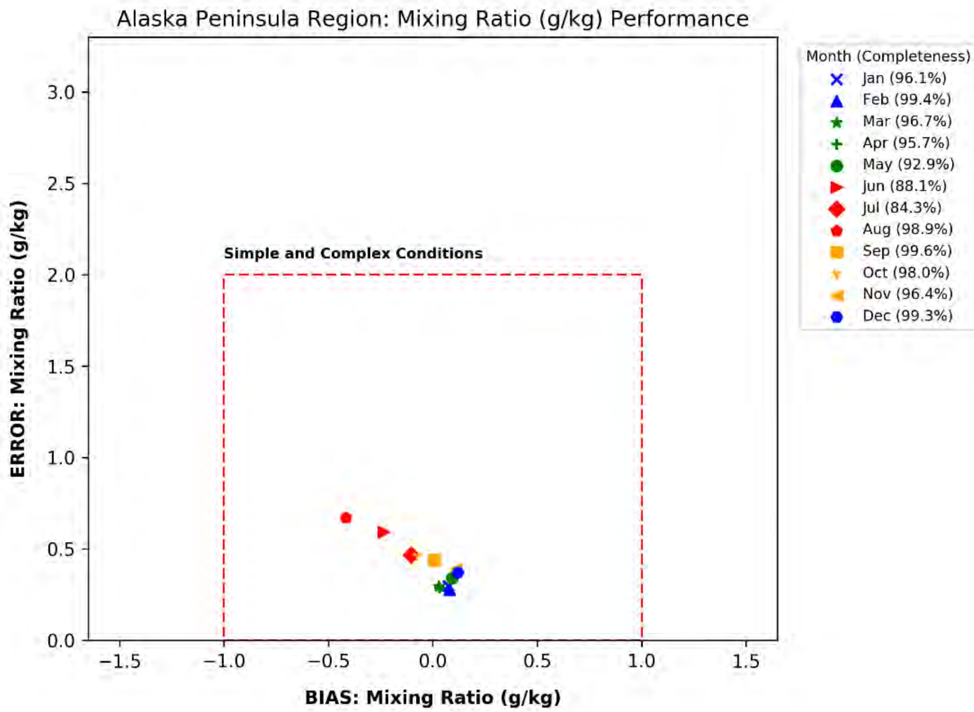

Figure 75. Soccer plot of monthly absolute humidity error and bias averaged over the Alaska Peninsula subdomain for 2016.

4.7 Upper-air analysis

A subset of upper-air station datasets was selected to illustrate general model performance at different locations across the 9 km domain. More specifically, five stations were selected to evaluate a variety of locations in Alaska, one in each of the subregions analyzed in the previous sections. The upper air stations were selected because they were representative of the regions in which they were located, with preference given to upper air stations located near the surface stations that were analyzed previously. Performance plots of all the upper-air station datasets are available in Appendix A.

The CYEV (Inuvik, Canada) upper air station was selected to analyze performance in the northeast region of the WRF domain. The 0z and 12z sounding distributions of temperature, wind speed, wind direction, and relative humidity error per season are plotted in **Figure 76**, **Figure 77**, **Figure 78**, and **Figure 79**, respectively. Temperature near the surface tends to be biased slightly cool in the morning (12z soundings) and biased warm in the afternoons (0z soundings) in the spring and summer. Relative humidity is shown to be biased a bit dry in the winter and summer and a bit wet in the spring and autumn.

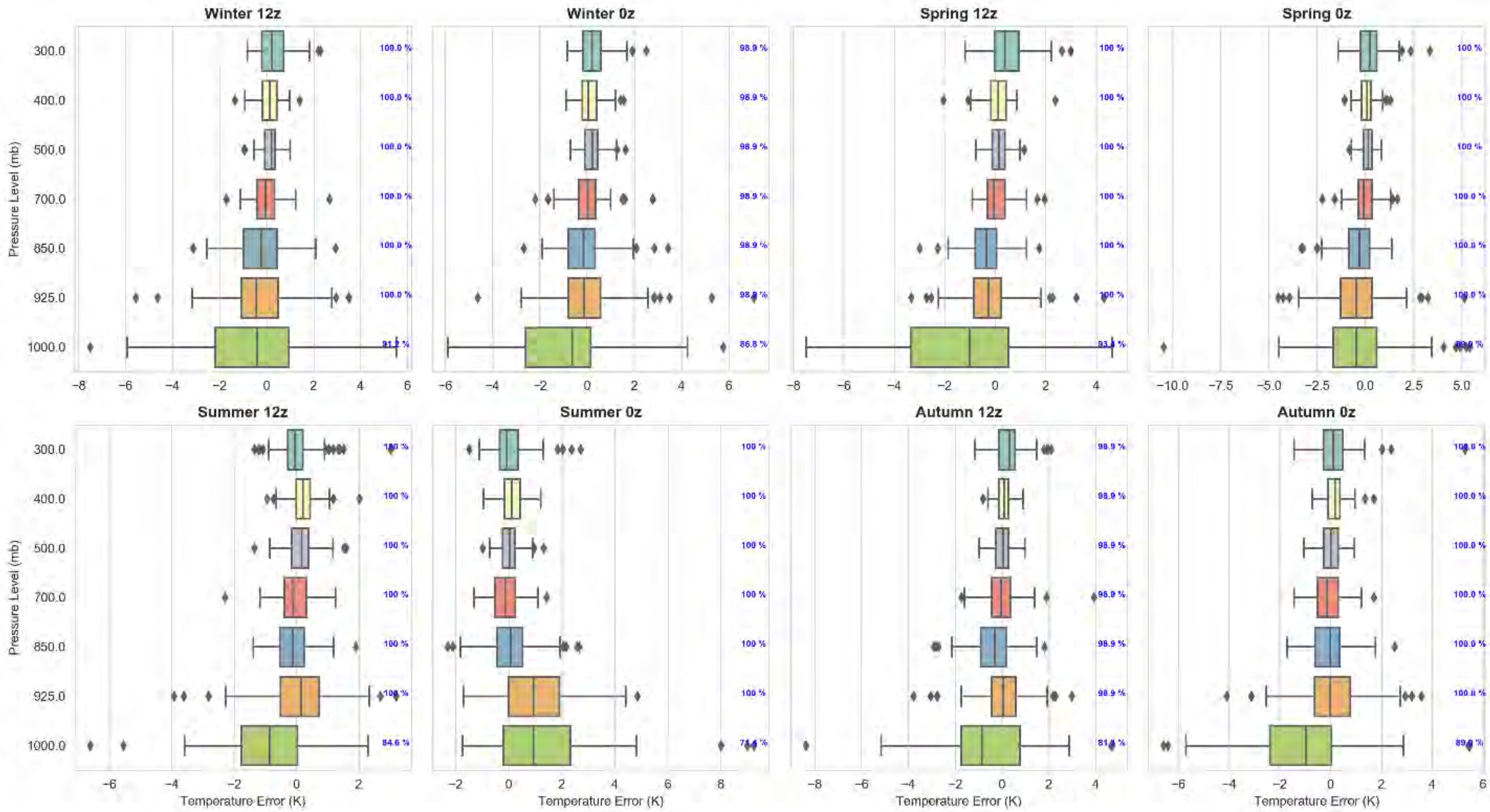

Figure 76. CYEV (Inuvik, Canada) upper-air distribution of temperature error by pressure-level and season (dataset seasonal completeness indicated in blue).

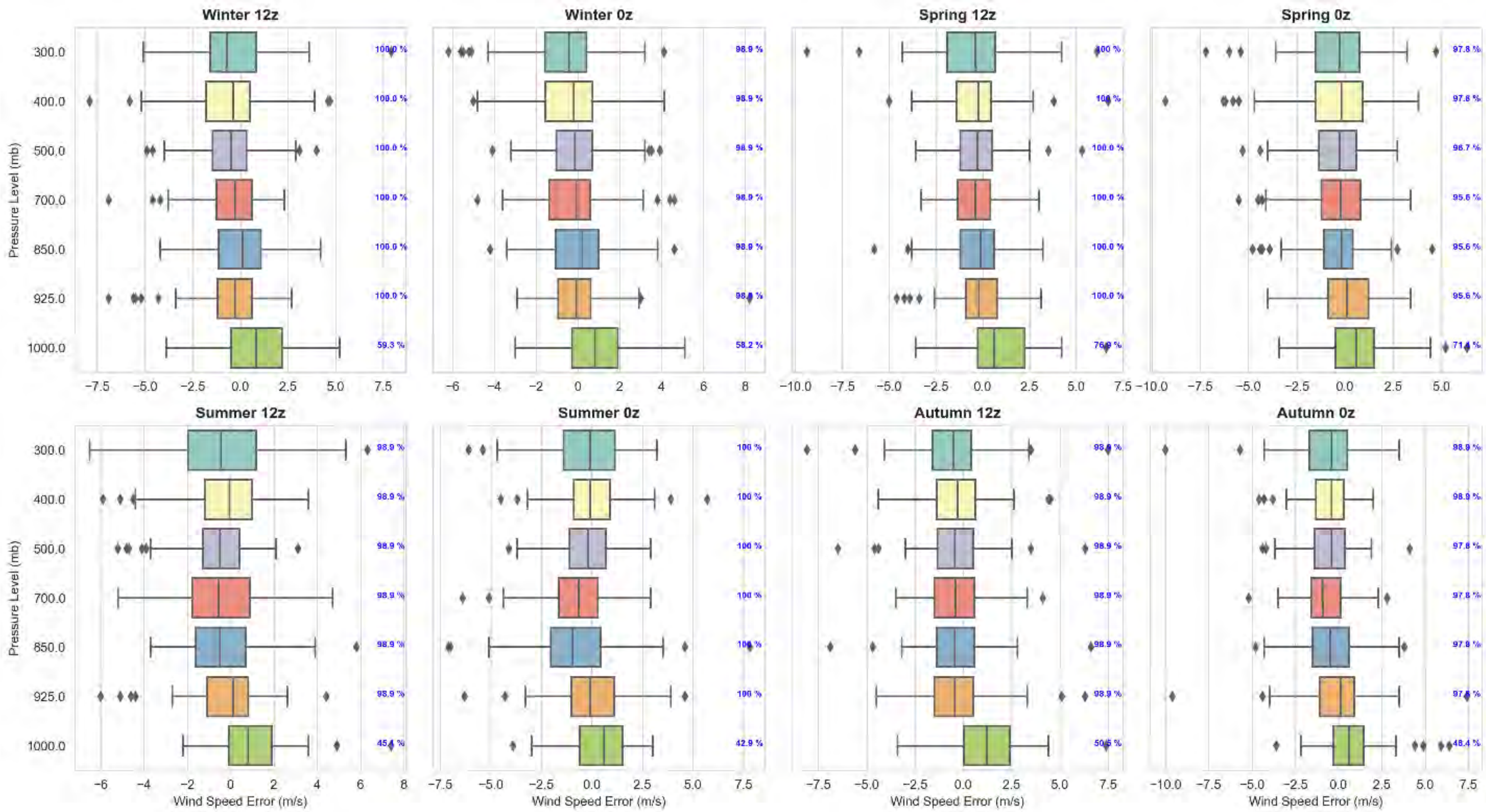

Figure 77. CYEV (Inuvik, Canada) upper-air distribution of wind speed error by pressure-level and season (dataset seasonal completeness indicated in blue).

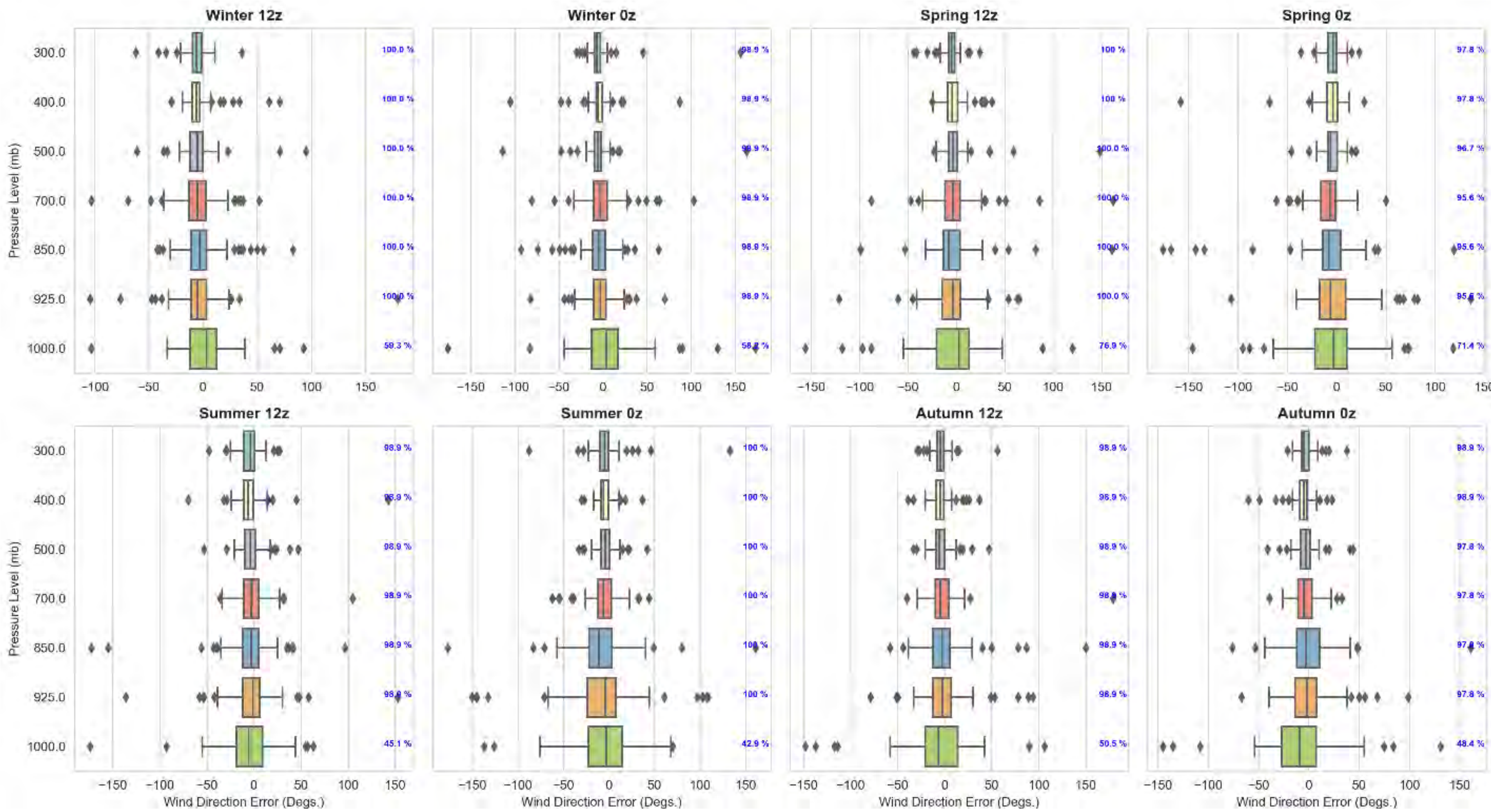

Figure 78. CYEV (Inuvik, Canada) upper-air distribution of wind direction error by pressure-level and season (dataset seasonal completeness indicated in blue).

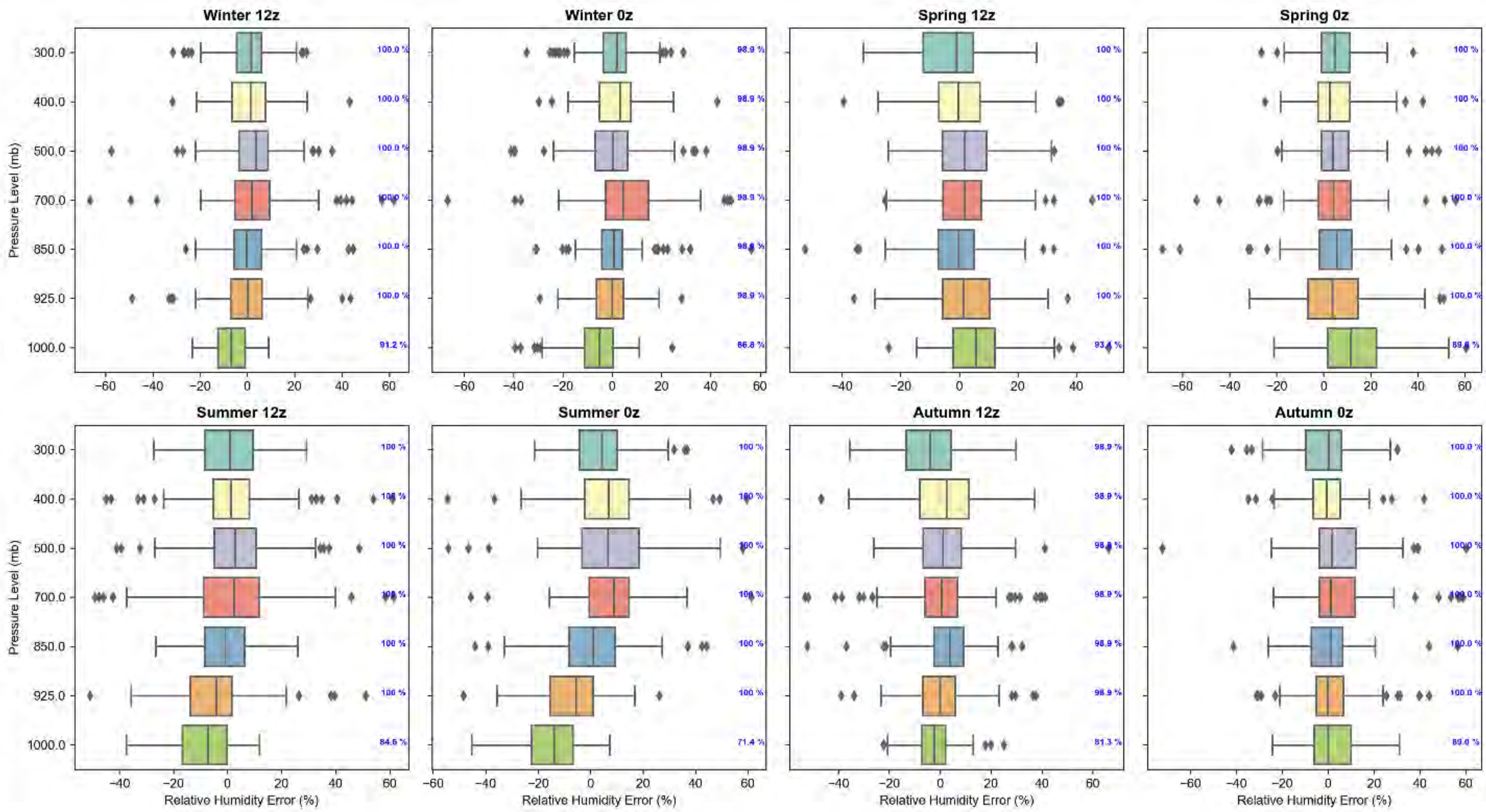

Figure 79. CYEV (Inuvik, Canada) upper-air distribution of relative humidity error by pressure-level and season (dataset seasonal completeness indicated in blue).

The PAFC (Anchorage) upper air station was selected to analyze performance in the center region of the WRF domain. The 0z and 12z sounding distributions of temperature, wind speed, wind direction, and relative humidity error per season are plotted in **Figure 80**,

Figure 81, **Figure 82**, and **Figure 83**, respectively. The results demonstrate WRF is biased warm in winter, autumn, and summer months near the surface but relatively unbiased aloft. Wind performance does not appear to be significantly biased aloft (few 1000 mb records of wind speed were available). Humidity is biased a bit dry nearer the surface and biased wet in the mid-levels most of the year.

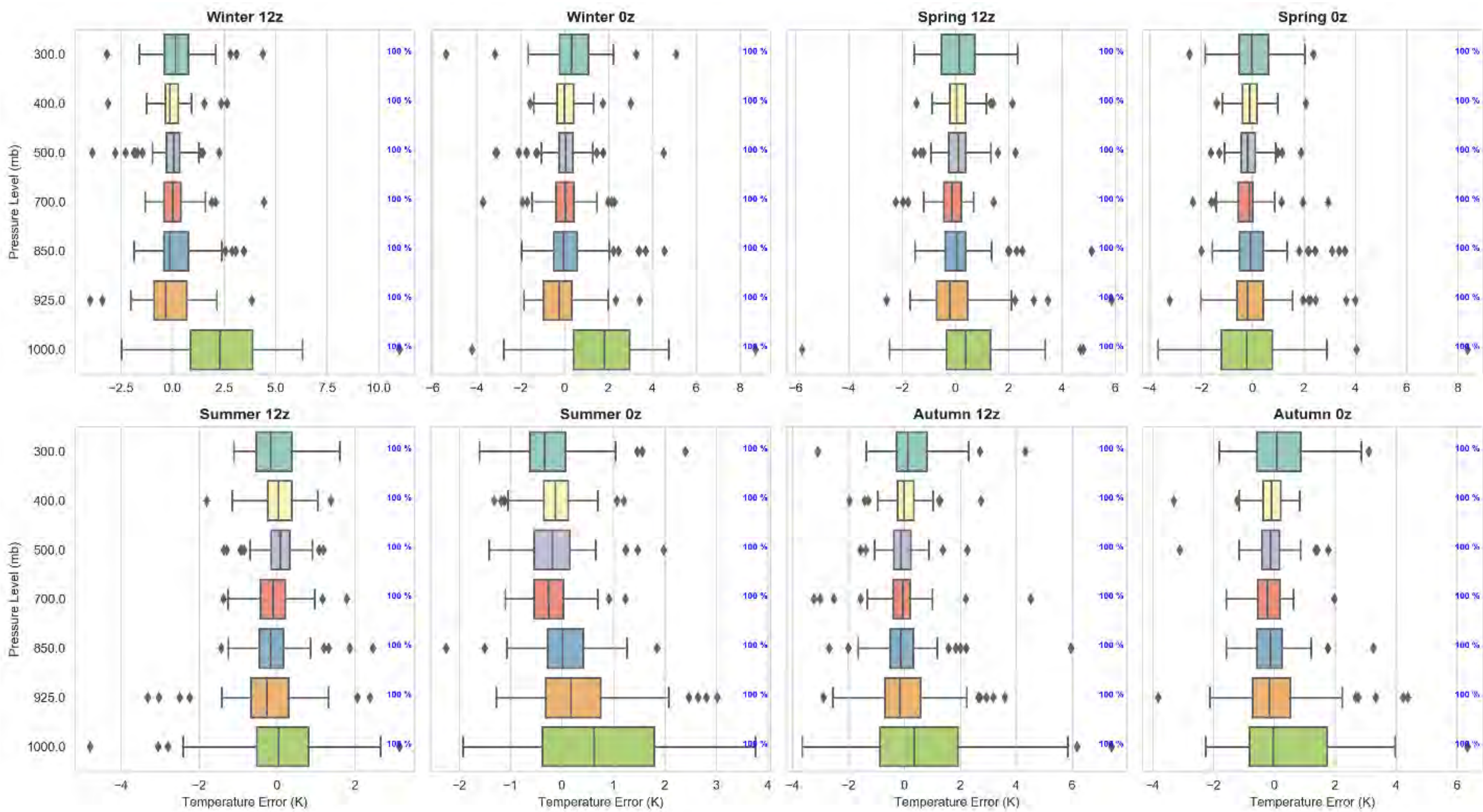

Figure 80. PAFC (Anchorage) upper-air distribution of temperature error by pressure-level and season (dataset seasonal completeness indicated in blue).

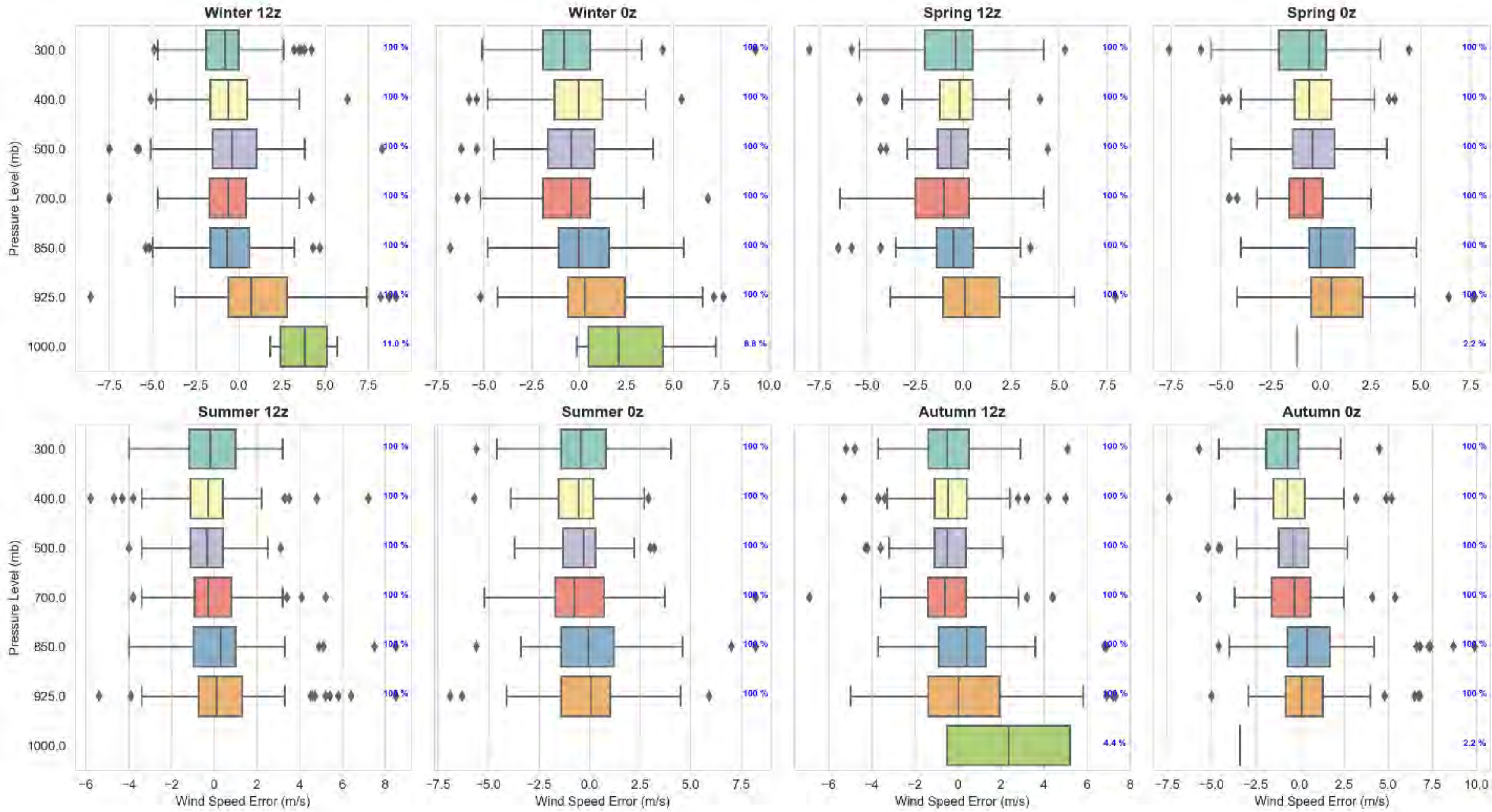

Figure 81. PAFC (Anchorage) upper-air distribution of wind speed error by pressure-level and season (dataset seasonal completeness indicated in blue).

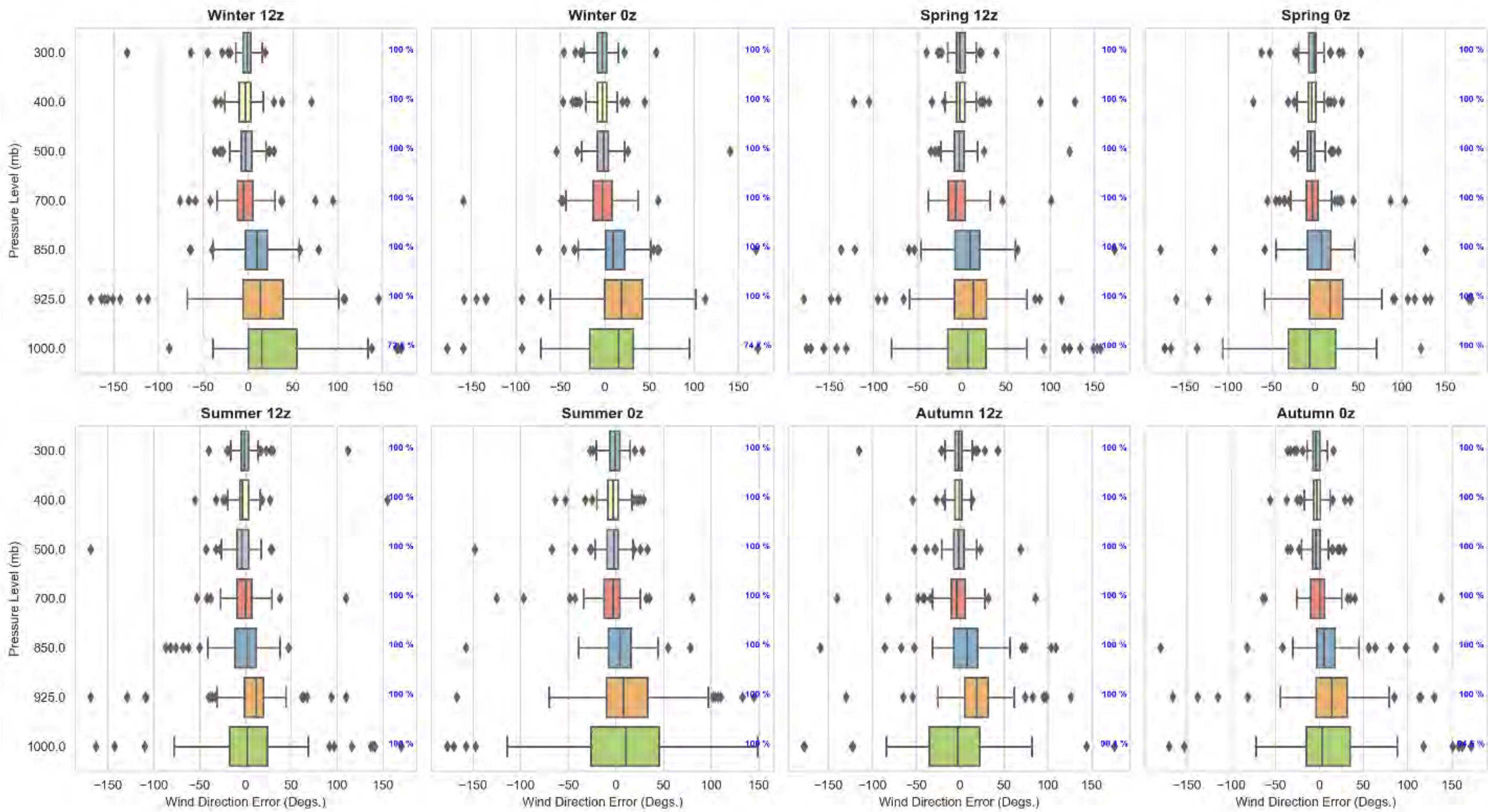

Figure 82. PAFC (Anchorage) upper-air distribution of wind direction error by pressure-level and season (dataset seasonal completeness indicated in blue).

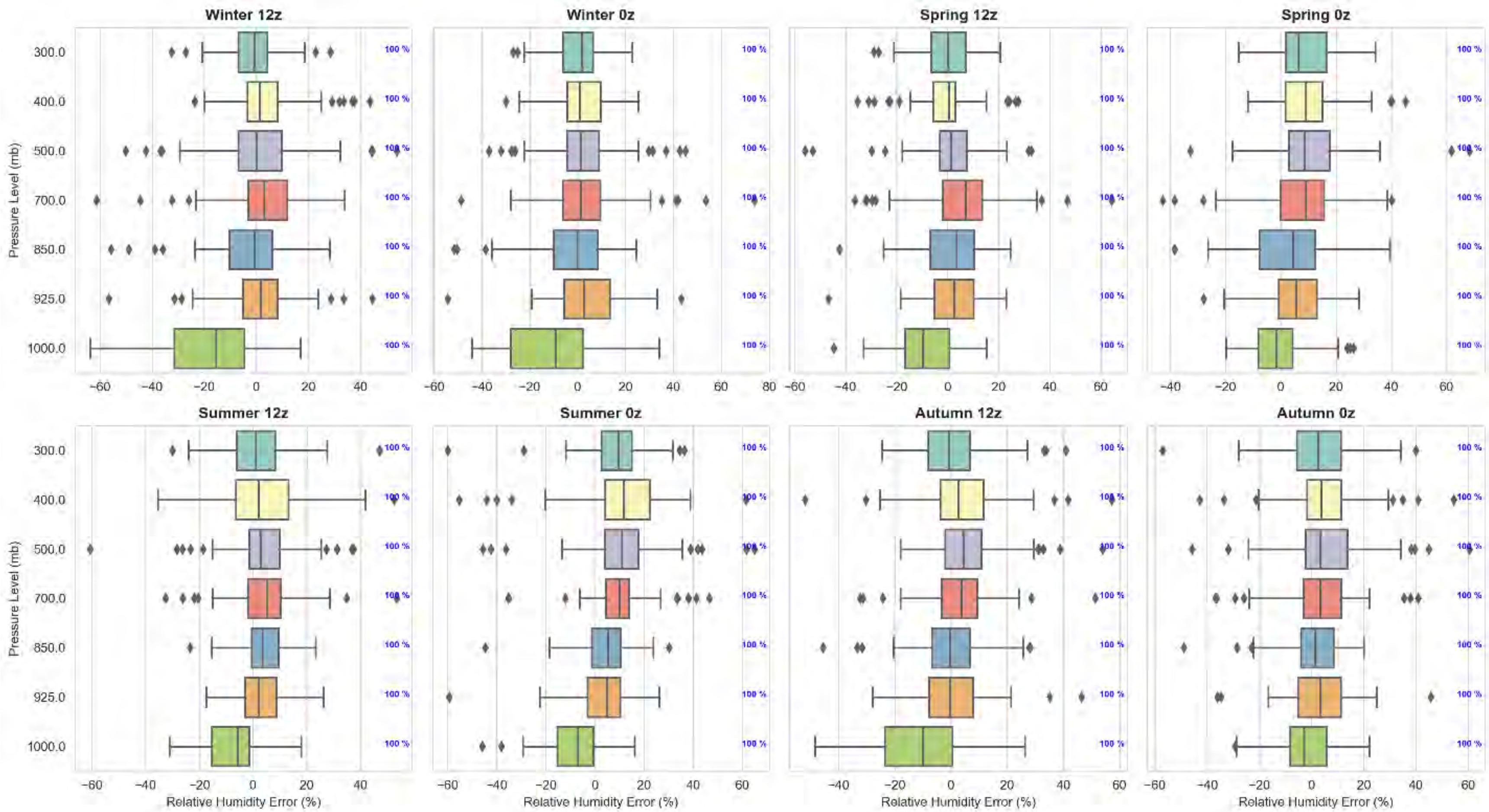

Figure 83. PAFC (Anchorage) upper-air distribution of relative humidity error by pressure-level and season (dataset seasonal completeness indicated in blue).

The PAFA (Fairbanks) upper air station was selected to analyze performance in the central inland part of the state, in the region of the Fairbanks $PM_{2.5}$ non-attainment area. The 0z and 12z sounding error distributions of temperature, wind speed, wind direction, and relative humidity per season are plotted in **Figure 84**, **Figure 85**, **Figure 86**, and **Figure 87**, respectively. Notably, the plots show a bias in temperature, wind speed, and relative humidity at the surface in winter, but less bias at higher pressure levels.

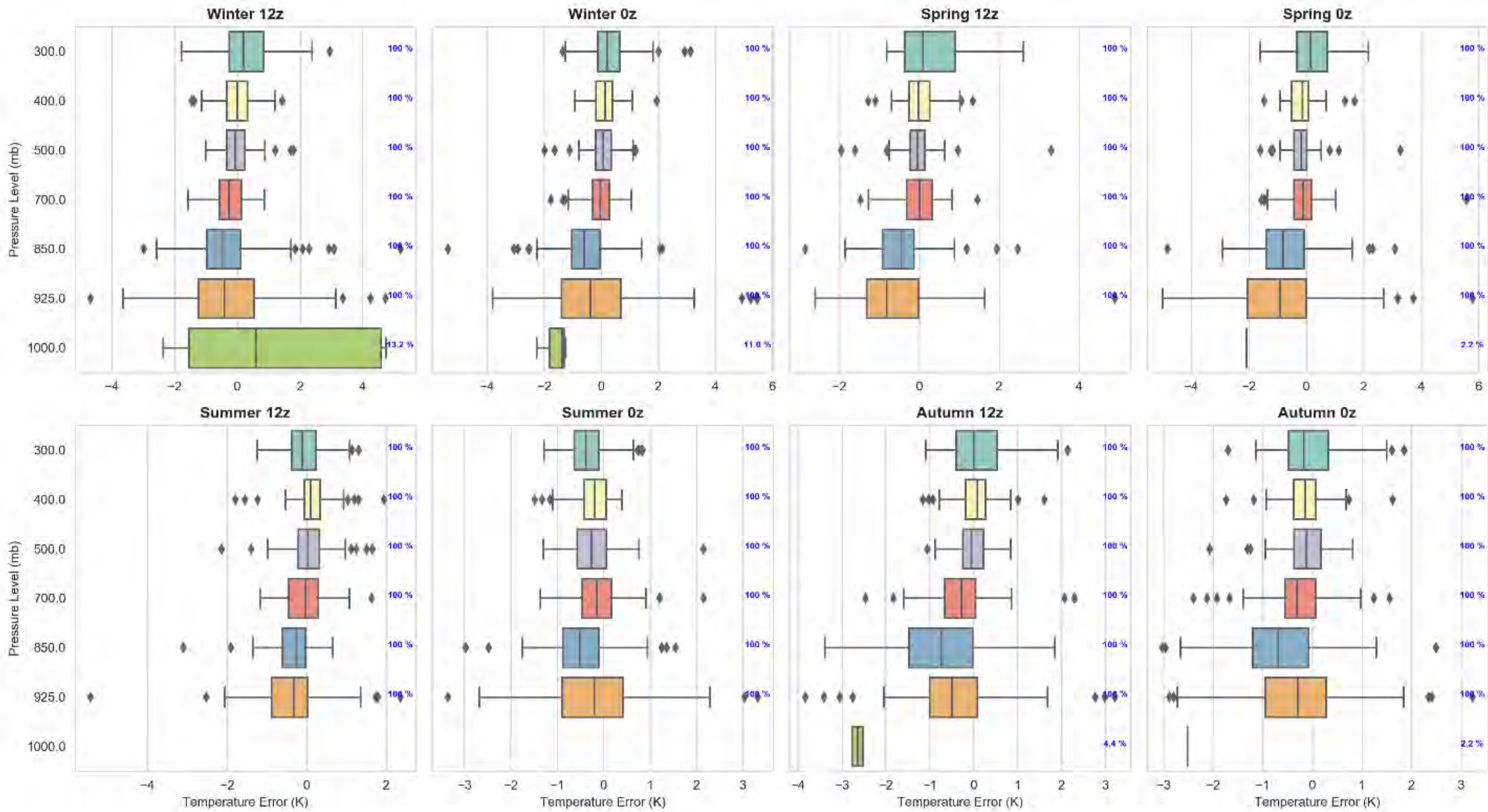

Figure 84. PAFA (Fairbanks) upper-air distribution of temperature error by pressure-level and season (dataset seasonal completeness indicated in blue).

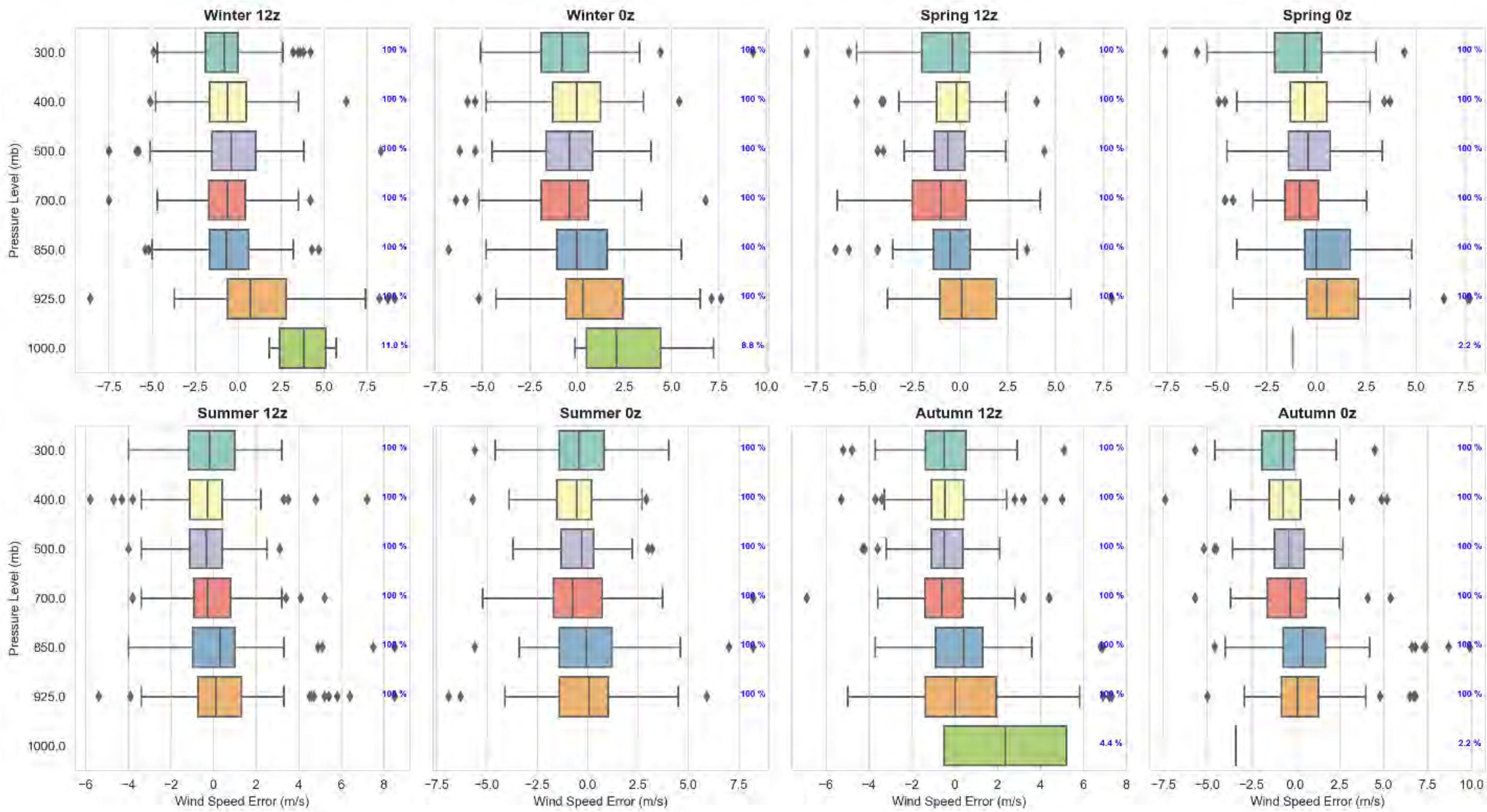

Figure 85. PAFA (Fairbanks) upper-air distribution of wind speed error by pressure-level and season (dataset seasonal completeness indicated in blue).

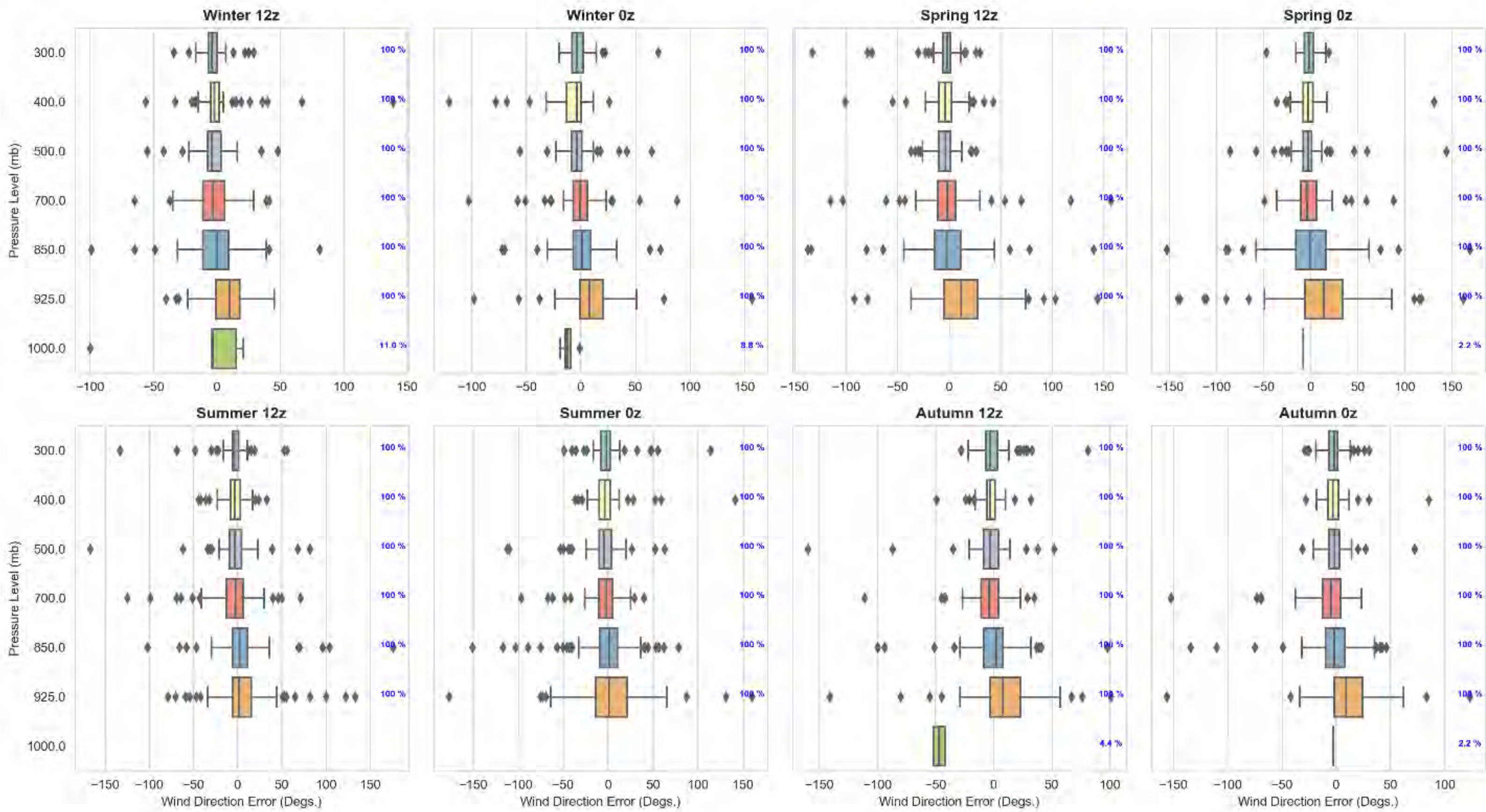

Figure 86. PAFA (Fairbanks) upper-air distribution of wind direction error by pressure-level and season (dataset seasonal completeness indicated in blue).

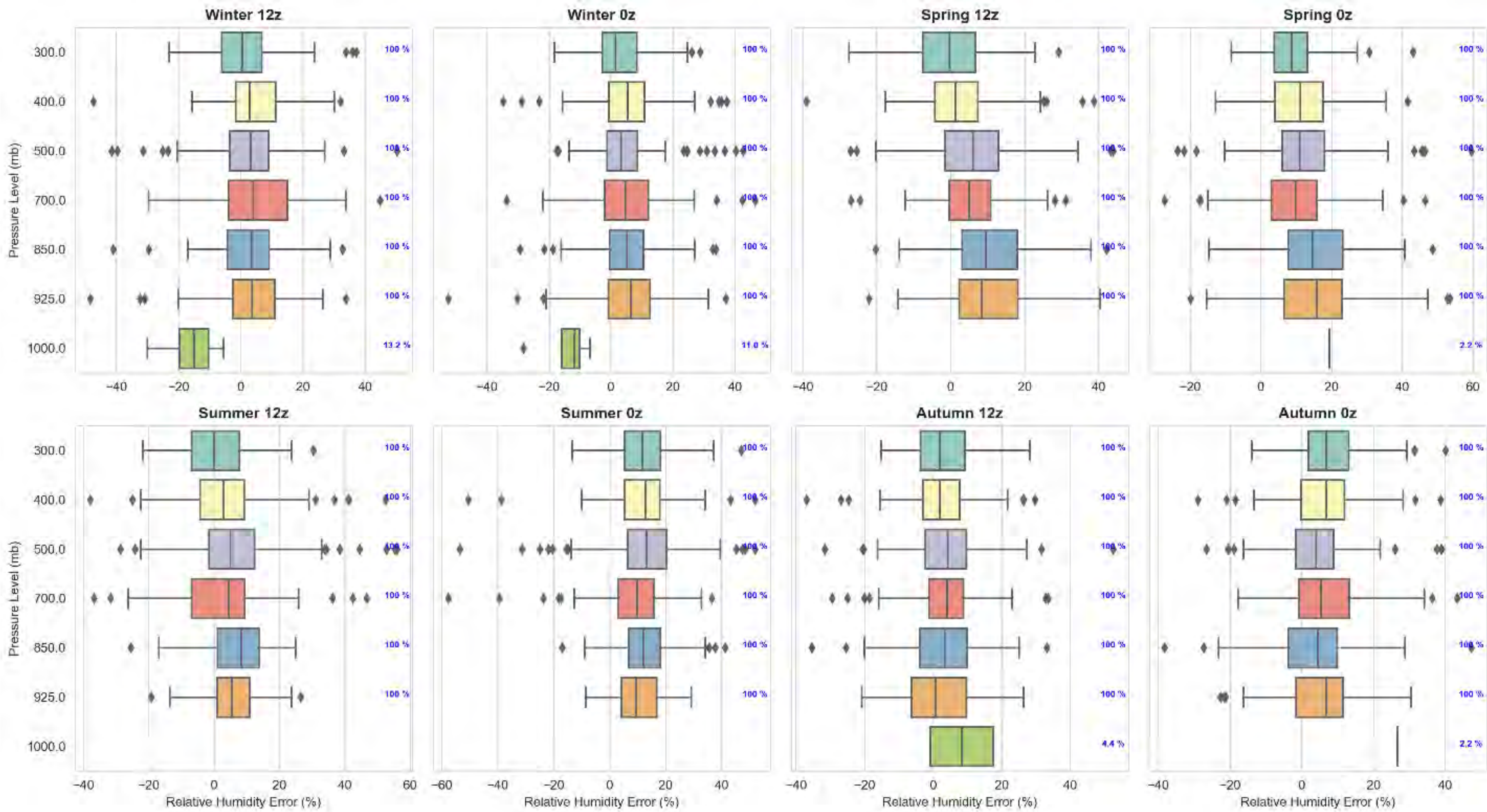

Figure 87. PAFA (Fairbanks) upper-air distribution of relative humidity error by pressure-level and season (dataset seasonal completeness indicated in blue).

The PABR (Utqiagvik/Barrow) upper air station was selected to analyze performance at the most northern upper-air station in the domain. The 0z and 12z sounding distributions of temperature, wind speed, wind direction, and relative humidity error per season are plotted in **Figure 88**, **Figure 89**, **Figure 90**, and **Figure 91**, respectively. There is a wide distribution of temperature error near the surface, but predicted temperatures aloft are generally unbiased and accurate. Wind speed and direction error and bias are also relatively low at all heights. Relative humidity is biased low near the surface, especially in winter.

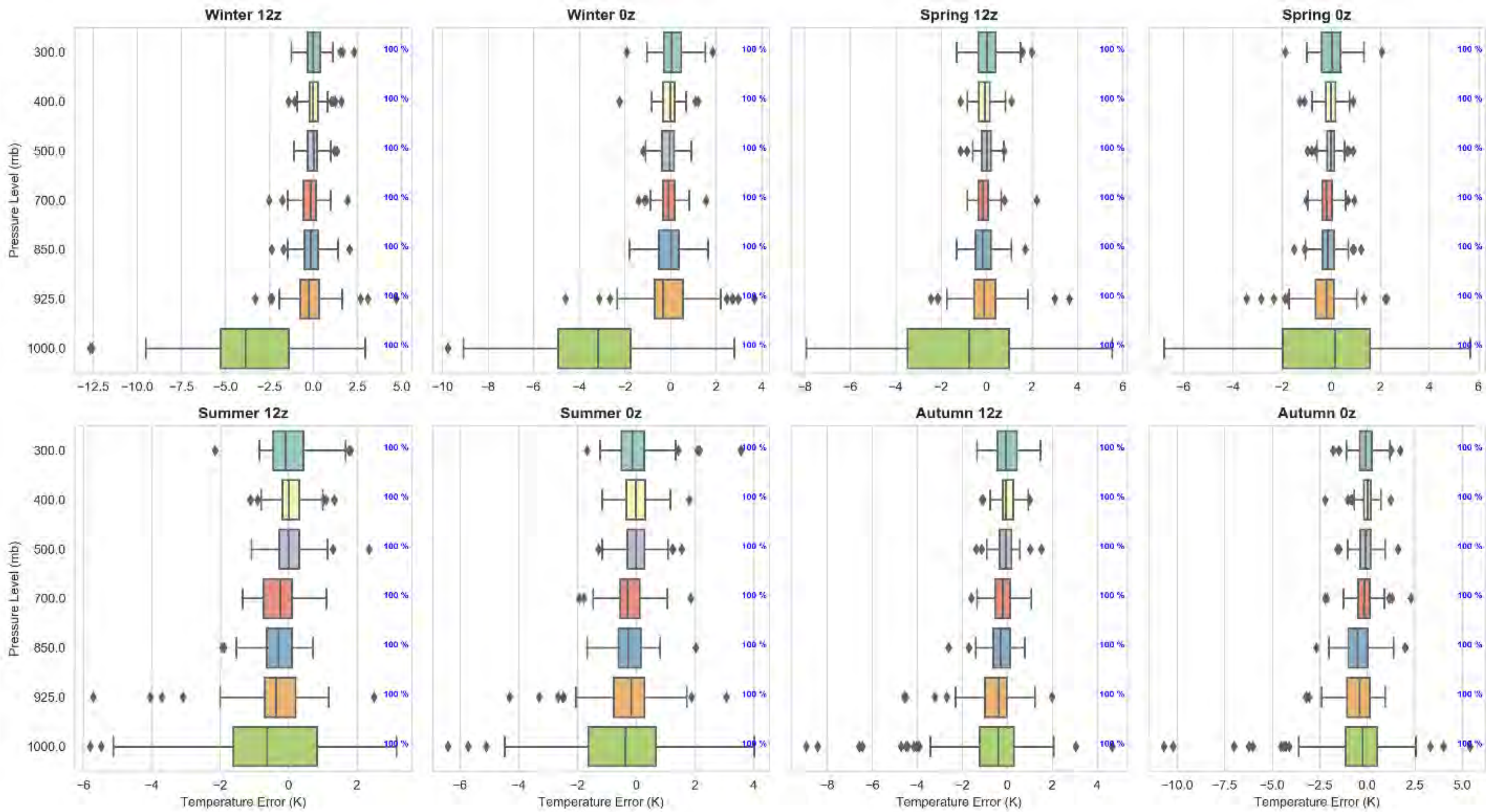

Figure 88. PABR (Utqiagvik) upper-air distribution of temperature error by pressure-level and season (dataset seasonal completeness indicated in blue).

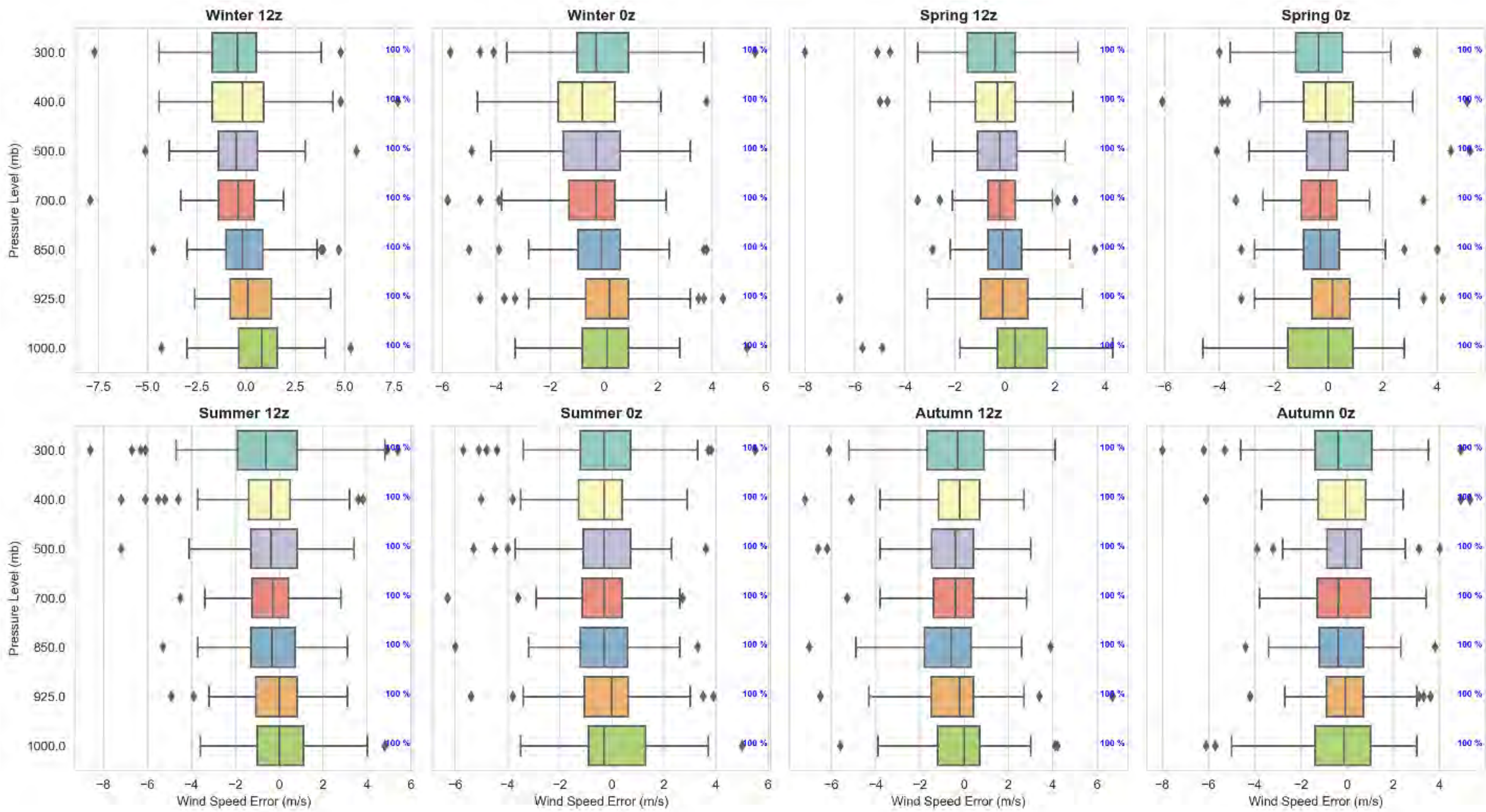

Figure 89. PABR (Utqiagvik) upper-air distribution of wind speed error by pressure-level and season (dataset seasonal completeness indicated in blue).

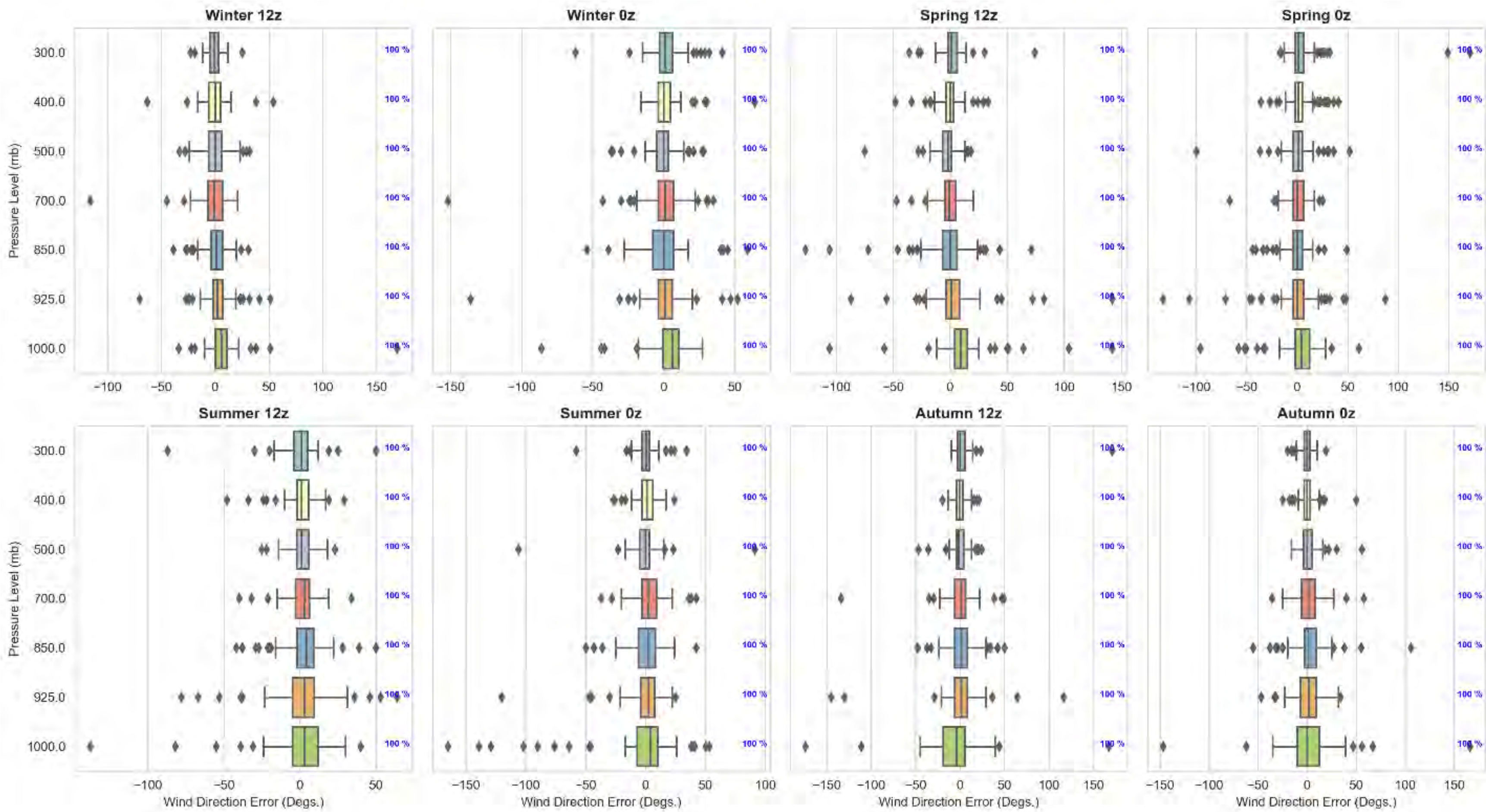

Figure 90. PABR (Utqiagvik) upper-air distribution of wind direction error by pressure-level and season (dataset seasonal completeness indicated in blue).

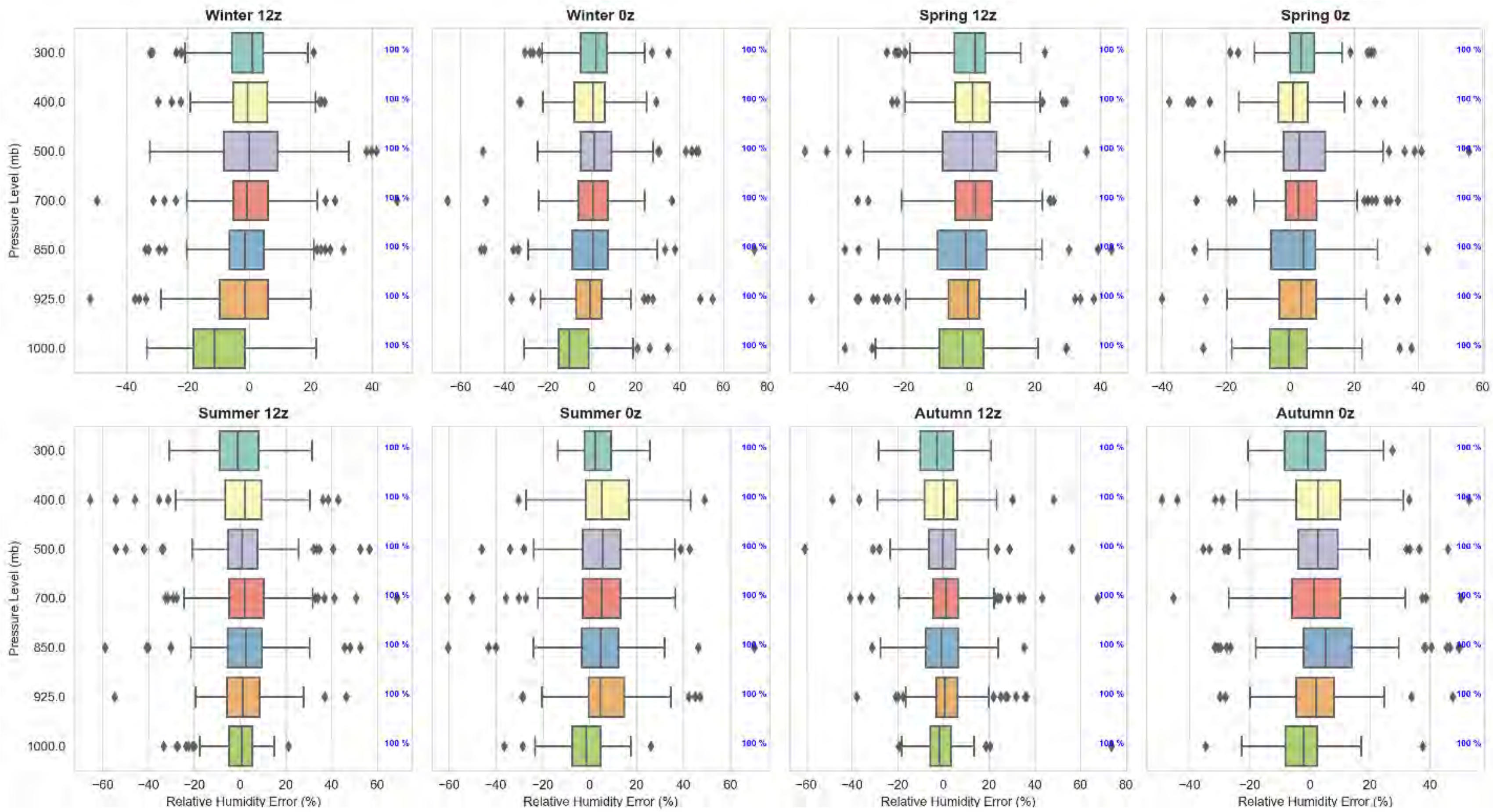

Figure 91. PABR (Utqiagvik) upper-air distribution of relative humidity error by pressure-level and season (dataset seasonal completeness indicated in blue).

The PASN (St. Paul Island) upper air station was selected to analyze performance in the western marine portions of the domain. The 0z and 12z sounding error distributions of temperature, wind speed, wind direction, and relative humidity per season are plotted in **Figure 92**, **Figure 93**, **Figure 94**, and **Figure 95**, respectively. WRF near-surface temperatures are biased cool in spring and autumn months, but generally unbiased aloft. Wind performance appears good, with low wind speed and direction error across all layers.

Relative humidity is biased a bit high (wetter) in lower layers across all seasons.

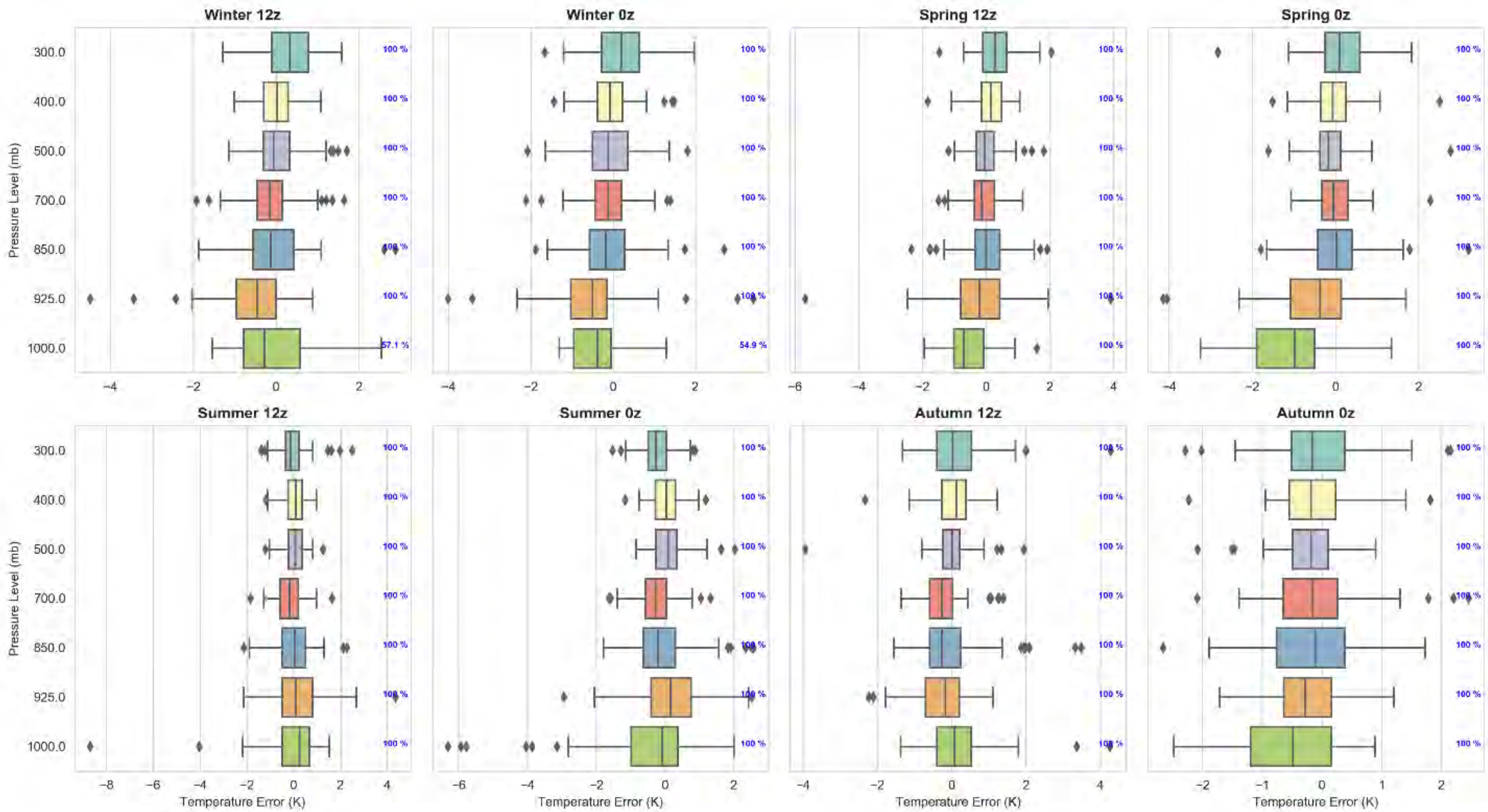

Figure 92. PASN (St. Paul Island) upper-air distribution of temperature error by pressure-level and season (dataset seasonal completeness indicated in blue).

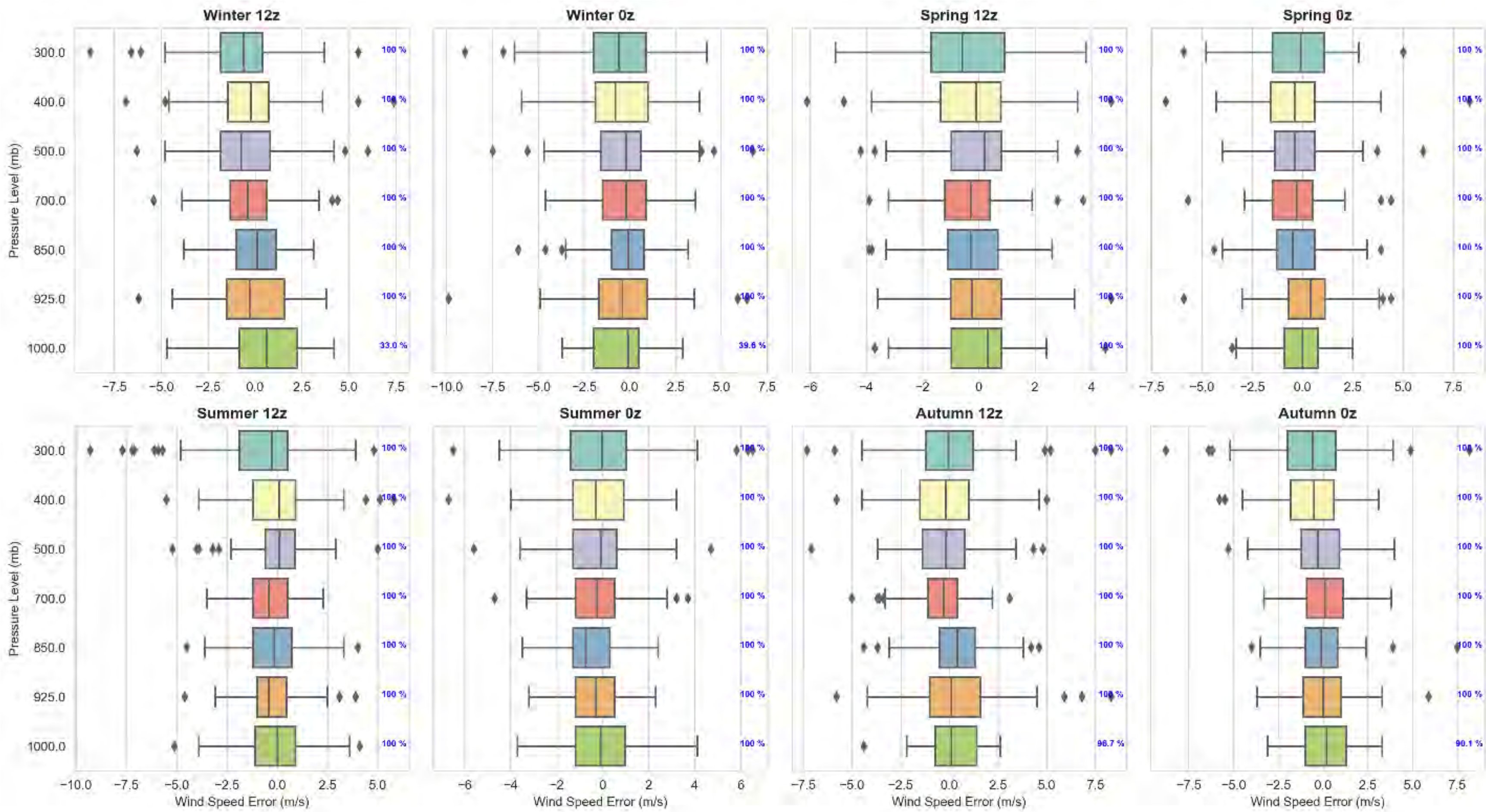

Figure 93. PASN (St. Paul Island) upper-air distribution of wind speed error by pressure-level and season (dataset seasonal completeness indicated in blue).

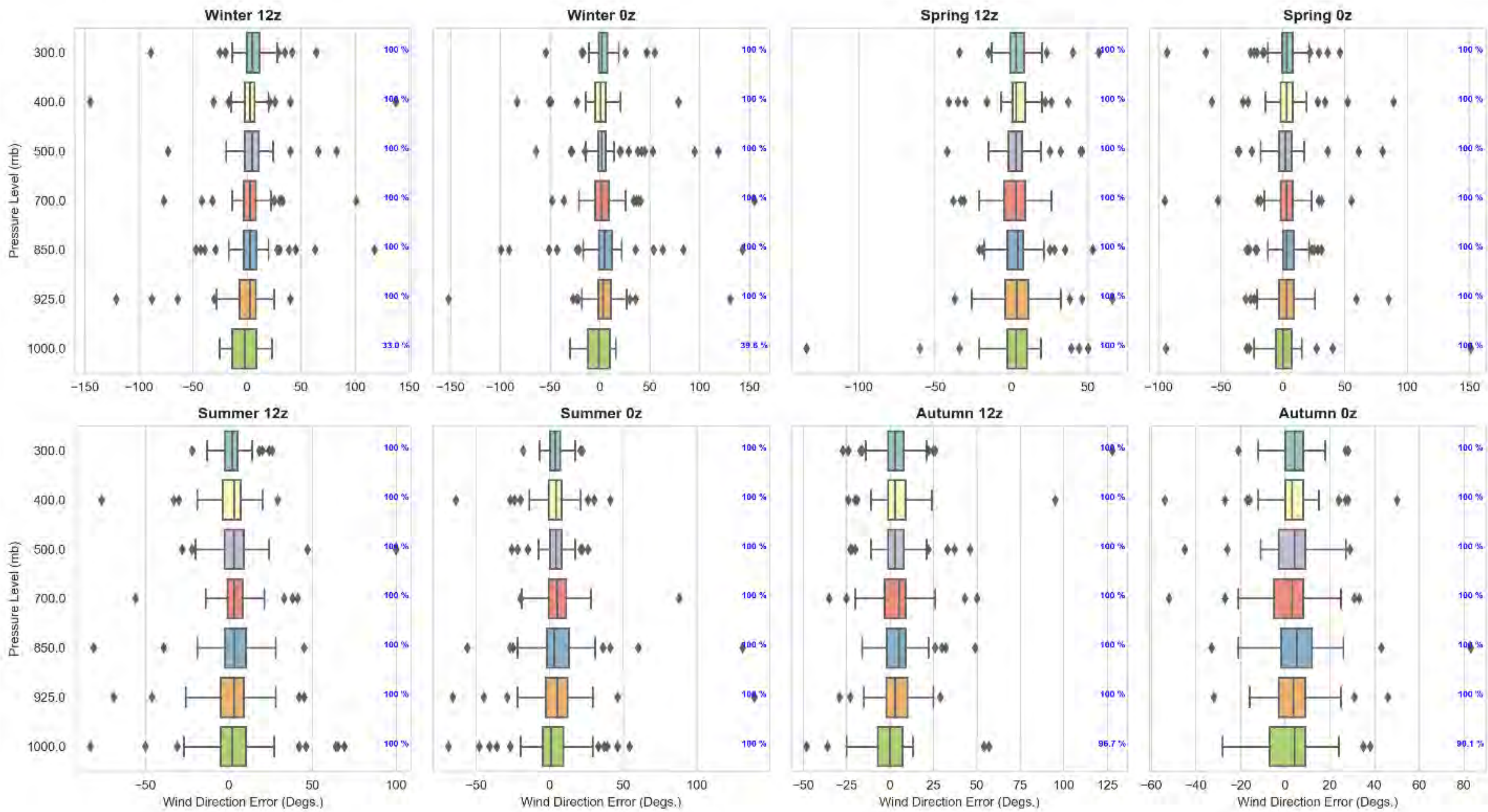

Figure 94. PASN (St. Paul Island) upper-air distribution of wind direction error by pressure-level and season (dataset seasonal completeness indicated in blue).

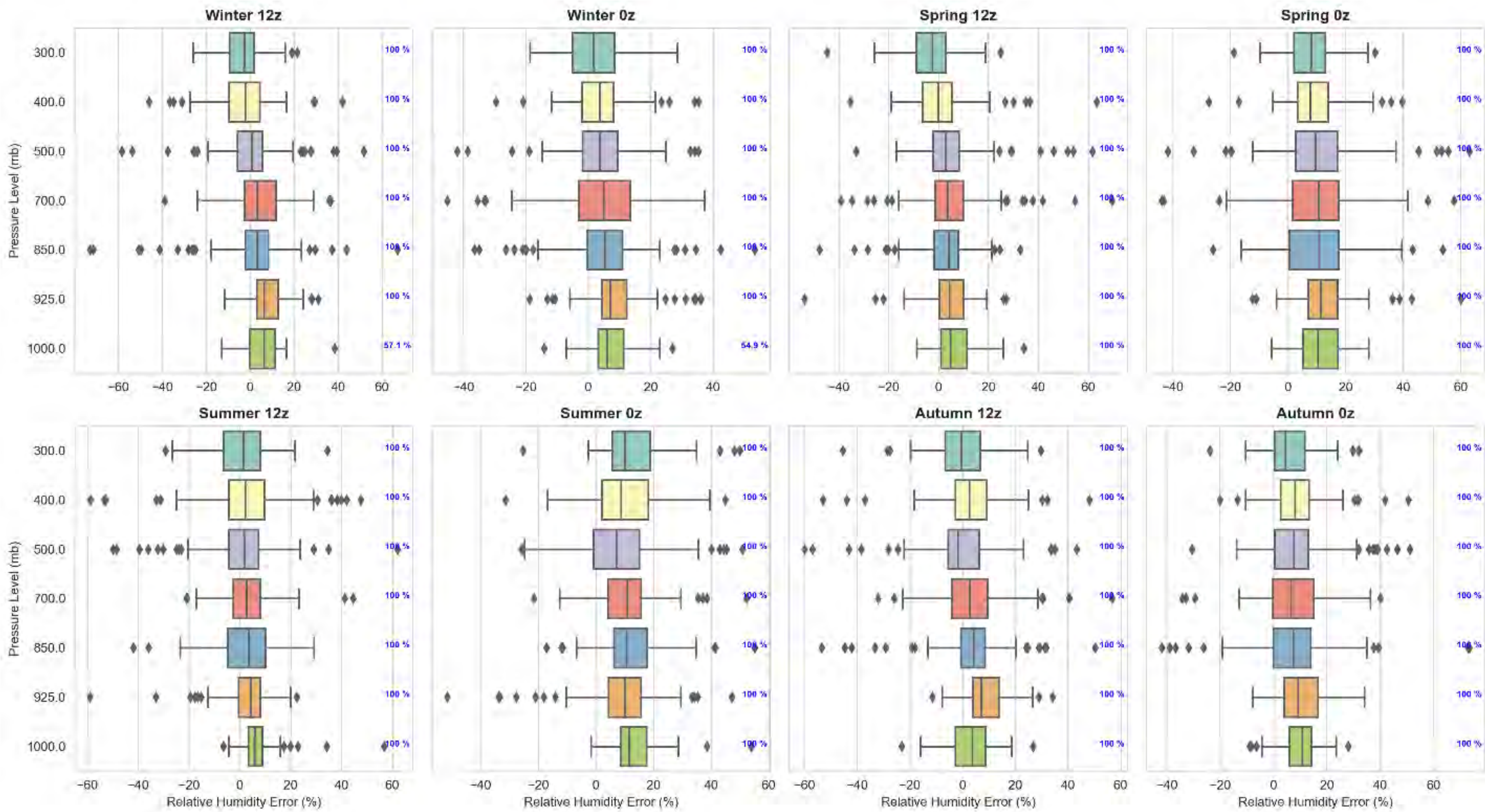

Figure 95. PASN (St. Paul Island) upper-air distribution of relative humidity error by pressure-level and season (dataset seasonal completeness indicated in blue).

The PANT (Annette Island, Alaska) upper air station was selected to analyze performance in the southeastern portions of the domain. PANT is located just south of Ketchikan, Alaska, about 200 miles south of Juneau. The 0z and 12z sounding error distributions of temperature, wind speed, wind direction, and relative humidity per season are plotted in **Figure 96**, **Figure 97**, **Figure 98**, and **Figure**

99, respectively. Overall, wind speed and direction error aloft is low. The moist bias seen in the other upper-air datasets is also prevalent in the PANT dataset, especially in spring.

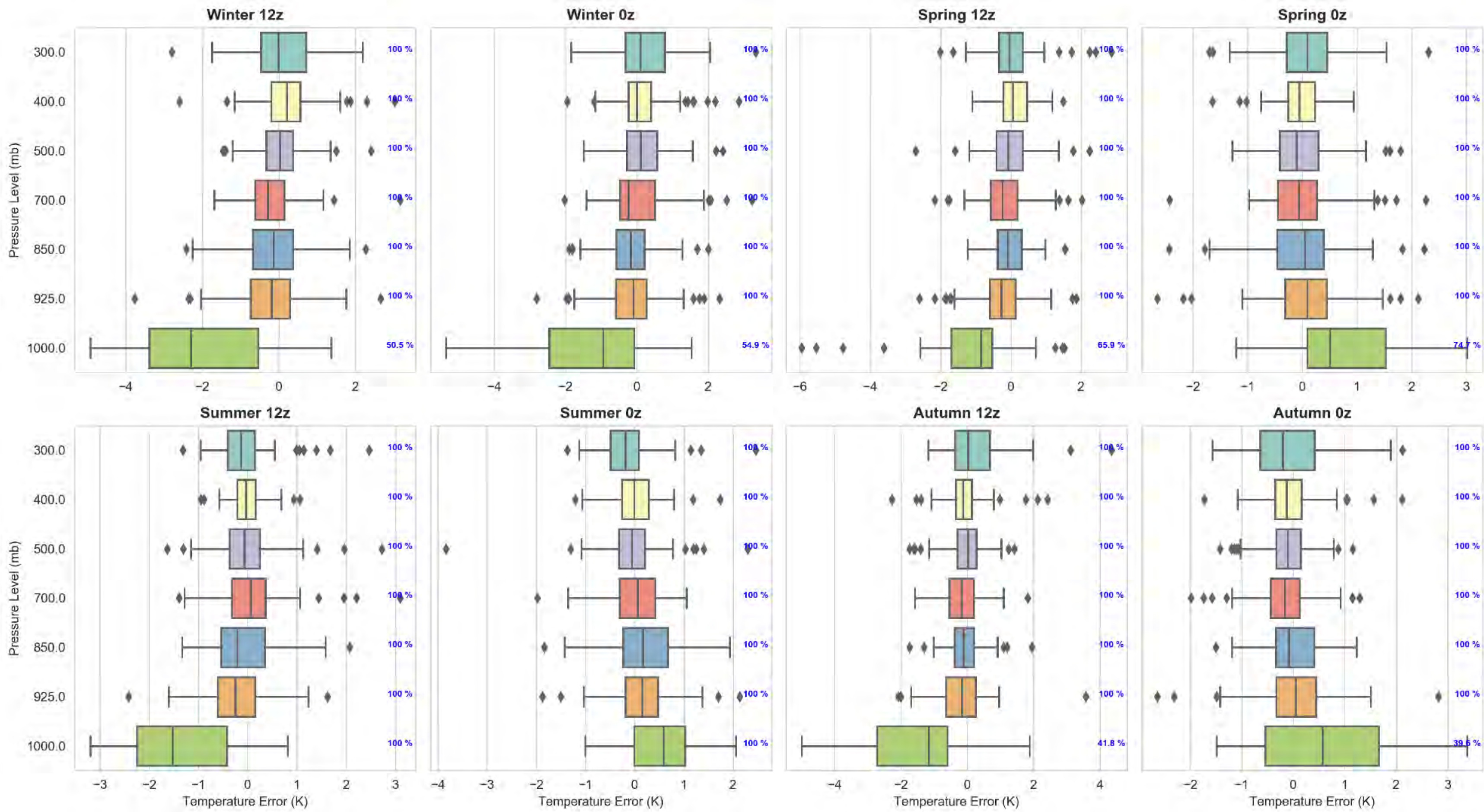

Figure 96. PANT (Annette Island) upper-air distribution of temperature error by pressure-level and season (dataset seasonal completeness indicated in blue).

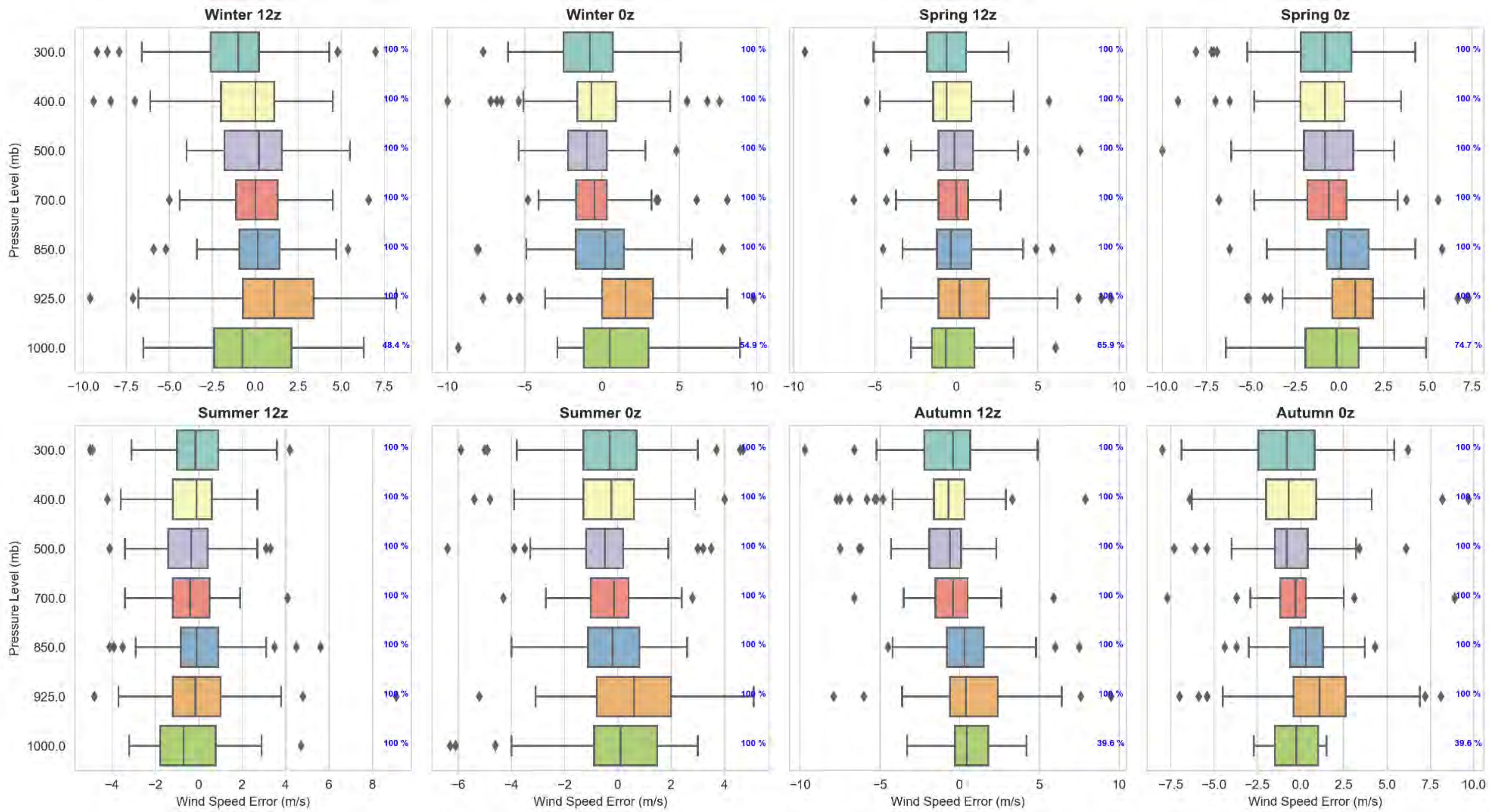

Figure 97. PANT (Annette Island) upper-air distribution of wind speed error by pressure-level and season (dataset seasonal completeness indicated in blue).

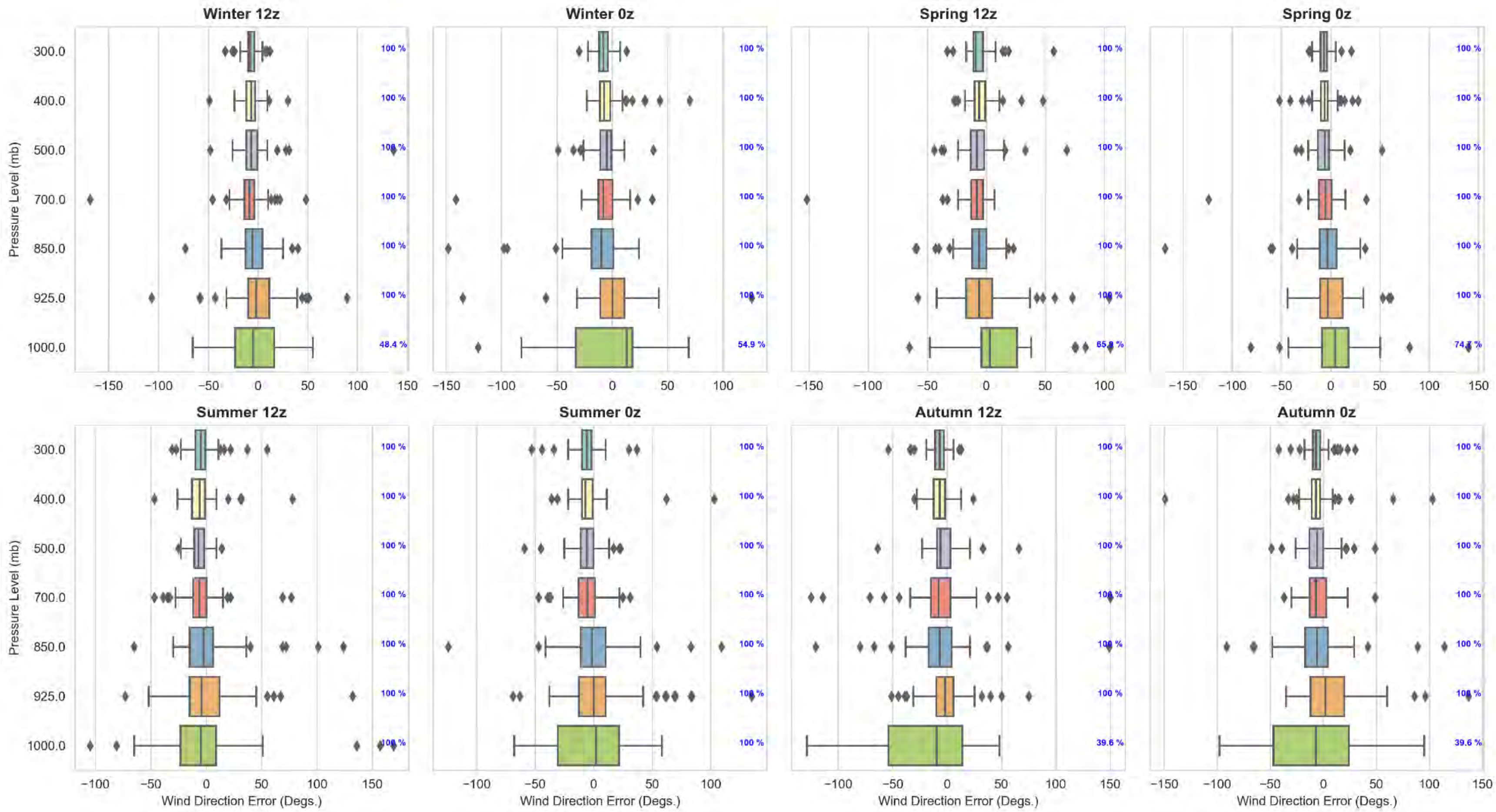

Figure 98. PANT (Annette Island) upper-air distribution of wind direction error by pressure-level and season (dataset seasonal completeness indicated in blue).

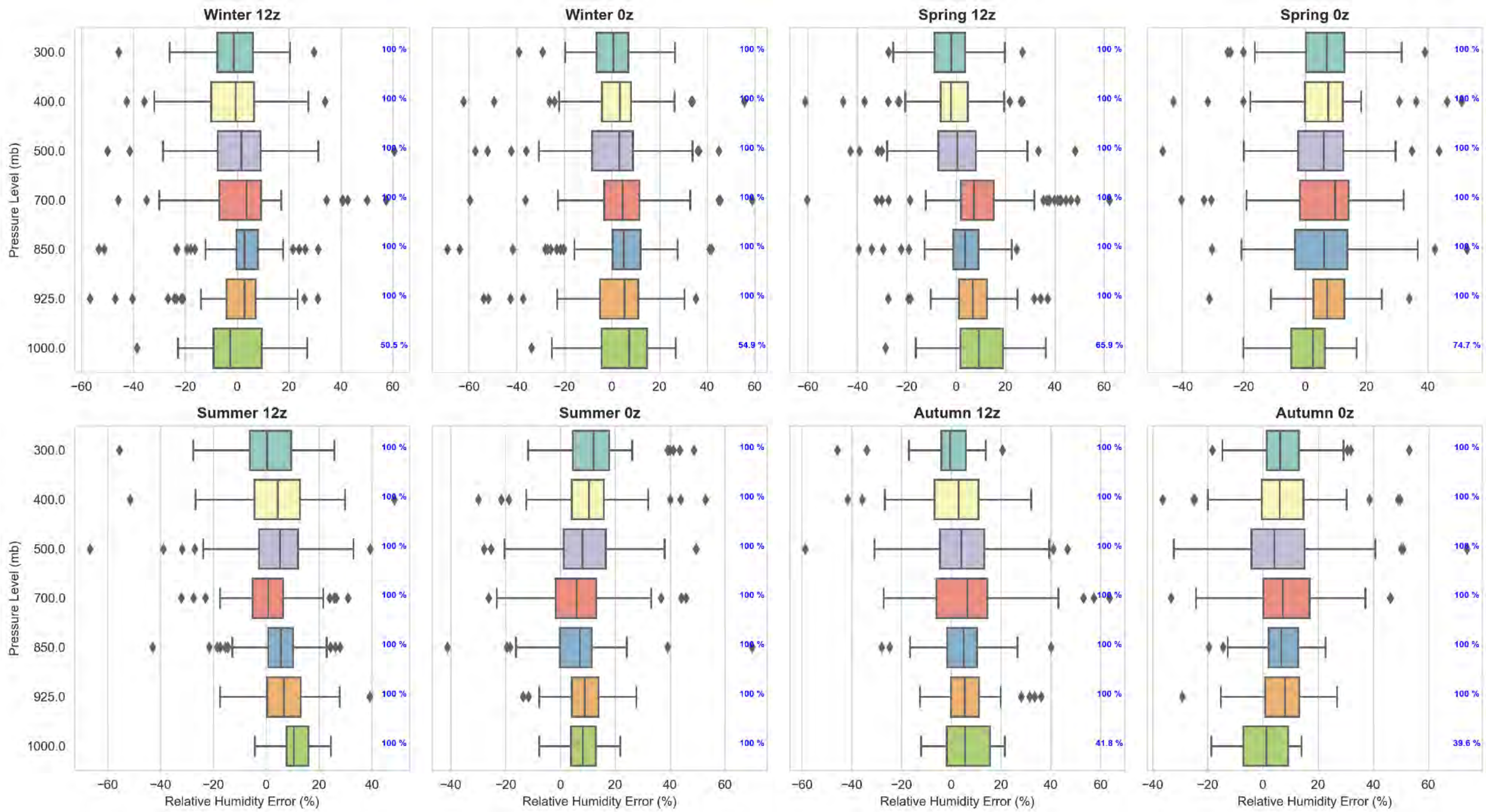

Figure 99. PANT (Annette Island) upper-air distribution of relative humidity error by pressure-level and season (dataset seasonal completeness indicated in blue).

4.8 Precipitation

Plots of monthly-averaged precipitation (in liquid-equivalent inches) determined from the 2016 WRF Alaska run are compared to NOAA-NCEP measured precipitation maps in this section. First quarter precipitation comparisons for January, February, and March are plotted in **Figure 100**, **Figure 101**, and **Figure 102**, respectively. The precipitation patterns across the state predicted by WRF match the NOAA-NCEP maps well. One notable difference is WRF predicts considerably more precipitation along the east slopes of the Alaska range and western Cook Inlet in January and February. WRF also tends to be a bit wetter in northwestern Alaska, more specifically in the Brooks Range northeast of Kotzebue Sound.

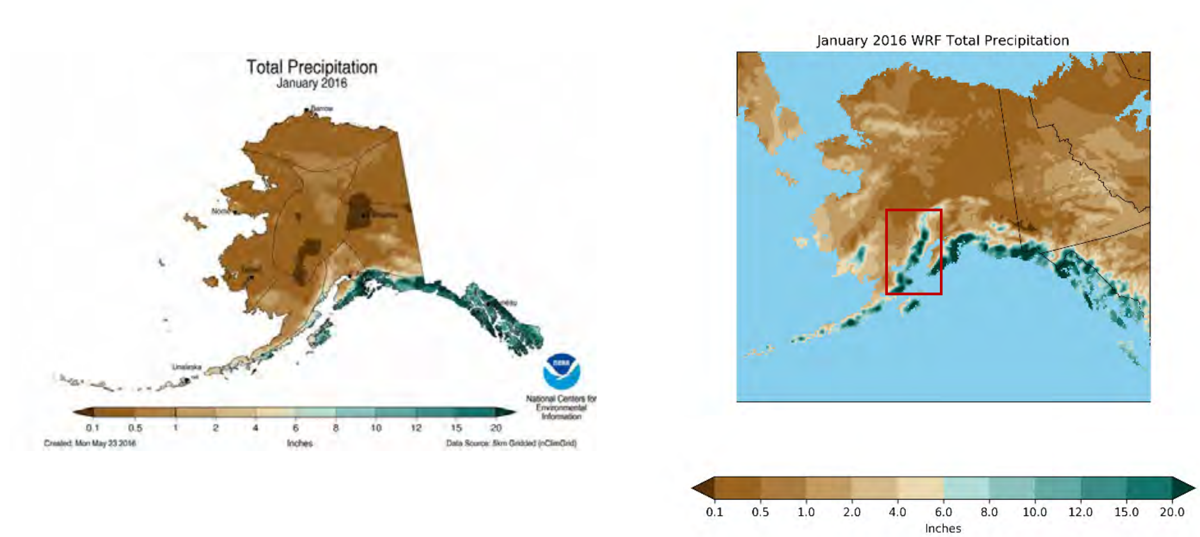

Figure 100. January 2016 monthly total precipitation, Alaska 9-km WRF (right) compared to NOAA-NCEP GHCN dataset map (left). The area of significant difference along west of Cook Inlet is highlighted by the red box.

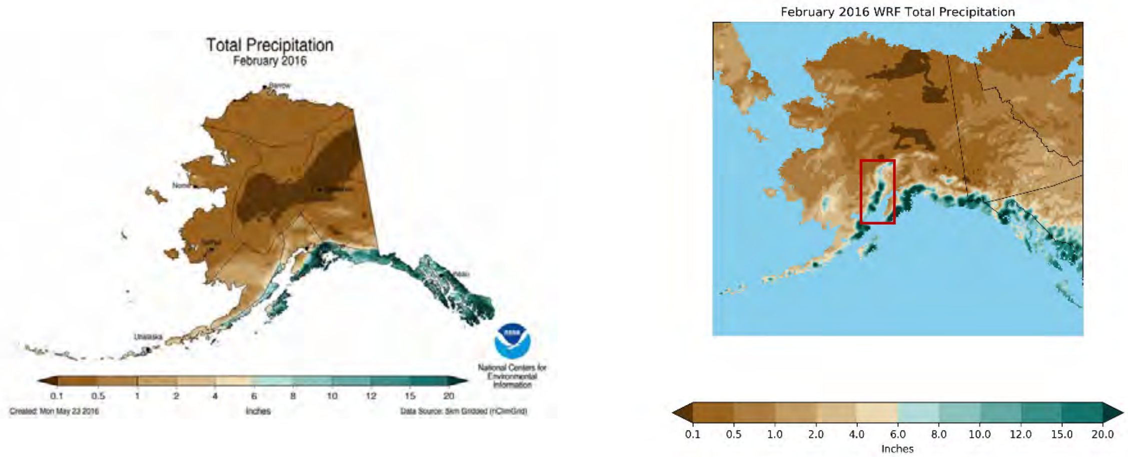

Figure 101. February 2016 monthly total precipitation, Alaska 9-km WRF (right) compared to NOAA-NCEP GHCN dataset map (left). The area of significant difference west of Cook Inlet is highlighted by the red box.

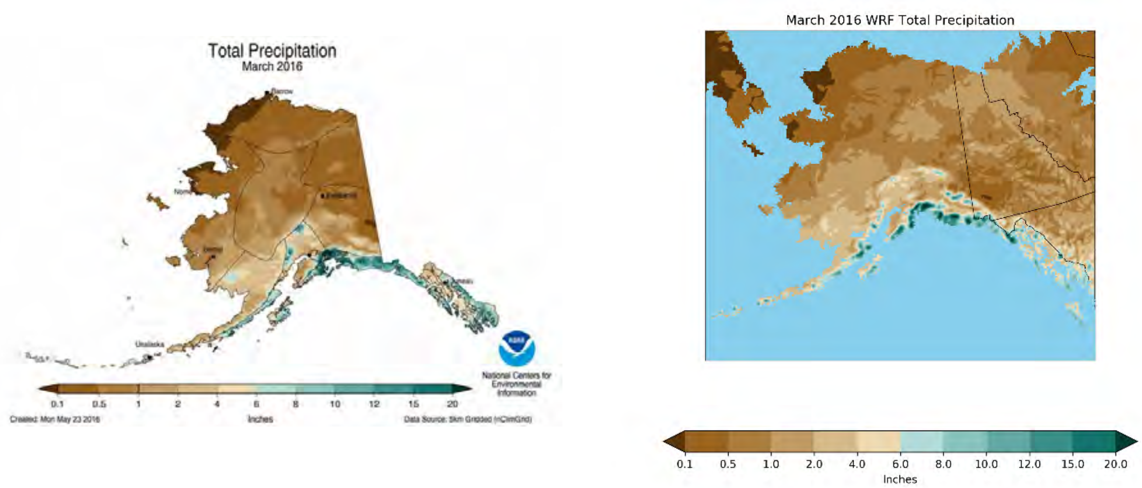

Figure 102. March 2016 monthly total precipitation, Alaska 9-km WRF (right) compared to NOAA-NCEP GHCN dataset map (left).

Second quarter precipitation comparisons for April, May, and June are shown in **Figure 103**, **Figure 104**, and **Figure 105**, respectively. Again, the overall precipitation patterns appear to be well simulated by the WRF model. Notable differences include excessive precipitation over the Alaska Range west of Cook Inlet in April, too little precipitation in the Chugach Range of southeast Alaska and Togiak River valley of southwest Alaska in May, and too much precipitation in the Wrangell-St. Elias mountains of southeast Alaska in June.

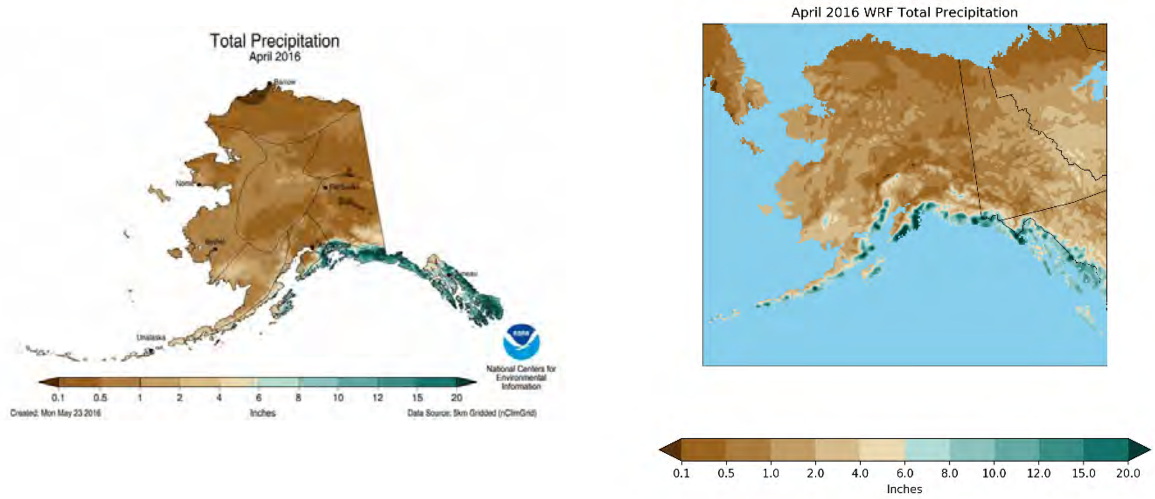

Figure 103. April 2016 monthly total precipitation, Alaska 9-km WRF (right) compared to NOAA-NCEP GHCN dataset map (left). The area of significant difference west of Cook Inlet is highlighted by the red box.

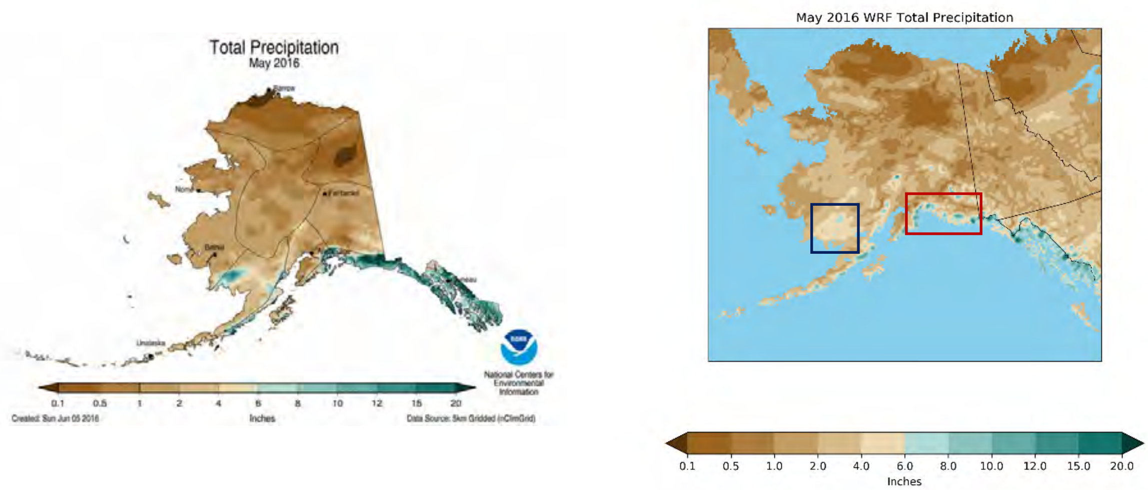

Figure 104. May 2016 monthly total precipitation, Alaska 9-km WRF (right) compared to NOAA-NCEP GHCN dataset map (left). Underprediction in Chugach Range and Tohiak Valley highlighted by the red and blue boxes, respectively.

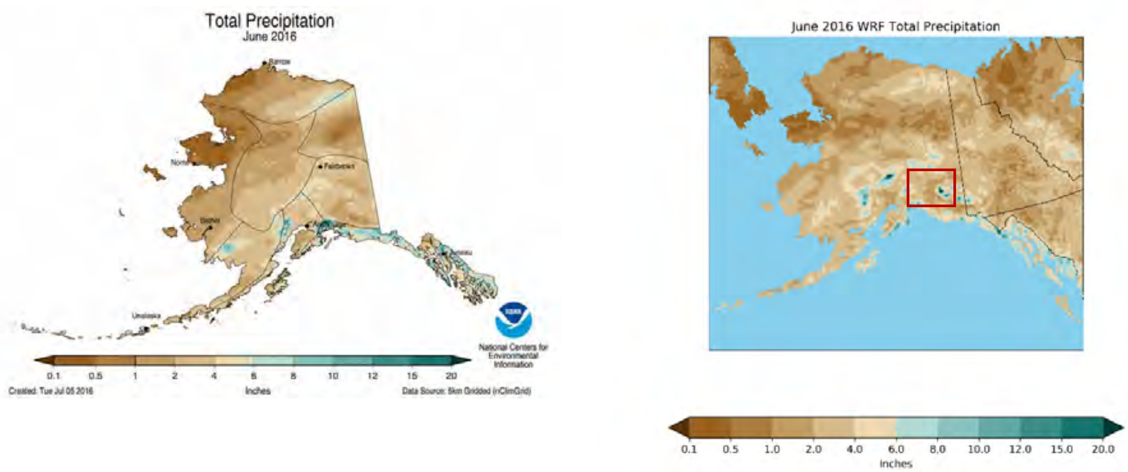

Figure 105. June 2016 monthly total precipitation, Alaska 9-km WRF (right) compared to NOAA-NCEP GHCN dataset map (left). Area of overprediction in the Wrangell-St. Elias National Park region highlighted by red box.

Third quarter precipitation comparisons for July, August, and September are shown in **Figure 106**, **Figure 107**, and **Figure 108**, respectively. The summer patterns of precipitation appear to be simulated well by WRF. A few notable differences include some excessive precipitation across west-central Alaska in July and along the central Brooks Range in August. WRF also appears to overpredict precipitation in Wrangell-St. Elias mountains of southwest Alaska in September.

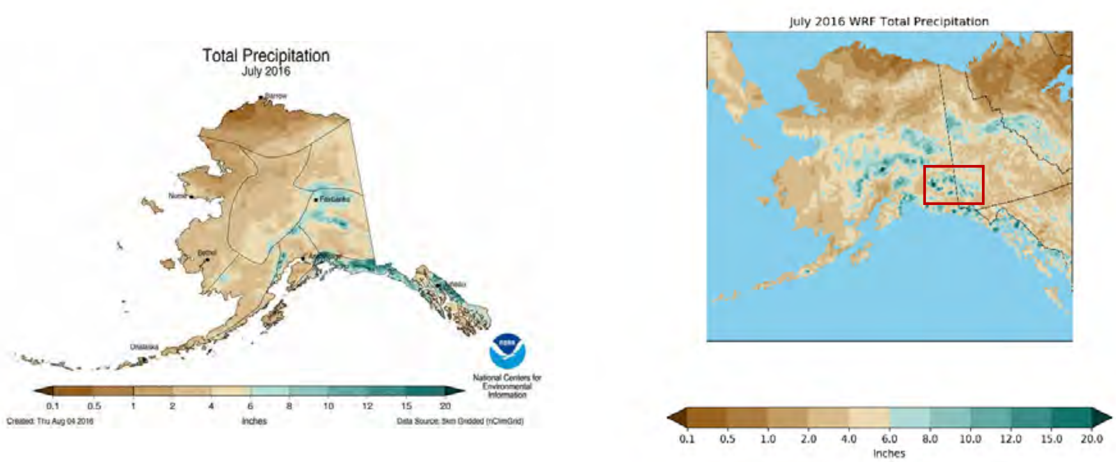

Figure 106. July 2016 monthly total precipitation, Alaska 9-km WRF (right) compared to NOAA-NCEP GHCN dataset map (left). Overpredicted precipitation in Wrangell-St. Elias range highlighted by red box.

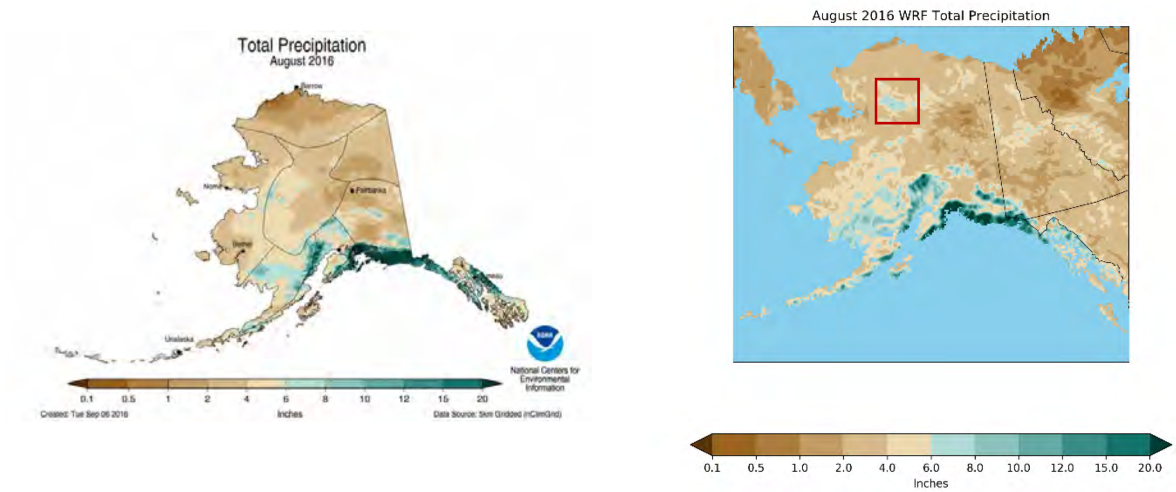

Figure 107. August 2016 monthly total precipitation, Alaska 9-km WRF (right) compared to NOAA-NCEP GHCN dataset map (left). Region of overprediction highlighted by red box in the central Brooks Range.

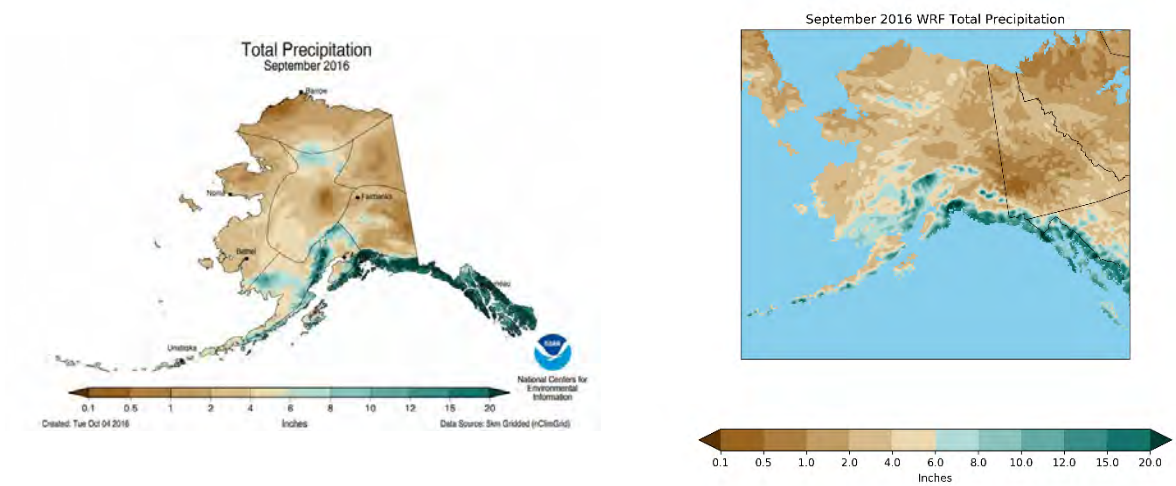

Figure 108. September 2016 monthly total precipitation, Alaska 9-km WRF (right) compared to NOAA-NCEP GHCN dataset map (left).

Fourth quarter precipitation, represented by the October, November, and December plots, is shown in **Figure 109**, **Figure 110**, and **Figure 111**, respectively. Again, the precipitation patterns predicted by WRF appear to match the observation-based maps well. It appears WRF may underpredict precipitation over the Chugach mountains in October. November and December patterns match the observation-based maps very well with no notable regional differences.

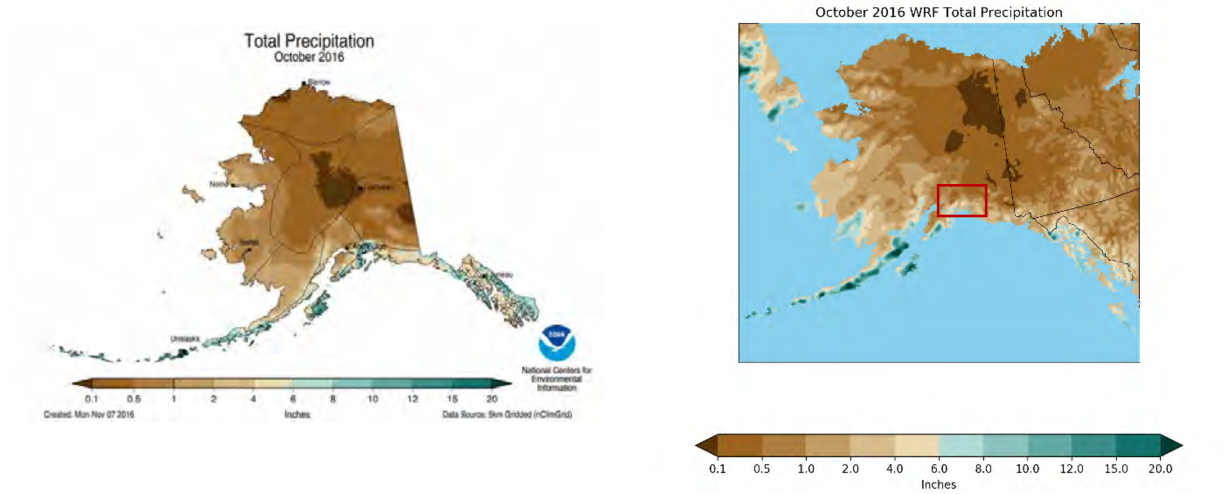

Figure 109. October 2016 monthly total precipitation, Alaska 9-km WRF (right) compared to NOAA-NCEP GHCN dataset map (left). Area of underprediction, in the Chugach Mountains area, highlighted by red box.

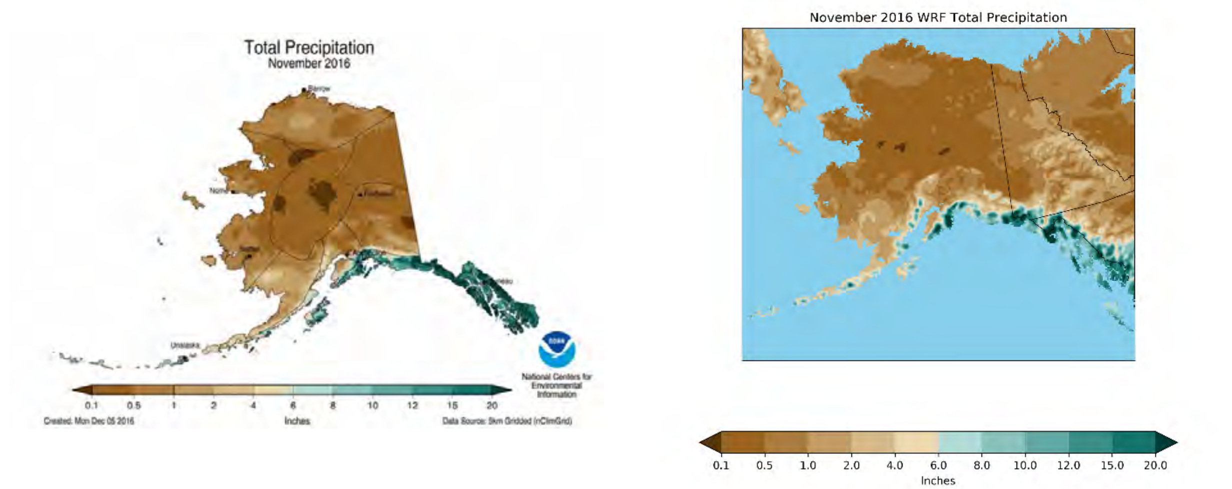

Figure 110. November 2016 monthly total precipitation, Alaska 9-km WRF (right) compared to NOAA-NCEP GHCN dataset map (left).

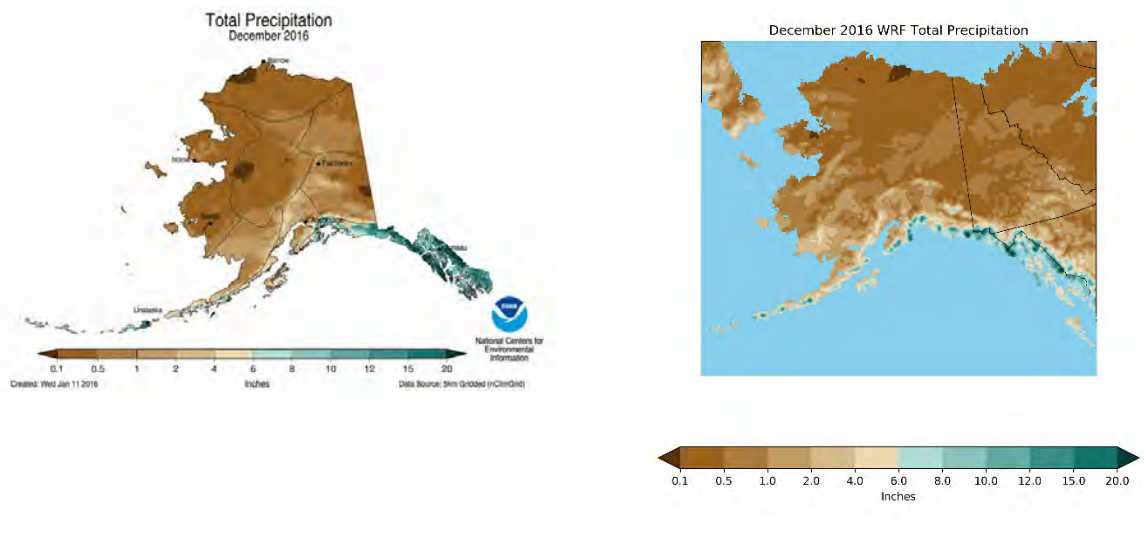

Figure 111. December 2016 monthly total precipitation, Alaska 9-km WRF (right) compared to NOAA-NCEP GHCN dataset map (left).

5. Conclusions

The EPA's 2016 Alaska WRF model 9 km dataset was evaluated in this report. WRF dataset hourly meteorological parameters were extracted at grid points nearest to the locations of surface and upper-air meteorological measurement stations, for comparison to measurements. Tools such as bias/error soccer-plots, parameter time series, and wind roses were used to assess the performance of surface meteorological parameters such as temperature, wind speed, wind direction, and humidity. Also, state-wide monthly precipitation maps were developed, using the WRF dataset, for qualitative comparison to observation-based precipitation maps.

The results demonstrate WRF error and bias vary by location, and the error and bias of the WRF model will need to be critically evaluated on a project-specific basis. This work was not intended as an investigative study, so no efforts were made to examine the causes of model error and bias in depth, although this could be a part of future project-specific evaluations.

Significant temperature biases along the north and northwest coasts of Alaska are likely due to the limits of the standard WRF model regarding the simulation of complex surface energy balances in the vicinity of sea-ice and tundra. These biases could potentially be corrected by use of parameterization schemes optimized for arctic conditions. The Polar WRF model, developed and maintained by the Byrd Polar Climate Research Center at Ohio State University (Byrd Polar and Climate Research Center, 2019), provides an alternative model parameterization that has been shown to improve WRF performance in Arctic regions (Brashers, et al., 2015). Application. Observational nudging may also serve to improve model predictions. Use of more layers in the vertical grid in some regions may also effectively improve performance, especially in the central and northern portions of Alaska impacted by strong winter inversions at the surface.

Future modeling efforts may focus on adoption of optimized schemes, methods, and physics modules to produce annual WRF datasets with less winter-time biases over the North Slope and interior of Alaska. The EPA may apply optimized schemes, such as those used in Polar WRF, as part of the optimization strategy.

The analysis products and plots contained in this report can be used by air permitting and other authorities in project-specific model performance evaluations to determine if the dataset is appropriate for regulatory use. Notably, this report itself does not represent an EPA endorsement or validation of the dataset. Any use of the dataset for regulatory purposes (such as those specified under 40 CFR Part 51, Appendix W) will require a project-specific performance evaluation. However, results from this report can be used as part of any project-specific MPE.

References

Appel, K., et al. 2011. *Overview of the atmospheric model evaluation tool (AMET) v.1.1 for evaluating meteorological and air quality models.* s.l. : Environmental Modelling & Software, Vol. 26, Iss. 4, pp. 434-443, 2011.

Bowden, J., Talgo, K. and Adelman, Z. 2015. *Western Air Quality Modeling Study WRF Meteorological Model Winter Modeling Application/Evaluation.* Chapel Hill, NC : UNC Institute for the Environment, 2015.

—. 2016. *Western-States Air Quality Modeling Study -- WRF 2014 Meteorological Model Evaluation.* Chapel Hill, NC : Prepared for Wester Regional Air Partnership by UNC Chapel Hill Institute for the Environment, 2016.

Brashers, B., et al. 2015. *Arctic Air Quality Modeling Study -- Meteorological Model Performance Evaluation: 2009-2013 BOEM Arctic WRF Dataset.* s.l. : Prepared by Ramboll Environ for U.S. Dept. Interior, BOEM. OCS Study BOEM 2015-049., 2015.

Brown, D. 2014. *WRF Meteorological Modeling in Support of Regional Air Quality Modeling for the 2011 Base Year.* s.l. : Iowa Dept. of Natural Resources, 2014.

Byrd Polar and Climate Research Center. 2019. Byrd Polar and Climate Research Center. [Online] Ohio State University, 2019. http://polarmet.osu.edu/PWRF/.

Emery, C., Tai, E. and Yarwood, G. 2001. *Enhanced Meteorological Modeling and Performance Evaluation for Two Texas Ozone Episodes.* Novato, CA : ENVIRON Int. Corp., 2001.

EPA, U.S. 2019. EPA CMAQ Atmospheric Model Evaluation Tool homepage. *U.S. EPA.* [Online] 2019. https://www.epa.gov/cmaq/atmospheric-model-evaluation-tool.

—. 2018. *Modeling Guidance for Demonstrating Air Quality Goals for Ozone, PM2.5, and Regional Haze.* Research Triangle Park, NC : U.S. EPA Office of Air Quality Planning and Standards, Air Quality Assessment Division, 2018.

Kemball-Cook, S., et al. 2005. *Alaska MM5 Modeling for the 2002 Annual Period to Support Visibility Modeling.* Novato, CA : ENVIRON Int. Corp., 2005.

NCAR. 2019. Weather Reseach and Forecasting Model. *National Center for Atmospheric Research.* [Online] August 2019. https://www.mmm.ucar.edu/weather-research-and-forecasting-model.

—. 2019. WRF ARW Model Users Page. *WRF Users Page.* [Online] 2019. http://www2.mmm.ucar.edu/wrf/users/.

NOAA-NCEP. 2019. Climate Monitoring National Temperature and Precipitation Maps. [Online] 2019. https://www.ncdc.noaa.gov/temp-and-precip/us-maps/.

Ramboll-Environ. 2015. *Allegheny County Health Dept. SO2 SIP WRF Model Performance Evaluation.* Novato, CA : Prepared for Allegheny County Health Dept., 2015.

Skamarock, W.C., Klemp, J.B., Dudhia, J., Gill, D.O., Barker, D.M., Duda, M.G., Huang, X., Wang, W., Powers, J.G. 2008. *A Description of the Advanced Research WRF Version 3.* 2008.

Tesche, T. and McNally, D. 2001. *Evaluation of CAMx and Models-3/CMAQ over the Lower Lake Michigan Region with Inputs from the RAMS3c and MM5 Models.* Ft. Wright, KY : Prepared for the Coordinating Research Council by Alpine Geophysics, LLC, 2001.

Vose, R.S., et al. 2014. *Improved historical temperature and precipitation time series for U.S. climate divisions.* s.l. : Journal of Applied Meteorology and Climatology, 2014.

Appendix A: Station Performance Plots
[Available in electronic format, upon request]
[Please contact: Jay McAlpine at MCALPINE.JAY@EPA.GOV]

United States Environmental Protection Agency	Office of Air Quality Planning and Standards Air Quality Assessment Division Research Triangle Park, NC	Publication No. EPA-454/R-20-003 May 2020